A tale of two cavities

J. Degallaix

Université Claude Bernard – Lyon I
Institut de Physique des 2 Infinis de Lyon
Laboratoire des Matériaux Avancés

Mémoire d'habilitation à diriger les recherches
soutenu publiquement le 30/11/2021, par :

Jérôme Degallaix

A tale of two cavities

Devant le jury composé de :

M.	Rémy Battesti	Rapporteur
M.	Christophe Dujardin	Président du jury
M.	Jérôme Morville	Invité
Mme	Edwige Tournefier	Rapportrice
M.	Jean-Yves Vinet	Rapporteur
Mme	Myriam Zerrad	Examinatrice

Sixty years ago I knew everything;
now I know nothing;
education is a progressive discovery of our own ignorance.

— Will Durant

ABSTRACT

This memoir is a summary of my research work at the Laboratoire des Matériaux Avancés (LMA) during the last 10 years. My activity focuses on the behavior of optical resonators and in particular on very low loss Fabry-Perot cavities used in frontier optical experiments.

In this document, I detail my contribution to two scientific experiments which rely on Fabry-Perot cavities: the French-Italian gravitational wave detector Virgo and the BMV (Biréfringence Magnétique du Vide) experiment at Laboratoire National des Champs Magnétiques Intenses at Toulouse. Two areas of research using cavities of vastly different dimensions but sharing also some common points: a small bandwidth as well as mirrors coated at LMA.

On Virgo, I worked on the second generation of the detector called Advanced Virgo (AdV). It is the instrument that will stay in our memory as the first one to have directly detected a Gravitational Wave (GW) in Europe in 2017. With its American counterpart LIGO, these two collaborations have launched the revolution of GW astronomy.

On AdV, I was the subsystem manager of the Optical System and Design (OSD) during the design and building of the instrument. The base configuration of AdV is a Michelson interferometer with 3 km long Fabry-Perot arm cavities. I explain how we derive the main specifications for the polishing and coating for the arm cavities mirrors based on optical simulations. The history of the mirrors is briefly described from the procurement of the blocks of glass up to the installation on the site. These exceptional mirrors of diameter 350 mm and weighting 40 kg are the best which could be achieved in matter of substrate, polishing and coating during the years 2010s.

Once the interferometer was pruning, I was the coordinator of the optical characterisation of the detector. I mention the various methods used to measure in situ the properties of the large mirrors and compare the results to our expectations. The most critical parameter is the arm cavity round trip loss, we managed to meet the specifications.

In the second part of this publication, I focus on a different kind of Fabry-Perot cavity compared to the AdV arms: a much shorter one but with also much higher finesse, that is the BMV cavity. In the middle of the cavity one can find an intense magnetic field and the aim is to measure directly the magnetic birefringence of vacuum as predicted by the theory of quantum electrodynamics. I was the motor behind the implementation of such cavity at LMA (but without the magnetic field) and we managed to measure a finesse of 370 000.

In the last 2 years, this cavity has benefited from a large upgrade with the installation of the mirrors on hexapods. Hence, it is now

possible to measure the optical loss as a function of the position of the laser beam on the mirrors. We can now also study the effects of the degeneracy of the cavity by tuning the distance between the two mirrors, the round trip optical losses are expected to increase when one higher order optical mode resonates at the same time as the fundamental one. During the writing of this HDR, we are currently commissioning and doing the automation of this setup.

Finally, in the annex of this document, I have added 5 articles that I published in peer-reviewed journals that highlight my scientific contribution. I am the first author for 4 articles and for the fifth one it is a PhD student that I was supervising.

The two first articles deal with the next generation cryogenic substrates for the European Einstein Telescope, the successor of Virgo in operation around the year 2035. For low temperatures, fused silica can no longer be used as mirror substrates due to excessive thermal noise, crystalline materials such as silicon or sapphire are so far the preferred candidates for the next mirrors. We have measured for the first time the optical absorption of ultra-pure silicon substrates at 1550 nm.

Two articles demonstrate the role of optical simulations in designing optical cavities and how it is essential to define the mirror surface specifications. In one article, the simulation code OSCAR that I have developed is detailed. The fifth article is a review of the detailed performances of the mirrors of AdV including all the characterisation done on the substrates and surfaces before and after coating. This paper aims to be the reference paper about the mirrors of AdV.

RÉSUMÉ DES TRAVAUX

Ce mémoire est un résumé de mes travaux de recherche au sein du Laboratoire des Matériaux Avancés (LMA) au cours de ces dix dernières années. Mon activité se concentre sur la physique des résonateurs optiques, en particulier sur les cavités Fabry-Perot faibles pertes utilisées en tant qu'amplificateurs dans les expériences d'optique de pointe.

Dans ce document, j'ai choisi de me focaliser sur ma contribution à deux expériences de physique ayant toutes les deux des cavités Fabry-Perot en leur cœur : le détecteur Franco-Italien d'ondes gravitationnelles Virgo en Italie et l'expérience BMV (Biréfringence Magnétique du Vide) au Laboratoire National des Champs Magnétiques Intenses à Toulouse. Deux recherches avec des cavités que tout semble opposer en terme de dimensions et pourtant qui partagent une très faible bande passante et des miroirs traités au LMA.

Sur Virgo, j'ai travaillé sur la deuxième génération du détecteur appelé Advanced Virgo (AdV). C'est l'instrument qui restera dans nos mémoires comme celui ayant réalisé les premières détections directes d'ondes gravitationnelles sur le sol européen en 2017. Avec les détections de son alter ego américain LIGO, ces événements ont marqué le début de la révolution de l'astronomie gravitationnelle.

Sur ce formidable instrument, j'ai été responsable du design optique lors de sa conception. AdV a pour configuration de base un interféromètre de Michelson avec des bras qui sont en fait des cavités Fabry-Perot longues de 3 kilomètres. Je relate donc le cheminement intellectuel et les simulations optiques qui ont été faites afin de trouver les bonnes spécifications pour le polissage et le traitement de surface (coating) des miroirs des cavités Fabry-Perot. J'explique aussi rapidement l'historique des miroirs de l'achat des blocs de silice (verre) jusqu'à l'installation sur le site de l'expérience. Ces miroirs de 350 mm de diamètre pour un poids de 40 kg représentaient les meilleures performances que nous pouvions espérer en matière de verre, polissage et traitement optique dans les années 2010.

Une fois l'interféromètre assemblé, je fus coordinateur de la caractérisation optique du détecteur. Je détaille donc les différents types de mesures qui ont été faites pour caractériser les performances optiques des cavités des bras et je les compare à nos attentes. Les miroirs des bras sont les éléments les plus sensibles sur le plan des pertes optiques et nous verrons que malgré les spécifications très strictes, nous avons réussi à les atteindre.

Dans une deuxième partie de cet ouvrage, je parle d'un deuxième type de cavité Fabry-Perot, bien plus compactes puisque longue de

seulement quelques mètres, mais aussi avec des finesse bien plus élevées (1000 fois plus) comme celle de BMV. Cette cavité, placée à l'intérieur d'un champ magnétique, a pour but de mesurer la biréfringence magnétique du vide, effet prédit par la théorie d'électrodynamique quantique contemporaine. J'ai été le maître d'œuvre de l'installation et de la caractérisation d'une telle cavité similaire au LMA[1], où nous avons mesuré une finesse de 370 000.

Au cours des années 2020 et 2021, cette cavité a subi une importante, mise à jour, avec en particulier le montage des miroirs sur des hexapodes permettant des mesures des pertes optiques en fonction de la position du point d'impact du laser sur les miroirs. Nous avons aussi maintenant la possibilité de changer la longueur de la cavité et d'étudier les effets de dégénérescence lorsqu'un mode optique d'ordre supérieur résonne en même temps que le mode fondamental. J'explique les motivations pour les modifications et détaille les nouvelles possibilités. Lors de l'écriture de cette HDR, nous sommes en phase de mise en service et d'automation de cette nouvelle expérience.

Finalement, en annexe de ce document j'ai ajouté 5 articles publiés dans des revues à comité de lecture, qui décrivent mes résultats scientifiques ou mes thématiques de recherche. Je suis premier auteur pour 4 de ces articles, deuxième auteur pour le cinquième qui a été écrit par un doctorant que je supervisais.

Deux articles concernent la recherche sur les substrats de demain pour la prochaine génération de détecteurs d'ondes gravitationnelles. Dans ces nouveaux détecteurs les miroirs des bras seront refroidis à température cryogénique, nécessitant des substrats cristallins comme le silicium ou saphir à la place de la silice. Nous avons réalisé les premières études sur l'absorption optique du silicium ultra-pur à 1550 nm.

Deux des cinq articles concernent les simulations optiques. Le premier détaille une technique pour faire des simulations de pertes dans les cavités optiques en utilisant la cartographie de surface des miroirs. Le second explique le principe du code de simulation optique OSCAR que j'ai développé et qui est maintenant utilisé par différents groupes de recherche.

Enfin le cinquième article est une revue d'ensemble sur les performances des miroirs des cavités d'Advanced Virgo. En particulier, les résultats des caractérisations optiques sur les miroirs avant et après dépôt sont explicités et peuvent servir de référence.

1 mais sans champ magnétique.

CONTENTS

1 INTRODUCTION

It was the best of times, it was the worst of times[1] could be one way to summarise 10 years of working in close contact with the mirrors of the Virgo gravitational wave detector. In this report, I will not talk about all the mirrors inside this laser interferometer but only the most critical ones: the ones forming the Fabry-Perot arm cavities. It is between these mirrors that the gravitational wave signal becomes imprinted in light's phase and then recorded.

In the second part of this manuscript, I will talk about another Fabry-Perot cavity, much shorter but with much higher finesse. This cavity is in a cleanroom at LMA and is a copy of the original one at the LNCMI (laboratory expert in very intense magnetic fields in Toulouse) aiming to directly measure the magnetic birefringence of vacuum. Another extreme optical experiment to push further the knowledge of the Universe and its Laws.

Even if vastly different, these two cavities share a similar linewidth and mirrors with high reflective coatings made in LMA.

1.1 THE DETECTION OF GRAVITATIONAL WAVES

A direct consequence of Einstein's theory of General Relativity (1915) [1], gravitational waves appeared as a purely theoretical prediction [2] in a follow-up paper one year later. According to this theory, the flow of time can be altered by the presence of mass or energy and space-itself becomes an elastic media. Gravitational Waves (GW) are ripples of the space-time created by accelerating masses and they can travel at the speed of light through the universe [3]. Contrary to electromagnetic radiation, gravitational waves are not absorbed by matter bringing unique information about their sources unavailable by other means. The fact that they can not be stopped already gives us a hint about the difficulties to detect them.

To be detected directly on Earth, the GW amplitude must be large enough and so far only the loudest (and closest) events in the Universe could be recorded. Two ingredients are necessary to detect such signals on Earth: heavy masses must be involved in the order of one to a hundred of solar masses and the bodies must be moving with extreme speed in percents of the speed of the light. Such cataclysmic

1 To plagiarize shamelessly the beginning of A Tale of Two Cities by Charles Dickens. For completeness, the good times were more frequent than the bad ones and of larger absolute magnitude.

events can not happen on Earth, nor in our solar system but occur in a regular fashion outside our galaxy.

The main sources of GW can be classified into two categories:

SHORT TRANSIENT That is the favorite target of our current detectors with the coalescence of compact binary objects. By compact, we mean with extreme densities such as the ones found in black holes or neutron stars. Such two body systems are tied by gravitational attraction, rotating around their centers of mass for millions of years but still getting imperceptibly closer and closer as GW are emitted [4]. The detectable signal for ground based laser interferometers could last from 0.1 second for heavy stellar mass black holes fusions to several tens of seconds for the signal from the inspiral phase of lighter binary neutron stars.

A burst of GW is also expected from massive stars at the end of their lives during the core collapse. Such signals from type II supernova are expected to last less than one second [5].

Short GW Signals with large unconstraint models are also expected from pulsar glitches [6] or from cosmic strings [7].

CONTINUOUS SOURCES are sources that can last in time scales longer than weeks or months. One expected continuous source generating a monochromatic signal (at a single GW frequency) is a spinning neutron star with a non perfectly spherical shape (i.e. with a mountain on the surface) [8]. A primordial GW stochastic background is also expected from the big bang [9], but that is only a prime target for next generation GW detectors.

1.2 THE BIRTH OF A NEW ASTRONOMY

I was lucky to witness (and directly participate in) the announcements of the first GW directly detected on Earth. Those are defining moments in the history of science, setting a before and an after. If I should select my three landmark moments they would be in chronological order:

1. The first detection GW150914 [10] in September 2015 and publicly announced 6 months later during worldwide press conferences. That is a golden event, well above the detector background noise and it was even recorded before the official start of the first observational period O1 of the Advanced LIGO interferometers. This signal is from the coalescence of 2 black holes of 36 and 29 $M_\odot$[2] at a distance of 460 Mpc.

2. The first multi-messenger observation with GW of the coalescence of two neutron stars with the event GW170817 [11] dur-

2 $M_\odot$ is the unit of one solar mass with our sun as reference.

ing the second observational run O2 in 2017. A short gamma-ray burst was detected 2 seconds after the GW signal had been recorded by both LIGO interferometers as well as Virgo. Then 11 hours after, the visible electromagnetic counterpart was localised with the host galaxy. More than 70 observatories covering the spectrum from radio waves to X-rays were able to study the event GW170817. This coalescence is the most complete observation of a kilonova and provides unprecedented insights to compare the speed of gravity versus the speed of light [12] or study nucleosynthesis [13]. It also demonstrates cosmological measurement of the Hubble constant with GW [14].

3. The publication of the O3A catalogue [15] as well as the public release of the LIGO-Virgo detectors output (called strain data) for the same period [16]. O3 is the third science run (2019-2020) and the catalogue O3A summarise all the GW sources detected in the first 6 months of this data taking run. In one paper, the total number of GW events detected was multiplied by 3, reaching a total of 50 coalescences detected (mostly black-black hole fusions).

The last 5 years were exceptional from the scientific point of view, starting from few events per year detected at the start of Advanced LIGO/Virgo to routinely detect one every week thanks to the improvement in the detector sensitivity. Starting with exceptional events, we are now doing statistics on the population of stellar mass black holes. 5 years which made GW astronomy a reality.

At the time of writing (year 2021), a network of GW detectors is currently running with the two American LIGO interferometers [17], the European Virgo [18] and the Japanese KAGRA [19]. The future commissioning and data taking times could be found in the living document about the observational prospects for the next 5 years [20].

At several places in this document, for the time frame we will refer to the data taking periods of the LIGO-Virgo collaboration. Those science runs are called sequentially O1, O2,... with O standing for Observation and are summarised in the table 1.

1.3 LASER INTERFEROMETRY

GW detectors are giant Michelson laser interferometers. While the efforts to detect those elusive waves started in the '60s with Joseph Weber's resonant bars [22], the progress in lasers and optics in the last four decades made laser interferometers the ubiquitous choice for GW detectors. They can achieve better sensitivity and larger bandwidth, albeit at the expense of increased complexity and with a much larger footprint.

Table 1: 39 in O3a

RUN	DATES [a]	COMMENT
O1	09/15 - 01/16	First GW detected with a fusion of two black holes, only with the two LIGO detectors [10].
O2	11/16 - 08/17	Virgo joined the last month. First fusion of neutron stars detected with GW [11]
O3	04/19 - 03/20	Almost one year of data with the 3 detectors. 1 event every 6 days on average. First fusions of neutron star and black hole recorded [21]
O4[b]	12/22 - 12/23	Sensitivity increased by a factor 2
O5[b]	??/25 - ??/26	Sensitivity again doubled. Several events per day expected

[a] Starting and end dates of the science runs as month/year.
[b] Dates to be confirmed.

1.3.1 *Principle of detection*

A GW of amplitude $h(t)$ arriving perpendicular to the plane of the Michelson interferometer will induce an equivalent differential change of the arm length $\Delta L(t)$ given by:

$$\Delta L(t) = h(t)L \tag{1}$$

with L the length of the arm of the Michelson interferometer as seen in figure 1. That is the simplest formula to understand the idea that detecting a GW is detecting a differential length change in two perpendicular directions. Closer to the physical equations, a passing GW is a distributed effect along the arm length equivalent to a (very small) modulation of the refractive index of the vacuum. So in practice the GW is imprinted as a modulation of the phase of the reflected light from the Michelson's arms. The phase variation is then converted to a variation of the optical power at the detection port of the interferometer through the interference phenomena at the beamsplitter.

All the challenge of the detection comes from the extremely small value of the GW amplitude h on Earth. An example is given below for the fusion of two black holes, similar to the first detection of the event GW150914.

$$h = 1.5 \times 10^{-21} \left(\frac{\text{Mass}}{30\ M_\odot}\right) \left(\frac{400\ \text{Mpc}}{\text{Distance}}\right) \left(\frac{\text{Frequency GW}}{50\ \text{Hz}}\right)^{\frac{2}{3}} \tag{2}$$

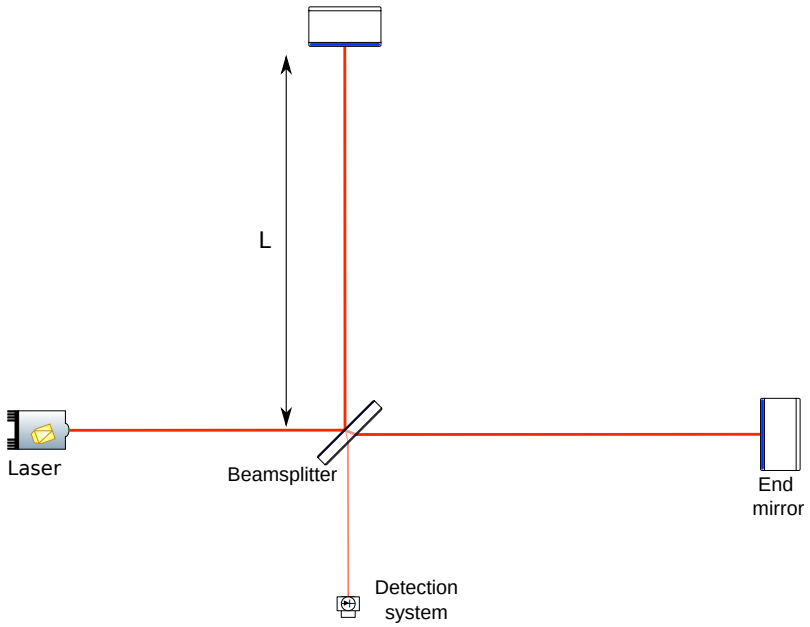

Figure 1: Schematic of a Michelson interferometer with two perpendicular arms of length L.

the frequency of the GW being twice the orbital frequency of the two massive objects. So with a Michelson arm length of 3 km, the GW signal will induce a differential arm length change of 5.10^{-18} m, much smaller than the size of the nucleus of an atom (10^{-15} m). Recording such extremely small distance changes over several kilometers highlight the difficulty of detecting audio-frequency GW on Earth.

1.3.2 *Finding the needle signal from the haystack of noise*

Measuring a GW is equivalent to measuring a small differential arm length change of the Michelson interferometer as seen in the previous section. During half a period of the GW, one arm becomes shorter while the other one becomes longer and during the second half period the opposite is happening. During normal operation, the Michelson interferometer is tuned to be on what is called the dark fringe. The light coming back from the 2 arms interferes destructively toward the detection side, all the light being reflected back toward the laser. A passing GW by modulating differential arm length will generate light at the dark port whose power is then recorded by a photodiode.

Measuring ridiculously small differential displacement of the order of 10^{-19} m is extremely difficult and numerous noises could dominate at the output of the interferometer the astrophysical GW signals. In this section, we will briefly remind the main strategies to maximise

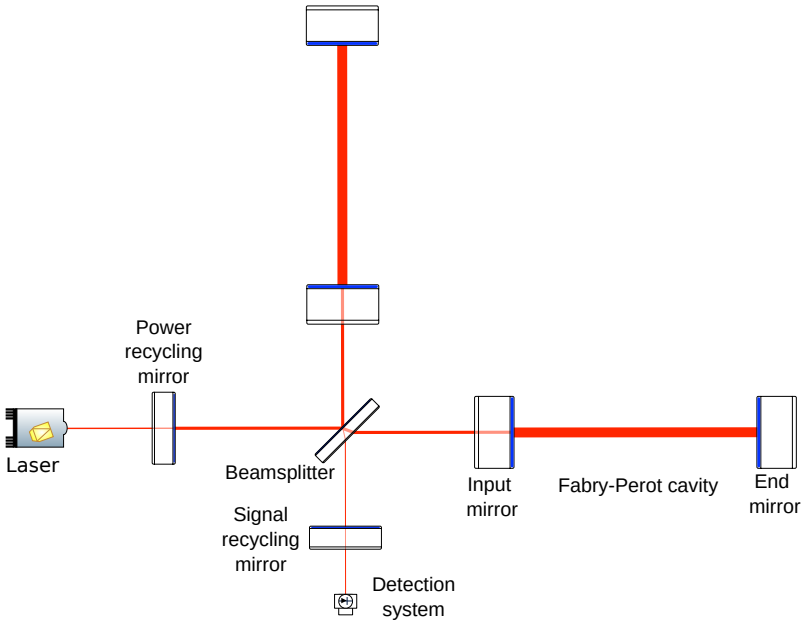

Figure 2: A more realistic schematic of a laser GW detector. Such topology is called dual recycling Michelson interferometer with Fabry-Perot arm cavities, that is the current configuration of Advanced Virgo and Advanced LIGO.

the recorded signal and also the main noises limiting the interferometer sensitivity.

1.3.2.1 *Increasing the GW signal*

The first action to increase the signal would be to have long arms for the Michelson interferometer as shown by the formula 1. To be noted: the extra light phase shift induced by the GW is cumulated as the light propagates along the arm length, as a consequence longer arms also mean shorter bandwidth for the detector[3].

To stay with Michelson arms length in the order of the kilometers to save space and cost (3 km for Virgo and KAGRA, 4 km for LIGO), a second lever is to increase the interaction time between the GW signal and the circulating light in the detector. For that, the two perpendicular arms of the Michelson are replaced by Fabry-Perot cavities. As an example, for Advanced Virgo the arm cavity finesse $\mathcal{F}$ is 450, given a phase amplification factor of $2\mathcal{F}/\pi$ ($\sim$ 290), to be noted this value is also the light power gain of the cavity (demonstrated in section 2.7.2).

The third action to increase the signal at the output of the detector, is to further increase the circulating power in the arm cavities. For that, the laser power at the input of the instrument is maximised and all the light exiting toward the laser is re-injected by the addi-

3 Bandwidth which could be partially compensated by the microscopic tuning of the position of the signal recycling mirror as defined later.

tion of a power recycling mirror [23] (seen between the laser and the beamsplitter in figure 2). To give an idea of the amount of light we are talking about for the design of Advanced Virgo, the input laser power is 200 W at 1064 nm with 120 W entering the interferometer. The circulating power in the recycling cavity is 5 kW and the power in the arm cavities can reach up to 650 kW. Even if 120 W enters the detector, only a small fraction is transmitted or reflected. The vast majority of the light is simply lost as scattered light in the detector.

1.3.2.2 *Decreasing the noise*

Numerous noises could induce an equivalent mirror displacement at the level of 10^{-19} m. Two noises are of particular interest because they limit the detector sensitivity in mid and high frequency ranges: the first is the Brownian coating thermal noise and the second one is the light quantum noise. As current limiting factors, these noises are driving the technical choices of the upgrades of Advanced Virgo.

The Brownian coating thermal noise is induced by the random thermal fluctuations of the two dielectric materials of the amorphous thin coating of the arm cavity mirrors. For Advanced Virgo (and LIGO), the thin coating is a Bragg reflector made of alternate layers of two materials: fused silica for the low refractive index material and tantala doped titania for the high one [24]. To understand the levers for reducing this noise, we can detail further its main parameters: the power spectral density of mirror displacement due to the coating thermal noise S_{CTN} is proportional to:

$$S_{CTN}(\omega) \propto \frac{T}{\omega} \frac{d\phi}{w^2} \tag{3}$$

with T the temperature of the mirror, d the thickness of the coating, ϕ the mechanical loss angle of the coating and the w the radius of the laser beam incident on the mirror. To reduce this noise for the next upgrade of Virgo (Advanced Virgo +), new coating materials are actively searched to hopefully reduce at the same time d (by increasing the refractive index contrast between the two coating materials) and ϕ, while keeping the outstanding optical properties of current materials. The geometry of the arm cavity will also be updated to allow larger laser beams on the end mirrors and hence increase w. The KAGRA detector is exploring another path by using sapphire cryogenic mirrors cooled down at 20 K to limit the impact of the coating thermal noise.

The second most relevant noise is from the quantum nature of light itself. This noise in the interferometer limits the sensitivity by two mechanisms: at low frequency as radiation pressure noise and in mid and high frequency as shot noise.

The radiation pressure noise is the effect of the back action of light while measuring the position of the suspended mirrors. The power

spectral density of the radiation pressure noise S_{RP} (again as equivalent displacement) is proportional to:

$$S_{RP}(\omega) \propto \frac{1}{m\omega^2}\frac{P}{\lambda} \tag{4}$$

with m the mass of the mirror, ω the frequency, P the power on the mirror and λ the wavelength. Due to the frequency dependence in $1/\omega$ in amplitude, the radiation pressure noise is only dominant at low frequency.

To measure the passing GW, the optical power at the output of the detector is recorded. This measurement could be seen as counting the number of photons per unit of time. Due to the discrete nature of light, the arrival time of the photos follows a Poisson statistic. For a simple Michelson without arm cavities, the power spectral density of the shot noise limited sensitivity is proportional to:

$$S_{SN} \propto \frac{\lambda}{P} \tag{5}$$

It is important to note that the radiation pressure noise and the shot noise have an opposite tendency regarding the laser power. Up to recent years, GW detectors sensitivity was limited by the shot noise at high frequencies whereas the radiation pressure noise was below technical noises at low frequencies. So the path forward to improve the sensitivity was to increase the laser power with the side effect of the need for complex thermal compensation systems to reduce the wavefront distortion due to the residual optical absorption [25].

A second strategy to reduce the shot noise is the injection of squeezed vacuum state at the output of the detector. First, frequency independent squeezing [26], reducing the shot noise level by 3 dB during O3 but with the penalty of increasing the opposite quadrature (Heisenberg principle) leading to excess radiation pressure noise. So to decrease both quantum noises at the same time requires the injection of frequency dependent squeezed vacuum light [27]. Such implementation is expected for the run O4 with the addition of a 300 m long filtering cavity at Virgo [28].

1.3.2.3 *The theoretical noise budget*

Except for the two main limiting noises described previously, numerous other noises can also degrade the sensitivity of GW detectors. An example of the theoretical noise budget of Advanced Virgo can be found in the figure 3. Only our best known enemies are in this figure, but during the operation of the interferometer, additional noises may also limit our detection capability such as control noise at low frequency [29] or scattered light in the most sensitive part [30].

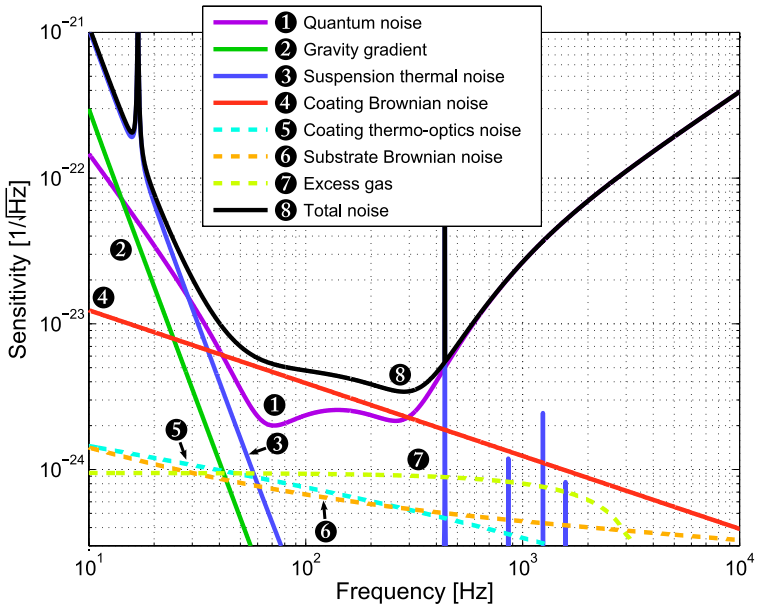

Figure 3: Noise budget of the Advanced Virgo GW detector. The vertical axis is the amplitude spectral density of the noise in unit equivalent to the GW amplitude h. To put it simply, a passing GW with an amplitude about the sum of all the noises (curve labeled 8) will be detected, if it falls under it will be buried in the noise.

The shot noise limit at high frequency is not flat as presented before in a simplified way but due to the presence of the long arm cavities which act as a low pass filter for the GW signal, it rises at high frequency.

Operating a GW detector is not only about having the best sensitivity but also a high duty cycle with clean data. So in parallel to noise hunting, considerable efforts also go to increase the robustness and stability of the interferometer. For example, controlling thermal aberration, mitigating scattered light or hunting for non-stationarity process creating glitches in the data [31] are also essential to operate the instrument. So the noise budget only tells one part of the story when looking to improve the machine and design subsequent upgrades.

1.4 AT THE HEART OF VIRGO: THE KILOMETER-LONG ARM CAVITIES

The GW signal is imprinted on the phase of the light in the 3 km long arm cavities of Virgo. It is really between the four large mirrors of the two cavities that the magic happens: the GW signal is transduced to a more easily measurable physical variable, a differential modulation of the phase of the light reflected by the two arms. Apart from the length of the cavity which is the separation distance between the two mirrors, the performances of the cavity are only set by the mirrors

Table 2: Impact of the mirror parameters on the sensitivity, only the most obvious linked are mentioned here.

PARAMETER	VARIABLE	IMPACT
	Substrate	
Size	Diameter	drives the beam size and so the thermal noise level
Dimensions	Mass	heavier mass reduces the radiation pressure noise
Material	Density	gives the mass
Material	Absorption	must be very low for the arm input mirror
	Polishing	
Geometry	RoC[a]	sets the laser beam size on the mirrors
Surface	Flatness	influences the contrast defect
Surface	Roughness	directly linked to the scattering loss
	Coating	
Material[b]	Loss angle	sets the coating thermal noise level
Material[b]	Optical loss	optical absorption and scattering
Process	Uniformity	optical mode shape

[a] Radius of Curvature.
[b] Not only the material is relevant here but also the coating deposition parameters as well as the post deposition thermal treatment (called annealing).

themselves. So to achieve a near perfect cavity would require near perfect mirrors. Moreover, the characteristics of the mirrors constrain directly the sensitivity. As an illustration, a non exhaustive summary of the dependency between sensitivity and mirror parameters can be found in table 2.

As detailed in the next chapter, the optical losses in the arm cavity are critical and must be kept as low as possible to reach the desired circulating power in the interferometer. To achieve that goal, the large mirrors of the cavity must have outstanding optical properties but also must be kept pristine despite all the contributors involved from casting the glass ingot to the final installation on site.

To give an idea of the shape of the large optics, a photo of two arm cavity mirrors in the cleanroom at LMA is shown in figure 4. They are made of the most transparent glass, free of any defect, polished

Figure 4: Photo of two arm cavity mirrors. They are cylindrical mirrors with a diameter of 350 mm for a thickness of 200 mm. Each one weights around 40 kg. Photo: L. Pinard

at $\lambda/300$[4] and with a reflectivity of 99.999% at 1064 nm for the end mirrors. A review paper about those mirrors can be found in page 125.

1.5 THE BMV FABRY-PEROT CAVITY

The second topic of this HDR is another optical cavity, shorter but with much higher finesse. The goal is also different since the cavity is not looking for astrophysical signals but aims for the first measurement of the Vacuum Magnetic Birefringence (VMB in English or BMV in French). The VMB is a non linear electromagnetic effect predicted by Quantum ElectroDynamics (QED) [32]: under a strong magnetic field, the vacuum itself becomes birefringent and changes the polarisation of the light.

The VMB experiment consists of a few meters long Fabry-Perot within a pair of polarisers to discriminate the light polarisation. The resonating light passes through a giant magnet sitting in the middle of the cavity. In Europe, two main experiments are using this approach: PVLAS using rotating permanent magnets [33] at Legnaro National Laboratories in Italy and BMV in France with pulsed magnets [34] at Laboratoire National des Champs Magnétiques Intenses in Toulouse. PVLAS has officially ended its search at the end of 2017 but this activity may continue at CERN in the coming years. The

4 Typical jargon from 'optics people', as a comparison, a good quality mirror is typically only at $\lambda/20$.

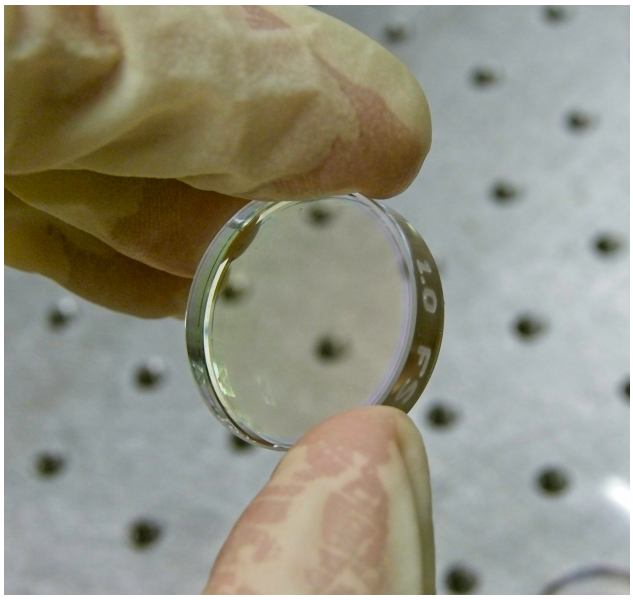

Figure 5: Photo of one of the two BMV mirrors. The mirrors have the standard dimensions of 25 mm in diameter for a 6 mm thickness.

second one, the BMV experiment is still going on with a steady collaboration with LMA.

The installation of a BMV like cavity at LMA started in 2015 following a successful ANR grant. The LMA was responsible for the coating of the very high finesse mirror as well as all the optical characterisation. For this goal, a cavity able to measure the round trip loss of the mirrors has been setup. The first measurement of the cavity finesse was achieved in 2018 and in 2020 a major upgrade program has started to measure the loss as a function of the position of the incident beam on the mirrors.

The mirrors are much smaller than the ones for Virgo and much easier to manipulate as shown in figure 5. Working on a tabletop experiment with only a few people involved, mastering all the components on the optical table or in the electronic rack is rather relaxing compared to the work at Virgo.

1.6 THE TWO CAVITIES IN A NUTSHELL

A summary of the main parameters of the two cavities is shown in the table 3 for easy comparison. The work on each cavity will be detailed in the subsequent two chapters.

Even with vastly different characteristics, the two cavities still share the same order of magnitude of linedwidth and mirrors coated at LMA. Another common point, albeit anecdotally, would be that I work closely on both.

Table 3: Summary of the two optical cavities that are discussed in this manuscript.

		ADVANCED VIRGO	BMV@LMA
Location		Cascina (It)	Villeurbanne (Fr)
Laser wavelength	[nm]	1064	
Length	[m]	3000	1.7
Vacuum	[mbar]	10^{-9}	0.1
Mirror diameter	[mm]	350	25.4
Mirror weight	[kg]	42	0.007
Finesse		450	400 000
Linewidth	[Hz]	100	240

NOTE ON THE BIBLIOGRAPHY

I should apologise in advance as some of the bibliographic references are internal Virgo notes stored in the Technical Document System (TDS [35]) and those are only accessible to Virgo collaboration members. I try to limit at the maximum such references and of course I can provide them on demand. Online posts from the Virgo logbook [36] are accessible to all readers.

2

THE VIRGO ARM CAVITIES

This chapter focuses on the work done on the design and characterisation of three different Virgo arm cavities. I joined LMA at the end of summer 2010 and my first work was on the Virgo+ arm cavities. Virgo+ [37] was the last incarnation of the initial Virgo and was decommissioned in fall 2011 to leave room for Advanced Virgo.

Most of my 10 years at LMA were dedicated to Advanced Virgo. I became SubSystem Manager (SSM) of the Optical Simulation and Design (OSD) for the Advanced Virgo project at the end of 2011 and kept this role up to the official end of the project at the start of 2017 (before the first virgo data taking O2 during the summer of the same year). The OSD subsystem was in charge of the optical design of Advanced Virgo, the development and management of simulation tools and also to assist the commissioning and operation of the interferometer. During the peak activity of the design, six full-time persons were working for OSD. I was myself also contributing to the simulation effort, not only managing it.

From 2016 up to now, I am also the coordinator of the optical characterisation of Advanced Virgo. The goal is to measure in-situ the optical parameters of the detector to tune the simulations and help the commissioning.

In 2018 and 2019, I did the first design of the arm cavities of Advanced Virgo+, the next upgrade of Advanced Virgo before passing my role of OSD SSM to Sebastian Steinlechner from Maastricht University. I am still present and a pillar of OSD, contributing to optical simulations.

2.1 INTERFEROMETER NOMENCLATURE

Different acronyms and abbreviations will be used in this chapter to refer to Virgo optics and so must be detailed first. For simplicity, the short names are usually the initials of the object, for the large optics we omit the word "mirror" and just refer to their location: WI stands for West Input (mirror). A detailed layout is shown in figure 6 with the suspended benches (the letter S stands for Suspended) and also the main photodiodes starting with a letter B.

The overall layout is similar between Virgo+ (up to 2011) and its successor Advanced Virgo (from 2015) with the exception of new large optics in the recycling cavities: the Pick Off Plate (POP) in front of the Power Recycling mirror (PR) and the Compensation Plates (CP)

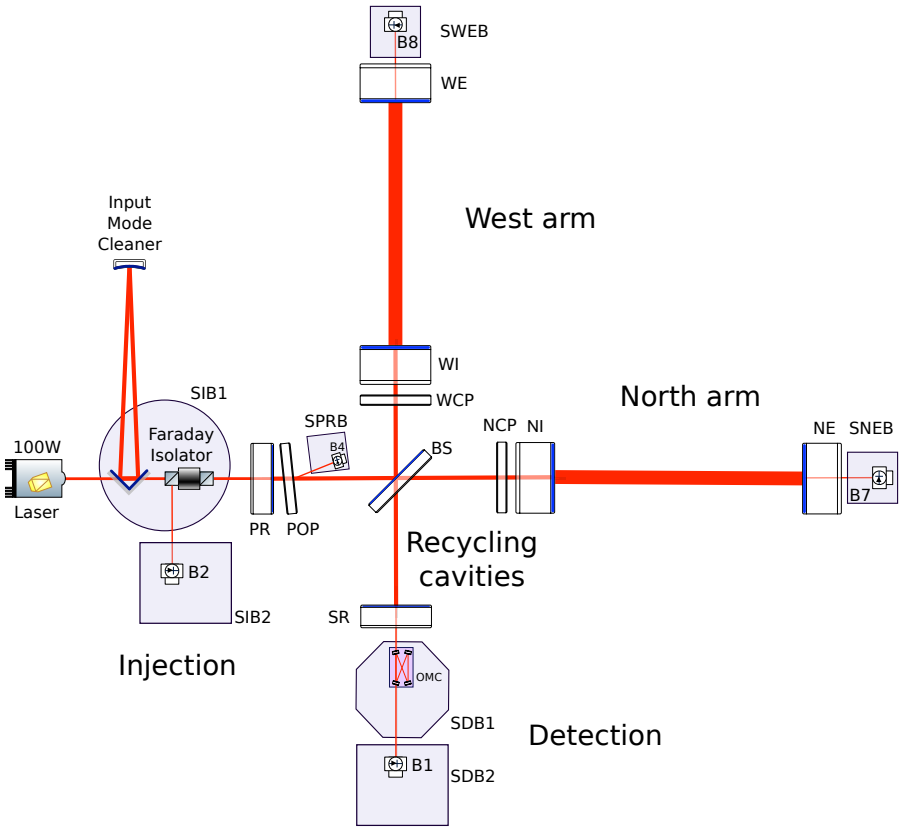

Figure 6: Advanced Virgo simplified optical scheme. Only the main mirrors are represented in this scheme.

in front of the input mirrors and since 2020 the Signal Recycling mirror (SR).

2.2 CHARACTERISATION OF THE VIRGO+ ARM CAVITIES

In 2010, the French Italian detector was in its Virgo+ version including for the first time the monolithic suspension[1] [38]. My first work was to try to measure in-situ the Radius of Curvature (RoC) of the arm cavity mirrors.

At that time, the arm cavity configuration was a flat input mirror with a curved concave end mirror. Unfortunately, while within the specifications, the RoCs of the end mirrors were on the opposite side of the tolerances, with a large asymmetry of more than 100 m over an average RoC of 3400 m. More specifically the NE RoC is 3300 m to be compared with the WE RoC of 3410 m. This large difference resulted in a poor dark fringe contrast with a large optical mode Laguerre Gauss (LG) of order 10 (the doughnut shape) at the dark port, increasing the coupling of the laser noise to the GW channel.

1 In that configuration, the mirror, the attachment ear and the suspension fibers are all made of the same material: fused silica

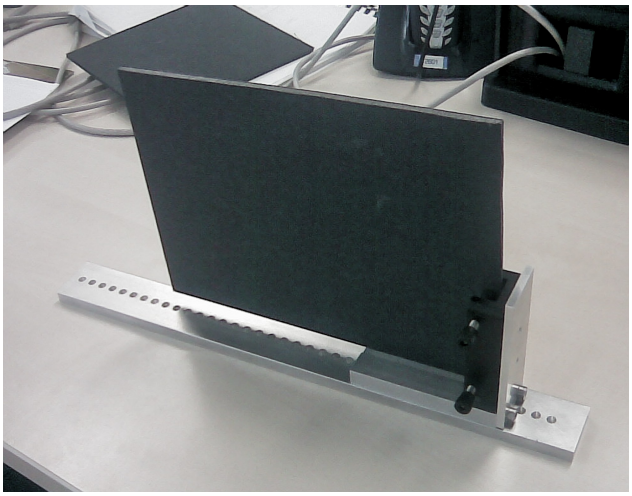

Figure 7: Moving black card board screen to cut the beam in transmission of the arm cavities. The holes on the bottom plate ensures accurate displacement.

The solution to solve this RoC asymmetry was the implementation of a thermal actuator to heat the central part of the mirror and hence by thermal expansion increase its RoC. Practically, a resistive heating element was designed to project heat at the center of the mirror [39]. This heater was positioned in front of the NEM mirror but below it and directly inside the vacuum tower. This strategy was implemented at the end of 2010 and the required heating power was fine tuned in the subsequent months reducing the power of the LG 10 mode by a factor 20 at the dark port [40].

Since one mirror RoC's inside the interferometer was changed, it became relevant to be able to measure in-situ its new profile. It is usually not possible to individually measure the RoC of both mirrors once the cavity is installed, so we assumed the input mirror to be perfectly flat[2]. With that hypothesis, we can derive the RoC of the end mirror by measuring the size of the laser beam in transmission of the cavity.

To measure the beam size, I got the idea to use the knife-edge technique [41] in transmission. With this technique, we record the intensity of a laser beam as it is progressively blocked by a screen. The transmitted power as a function of the screen position is directly linked to the beam radius of the laser. This solution is relatively easy to implement as the beam size in transmission of the arm cavities is large with a radius of 4 cm. The difficulty is more about finding a place to insert the screen. It was not possible to position it right after the end mirror which is in vacuum but we have to position it just after the first lens of the telescope in air and located on an optical table.

2 The Virgo+ arm cavities were plano-concave.

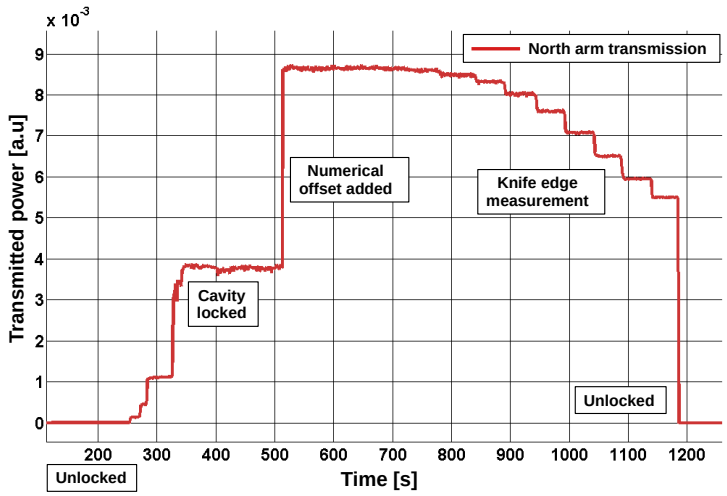

Figure 8: Time series of the power transmitted by the arm cavity as the screen is blocking progressively the beam from 700 s. At some point, when the screen is blocking too much of the beam the cavity unlocked.

The mechanical setup to cut the beam is shown in figure 7. The screen is only a black cardboard that can be moved by steps of 1 cm thanks to a grid of positioning holes at the base. Due to the very low transmission of the end mirror (3 ppm), only a small amount of power is transmitted by the arm cavity (< 50 mW over a 100 mm beam diameter) and so blocking the beam did not represent a significant hazard.

The transmitted power as a function of the time during one knife-edge measurement is shown in figure 8. It should be noted that the transmitted beam is not usually dumped but rather send to photodiodes to diagnose the state of the interferometer and also participate in the lock acquisition. So during the measurement, we were at risk of unlocking the arm cavities, especially as we were working relatively close to the mirror.

Before the measurement, a numerical offset is added with the DAQ software to artificially increase the power read by the photodiode in transmission as shown in figure 8 at the time 510 s. That was mandatory for the measurement since if the transmitted power is too low, the logic of the interferometer control will declare the cavity unlocked and so the locking script will automatically start again.

The screen is held 30 s at each position and the average transmitted power as a function of the screen position is showed in figure 9. The measurement was done for both arms after the NE thermal actuation giving a beam radius of 4.32 cm for the North arm and 4.22 cm for the West arm (with statistical errors around 0.5 mm). That gave a respective end mirror RoC of 3830 m for NE and 3400 m for WE. The WE value is close to what was measured at LMA during the individual characterisation of the mirrors (3410 m), which is coherent since

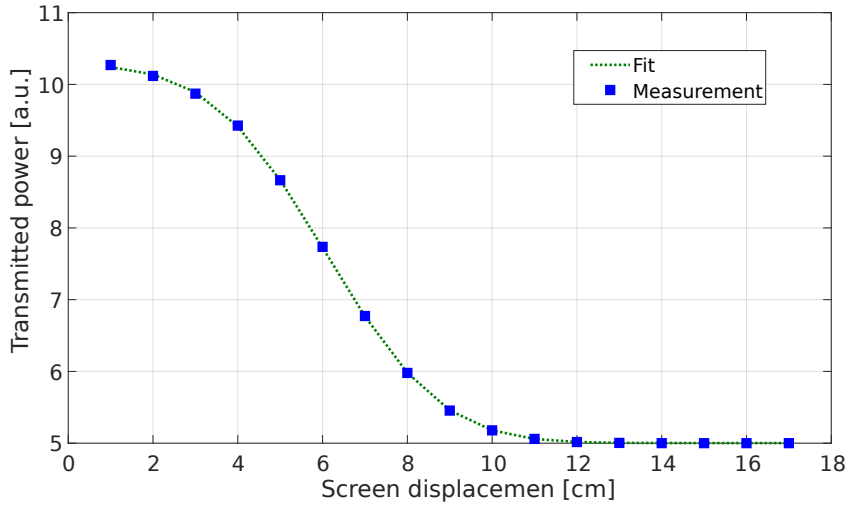

Figure 9: Transmitted power as a function of the screen position. The best fit function (i.e. 2D integral of a Gaussian beam) is also plotted.

no heater was installed for this mirror. However, for the NE, the RoC value is too low, according to the dark fringe power the asymmetry must be much less than what was measured. One explanation is that the heat on the surface of the mirror will create a focusing thermal lens due to the temperature gradient inside the substrate. That would change the beam size at the telescope level.

Even if the measurement was not totally successful, that was an important step to enter in the realm of Virgo. It was my first interaction with the interferometer, a complex machine in a peculiar environment. We still demonstrated the proof of principle of the measurement on very large beams.

Such a measurement was no longer possible in Advanced Virgo, the upgrade of Virgo+ as all the telescopes behind the end mirrors are now in vacuum. To estimate the cavity parameters, the most suitable method is to measure the cavity g-factor as explained in the section 2.5.

2.3 DESIGN OF ADVANCED VIRGO ARM CAVITIES

The years 2009-2012 were the peak of activity to design the new Advanced Virgo interferometer. The goal was to be 10 times more sensitive than the initial Virgo that would allow scanning a volume of space 1000 times more important. Advanced Virgo with its American counterpart were expected to be the first instruments to directly record gravitational waves on Earth and as you know they achieved this remarkable discovery with the first detection for LIGO in 2015 [10] and in 2017 for Virgo [42].

Advanced Virgo was a major upgrade of the Virgo detector, the kind of upgrade which requires a significant budget (order of 20 M€) and several years of shutdown. The detector was profoundly renewed with a higher power laser (up to 200 W), upgraded mirror suspensions, new vacuum cryo-traps and all the optics would have to be exchanged, the central large mirrors but also all the ones on the injection and detection benches.

Thanks to technological progress, the new Advanced Virgo mirrors would be of much better quality compared to the initial ones made 10 years before. The progress cover every aspect of the mirror production: the substrate, the polishing and the coating.

2.3.1 *The constraints*

To design the new arm cavities, one must include from the start any physical limits already present. These constraints already reduce the number of free parameters to explore to obtain the best sensitivity.

The first hard constraint is the length of the cavity fixed by the vacuum infrastructure. So the first parameter, the arm cavity length is fixed to 3 km.

The second constraint in the case of Advanced Virgo was the dimensions of the mirrors. To speed up the project, the fused silica glass ingots were ordered before the completion of the full design. So we already knew in advance that the mirror substrates would be 350 mm in diameter and 200 mm thick, weighing 42 kg.

With these two parameters frozen, the design could start.

2.3.2 *Radius of curvature*

The cavity is made of two concave mirrors, with both Radius of Curvature (RoC) of the High Reflective (HR) surface around half of the cavity length (the concentric resonator geometry). As a first iteration, the geometry must answer two contradicting requirements: to have the beam size as large as possible to reduce the coating thermal noise (see Eq. 3) but without inducing extra clipping loss due to the finite size of the mirrors.

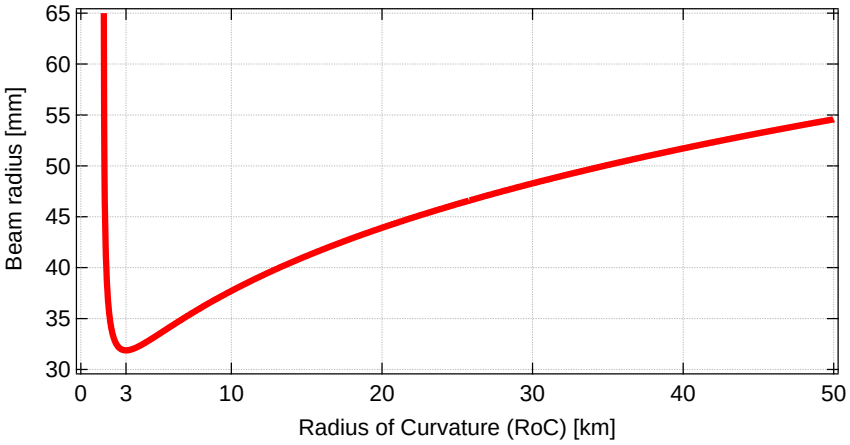

Figure 10: Beam radius on the mirrors as a function of the radius of curvature of the cavity mirrors. The cavity length is 3 km and both mirrors are supposed to have the same radii. The minimal beam radius is achieved when the RoC is equal to the cavity length.

The beam size on the mirrors is minimal when the RoC of the mirrors is equal to the cavity length for a symmetric cavity. So to increase the beam size we have to either reduce the mirror RoC or increase it as shown in the top plot of the figure 10. In theory, the beam size can increase up to infinity with the 2 extreme cases of instability: when the RoC is half the cavity length (mirror g-factor[3] equal to -1 [43]) or when both mirrors are flat (g-factor equal to 1). In those two cases, the cavity geometry can no longer support a stable laser mode (no eigen mode for such resonators) and so is called unstable.

Still from the plot of figure 10, there exists two geometry to achieve a given beam size of the mirror. One with a short RoC (between 1500 m and 3000 m) and one with a longer RoC (above 3000 m). For Virgo and as well as for LIGO and KAGRA, the first solution is chosen to reduce the angular tilt instability linked to the presence of high optical power with suspended mirrors [44].

To precisely find the suitable mirror RoC, it was decided to go for an average RoC of 1551 m to have negligible clipping loss (less than 1 ppm per mirror) in the case of a perfect cavity. The exact value of the RoC is selected to avoid the resonances of higher order modes at the same time as the fundamental mode. Such double resonance called degeneracy is detrimental to the interferometer as high order optical modes have higher clipping loss and also make the control signals less reliable.

However the Virgo arm cavity is not symmetric, the RoC of the Input Mirror is smaller compared to the End Mirror (EM) ones. The motivation is again to reduce the amplitude of the coating thermal noise. The EM being almost perfectly reflective, the coating there is

3 The g-factor of the mirror is defined as one minus the cavity length divided by the mirror radius of curvature: g = 1 - L/RoC.

Table 4: Summary of the arm cavity geometry and mirrors transmission.

		IM	EM
RoC	[m]	1420	1683
Beam radius	[mm]	48.7	58.0
Transmission		1.4%	4 ppm

twice as thick compared to the IM as a result the power spectral density of the coating thermal noise is twice that from the EM (remember the eq. 3). So to reduce the contribution of the EM thermal noise it was decided to make the beam 9% larger there and at the same time reducing by the same amount the beam size on the IM. The summary of the nominal cavity parameters is presented in the table 4.

2.3.3 *Arm finesse*

The addition of the signal recycling mirror in Advanced Virgo allows much more flexibility in the optimal choice of the finesse of the arm cavities. Indeed, without it, the frequency bandwidth of the detector constraint by the science goals is only set by the finesse of the arms, which means for a given sensitivity curve, we have a fixed value for the arm finesse.

With signal recycling, the optical response of the detector is changed and depending on the microscopic position[4] of the signal recycling mirror, the bandwidth of the detector can be tuned. In that case, the finesse of the arm cavity is more an open choice depending on other criteria than just the detector bandwidth.

The choice of the finesse is not obvious as it depends on several considerations. As an example, a high arm cavity finesse could reduce the thermal load in the central interferometer as less circulating power would be required on the beamsplitter. However a high finesse arm cavity would be more difficult to lock and the round trip losses would have more impact.

Finally, the finesse was decided to be 450 [45], same as Advanced LIGO, leading to a IM transmission of 1.4%.

2.3.4 *Arm round trip loss*

The light Round Trip Loss (RTL) in the arm cavity is one of the most critical optical parameters for a GW detector. It quantifies the amount of optical loss when the laser does one 3 km round trip in the arm cavity. The RTL does not include the transmission of the input mirror

4 The microscopic position sets the resonance condition of the light in the signal recycling cavity.

Table 5: Cavity gain, arm cavity reflected power and power recycling gain as a function of the RTL. The following parameters have been used: arm input mirror transmission is 0.014, the arm end mirror is perfectly reflective (cavity finesse 446) and the power recycling mirror transmission is 0.05 (AdV nominal parameters).

RTL [ppm]	CAVITY GAIN	REFLECTED POWER[a] [W]	RECYCLING GAIN
0	284	1	78
75	281	0.978	39
150	278	0.958	24

[a] The reflected power is normalised to 1 W of input power for the arm cavity.

as the light exiting the cavity by the input mirror is not lost but stays in the detector and contributes to the power recycling gain.

The RTL is typically a very small number, less than 0.01%. It is highly dependent on the surface quality of the mirrors. Indeed, a bad mirror surface means higher optical losses due to excess scattered light and so less circulating power in the arms. A second consequence is also to decrease the light power reflected by the cavity so it has a direct impact on the recycling gain. To understand the impact of the Round Trip loss (RTL) on the arm circulating power one can do a simple simulation with 3 different theoretical cases: perfect surfaces for the arm cavity mirrors (RTL = 0 ppm[5]), with outstanding coating and polishing (RTL = 75 ppm) and with double RTL compared to the previous case (RTL = 150 ppm). The results are shown in table 5.

One can see in table 5 that there is a double penalty to increase the arm round trip loss. The first one is a decrease in the arm cavity power gain as the finesse is decreased and the second one is a much sharper decrease in the power recycling gain. The circulating power in the arm is proportional to the product of both gains, as an example with only 75 ppm of RTL, the arm cavity circulating power will drop by half compared to the utopian case of no loss.

The specification for the arm RTL for Advanced Virgo was indeed set to 75 ppm (also the same as Advanced LIGO). It is a crucial number but the way to select it is a mix of realistic expectation and arbitrary threshold. The RTL of 75 ppm allows excellent performances of the interferometer and meanwhile this loss could still be achieved with state of the art polishing and coating. This value has now been validated and became a standard as it is also used for the design of Advanced Virgo+ as well as for the Einstein Telescope at the time of writing.

From the 75 ppm maximum loss, we estimated that 4 ppm will be from the EM coating transmission and 1 ppm from the coating optical

5 ppm stands for part per million, it is equivalent to 10^{-6}.

absorption. That left us with 70 ppm due to scattered light and that is directly related to the surface quality which is the topic of the next section.

2.3.5 *Surface quality*

The surface of the substrate refers to the surface height measured from an arbitrary plane. For convenience, for curved surfaces, the average curvature is subtracted and so the remaining landscape, the surface error is made of bumps and dips of different heights and spatial extends. The piston term is also removed so the average surface height is set to zero.

Regarding the optics surface, two main specifications are derived: the flatness and the roughness levels. Both represent surface height specifications but on different spatial scales. The flatness is on the low spatial frequency (large mountains on the surface) whereas the roughness concerns the high spatial frequency (much smaller features). The spatial frequency border between the two specifications is rather fuzzy and is set in practice by the characterising instruments.

On one hand, the flatness is measured by a Fizeau type of interferometer [46] where the surface to be measured is compared to a reference surface. Such instruments are sometimes called a "Zygo interferometer" from the eponymous ubiquitous brand. One such example is shown in the figure 11 on the left, the aperture is 450 mm diameter, the lateral resolution is 0.4 mm and the surface height repeatability is around 0.3 nm [47].

On the other hand, the roughness is measured by an optical profilometer, it is also an instrument based on interferometry but that time, the reference surface is usually within a microscope objective. The field of view is much smaller typically less than 1 mm^2 (lateral resolution of 1 µm for the smallest magnification) and height accuracy is sub-ångström. The device at LMA is shown in the right part of figure 11.

To go further in the design, one has to do the decomposition of the RTL over the different sources of optical losses. We knew the total loss should be 75 ppm and based on experiences and simulations we decided on the following RTL budget: the majority of the losses, 50 ppm should come from the flatness, 20 ppm from the roughness and the remaining 5 ppm includes the EM transmission and the coating absorption.

2.3.5.1 *Flatness*

To simulate the impact of the surface flatness on the losses in the cavity, optical simulations using realistic 2D surface height maps of the mirrors were developed. The codes are based on the ability to simulate any arbitrary electric fields (a laser beam) inside the cavity and

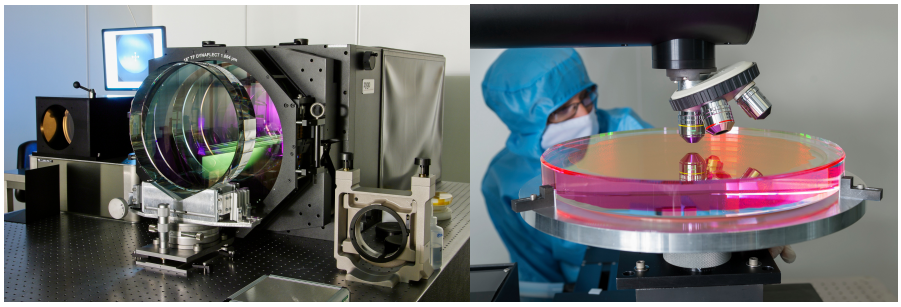

Figure 11: Photos of the two main instruments to characterize the flatness (left) and the roughness (right) of the substrate or mirror surfaces. The left instrument is a wavelength shifting Fizeau interferometer from the brand ZYGO with a 450 mm aperture. The right one is a custom made optical profilometer with different objectives. Both instruments have a working wavelength of 1064 nm and are installed in the clean room at LMA. Photo Credit: me (left) and Cyril Fresillon CNRS Photothèque (right).

not only a perfect fundamental Gaussian mode. The inner working of such simulation is described in the article on page 135 for the code OSCAR and so I will not come back on it.

So to derive the flatness specifications, we created virtual mirror maps with different surface heights that we included inside the simulations of the arm cavity, one surface map on each mirror. Good polishing means mirrors with low surface flatness and so low round trip losses. The quality of the surface flatness is quantified by the RMS over a central diameter. In the case of Advanced Virgo, the central diameter is 150 mm, corresponding to about 3 times the laser beam radius on the mirrors. In the central diameter is located the majority of the laser power (99%) and so that is where the most stringent specifications are defined.

The virtual mirror maps are not random, they follow a certain PSD (a 1-D spectra to quantify the height of the surface errors according to their spatial frequencies). The PSDs are usually derived from surface measurements from pathfinder optics or previous polishing works. That is why it is important to ask companies past achievements and to not rely only on what they think they could achieve.

The intellectual approach at the time of the design of Advanced Virgo (2010-2011) is well described in Romain Bonnand's PhD thesis [48] chapter 3, so I will only remind here the main messages:

- the PSD of a polished surface depends on the polishing process. Different companies will produce surfaces with different PSDs even if the final peak to valley or RMS are similar.
- The cavity round trip loss as a function of the surface flatness (quantified for example by the RMS) will depend on the PSD.

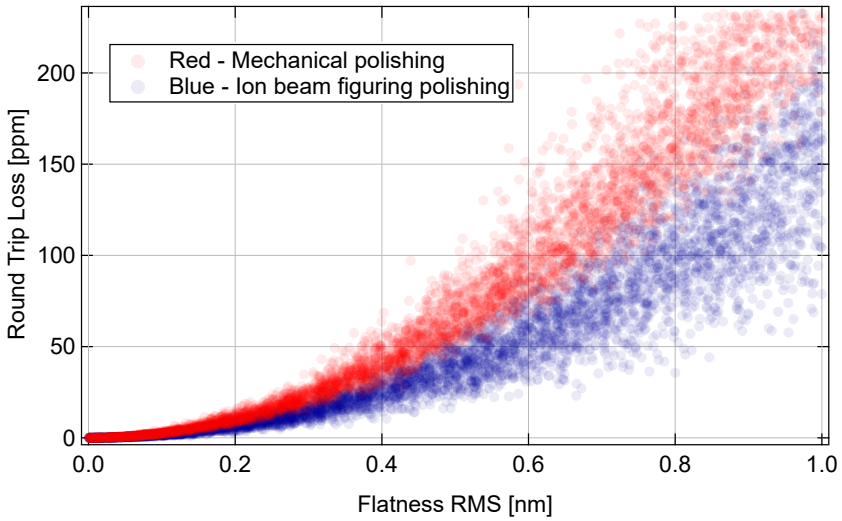

Figure 12: Arm cavity simulations for the Advanced Virgo geometry. The RTL versus the flatness of the mirrors is shown for 5000 simulations. Two different realistic PSD has been used. For those simulations, the PSD shape is assumed to be independent of the flatness level.

- For Advanced Virgo, the flatness of the arm cavity mirrors must be less than 0.5 nm RMS in the central diameter of 150 mm.

To illustrate the above statements, we did a Monte-Carlo simulation of 5000 random mirror flatness and recorded the RTL. The results are presented in figure 12. For each simulation, both input and end cavity mirrors have surface maps with the same PSD and the same RMS. The 5000 different flatnesses are taken uniformly between 0 and 1 nm RMS. As expected, the higher the flatness, the higher the round trip loss of the cavity.

The plot shows the RTL for 2 different PSDs of the mirror surface, as we can see the loss depends on the PSD shape. The 2 PSDs are from two different polishing techniques. The first one is from standard mechanical polishing while the other one uses Ion Beam Figuring (IBF). IBF is complementary to traditional polishing and is the ultimate polishing step where all the bumps at the surface of the substrate are selectively removed (or sputtered) by a focused ion beam [49]. Those results are from a simulation exercise as any arbitrary low level of flatness can not be achieved on real optics. In practice, on large surfaces, very low surface flatness (below 0.5 nm RMS) can only the achieved with the IBF technique.

From figure 12, we can deduce that to have consistently less than 50 ppm of RTL due to the flatness of the mirror, it is recommended to use IBF polishing with a flatness requirement less than 0.5 nm RMS in the central part.

We can simulate the beam size, RTL and arm cavity gain as a function of the radius of curvature of the mirrors assuming a symmetric

cavity. The results are presented in figure 13 for the region of interest. As seen previously in figure 10 for RoC closer to 1500 m, the cavity becomes unstable and the laser beam size on the mirrors grows infinitely large, increasing the RTL due to the finite size of the mirrors.

What is more of interest is the region around a RoC of 1600 m, similar to the cavity geometry of AdV. Adding a surface map with a flatness of 0.5 nm RMS on both mirrors, increases the RTL from less than 1 ppm to 30 ppm. This result is expected as it is the average RTL value for such surface quality as seen in figure 12. As we can notice on the beam size and the cavity gain, top and bottom plots, adding realistic outstanding surface maps have no impact on those parameters, we are still dominated by the cavity geometry. So the natural question is: are we too stringent about the flatness specification ? therefore adding unnecessary cost and delay to the project ?

The above question is a very valid point, if we consider only a single Fabry-Perot cavity. However, in the case of a GW detector, there are two arm cavities that we must recombine as well as a recycling cavity which is coupled to the arms. So another figure of merit is the power reflected by the arm cavity in the fundamental TEM_{00} mode that is shown in figure 14. We project the reflected beam on the fundamental mode, as it is the beam with the optimal coupling to the other parts of the interferometer: recycling cavities but also the output mode cleaner.

With figure 14, we can see a more worrisome story. Even with outstanding mirror surfaces and with a RTL of only 30 ppm, in reflection of the arm cavity 1% of the light is lost, reducing the recycling gain. More alarming, dips in the reflected power are present for some RoCs, in that case, the cavity is degenerated, higher order modes can resonate at the same time as the fundamental one increasing the RTL and reducing the power in the TEM_{00}. For those simulations, we assumed a perfect alignment and mode matching, so we could expect to have very little chances to excite higher order modes but that is not the case. So even with the optimal conditions of a perfect input laser beam and state of the art polishing, the cavity degeneracy must not be underestimated. Such effects of the degeneracy have recently been experimentally demonstrated in a long suspended cavity [50].

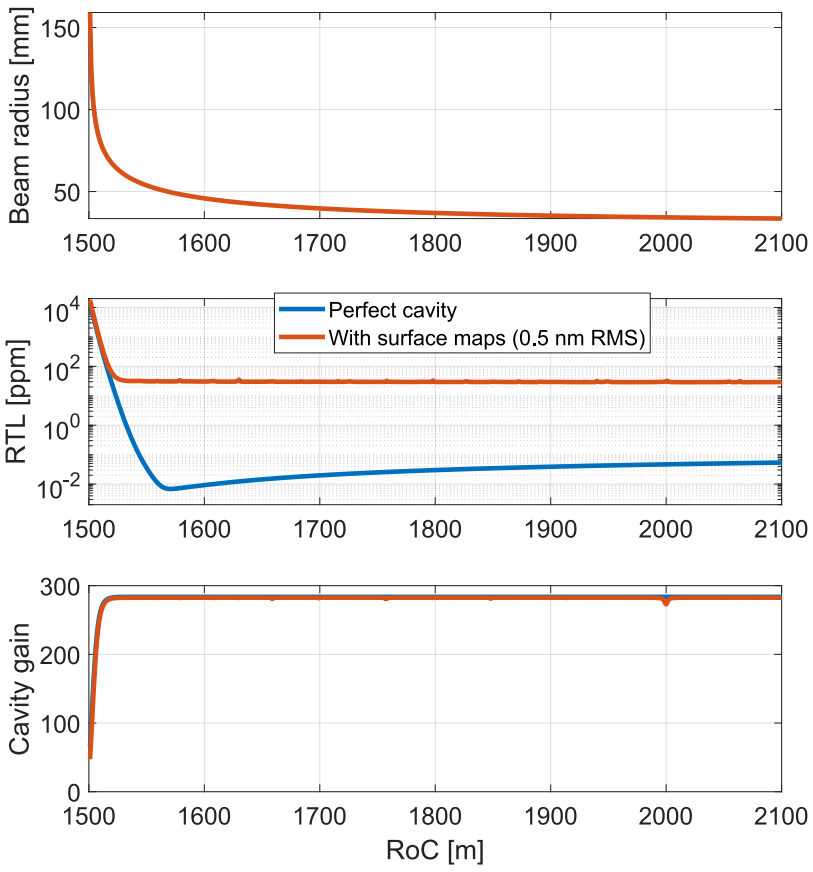

Figure 13: From top to bottom: beam radius of the laser beam on the mirror, cavity Round Trip Loss (RTL) and the cavity power gain as a function of the radius of curvature of the mirrors assuming a symmetric cavity. For the top and bottom plots, the results with and without surface maps are superimposed. It is interesting to note that the minimal loss for the perfect cavity is not achieved for the minimal beam size on the mirror. The reason is not currently understood by the author. For those simulations, the input beam parameters are adjusted to ensure optimal mode matching and alignment for every cavity geometry.

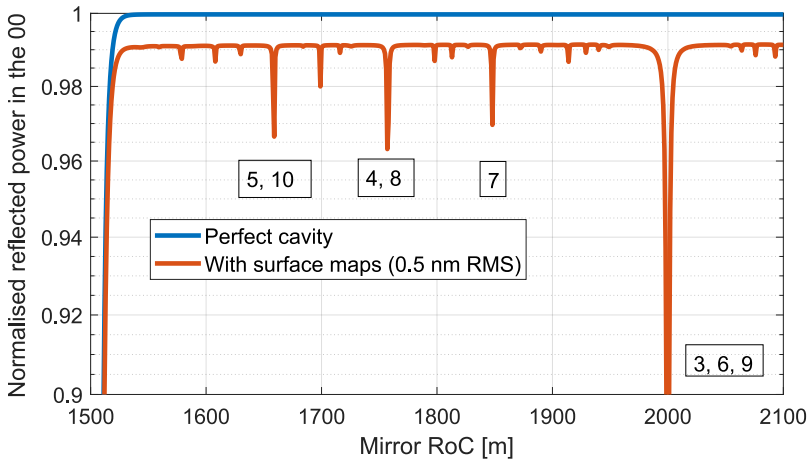

Figure 14: Normalised power reflected by the cavity projected to the fundamental mode as a function of the RoC of the mirrors. The orders of the optical modes resonating at the same time as the fundamental are shown in the boxes. The cavity degeneracy for certain RoCs induces a strong loss in the cavity reflected power in the fundamental mode.

2.3.5.2 *Roughnesss*

As a reminder, the roughness encompasses the surface defects with high spatial frequencies (typically, defects with less than 0.1 mm lateral scale). When hitting such defects, the light is scattered at large angles (compared to the ratio of the mirror diameter over the cavity length) and so it is directly lost. The amount of light lost is directly proportional to the RMS of the surface according to the total integrated scatter law [51]. More precisely, the amount of light scattered $\mathcal{L}$ by a mirror of roughness σ RMS is given by:

$$\mathcal{L} = \left(\frac{4\pi\sigma}{\lambda}\right)^2 \tag{6}$$

with λ the light wavelength (1064 nm in our case). For advanced Virgo arm mirrors, the specification for the roughness was to be below 0.1 nm RMS in the central part. That would give a loss between 1 and 2 ppm of loss per mirror according to formula 6. This specification could have been relaxed according to the loss budget but we decided to go for the best which could be achieved by state of the art polishing.

2.3.5.3 *Defects*

A specification also existed regarding the cosmetic defects given as the maximum integrated area or total numbers allowed according to their sizes. Those are punctual anomalies on the surface different from the overall roughness background. For example, in the central diameter of 150 mm, the total number of defects of size between 5 µm and 50 µm must be less than 15 [52].

I did not participate to the writing of those specifications so I can not comment on them. As far as I understand, it is a rather a rough hand model, assuming that the total integrated area of the defects is considered as a pure optical loss.

2.3.5.4 *Final words on the polishing specifications*

A large part of the polishing work for the substrates of Advanced LIGO mirrors was already completed at the time we were calculating the specifications for the AdV ones. That revealed to be extremely useful as it demonstrated the best polishing which could be achieved at that time and it inspired us on several calculations.

So at the end, the specifications were a mix of requirements from optical simulations and realistic expectations of what could be practically manufactured. Both information must be blended smoothly to achieve an interferometer compatible with the science goal and also to have the optics in a limited amount of time and budget. Also, as a matter of fact, when looking for polishing companies, do not hesitate

to ask them for results from previous work similar to your demands. That gives precious input to achieve realistic simulations.

2.3.6 *Coating specifications*

The second large class of specifications is for the coating itself, the thin layers of materials which will give the optical function to the block of polished glass. The main specifications are given from the cavity finesse we would like to achieve, a compromise between detector sensitivity and bandwidth, optical loss and recycling gain. The arm cavity finesse was decided to be 450 (similar to Advanced LIGO), the number itself has nothing spectacular as finesse 1000 times higher could be achieved in the lab albeit on much smaller cavities.

2.3.6.1 *Mirrors transmission*

The finesse of the cavity is given by the transmission of the input mirror as the end mirror is almost perfectly reflective. To achieve a finesse of 450 (power gain of 280), the transmission of the input mirror has to be (1.4 ± 0.1) % at 1064 nm. It could be compared to the 75 ppm (0.0075%) of round trip loss, meaning that thanks to this relatively low finesse, the expected optical losses are not degrading the finesse of the cavity.

The end mirrors have a transmission of (4 ± 1) ppm so a small fraction of the light is transmitted by the cavity and can be used for diagnostic and for the locking procedure.

Those are the transmissions for the main infrared laser but specifications also existed at other wavelengths, for example at 532 nm to have even a lower cavity finesse to control the cavity with auxiliary green lasers.

Both input and end mirrors have also an anti-reflective coating on the side of the substrates outside the arm cavity. Ideally there the reflection should be zero which could only be achieved in theory. So one more time, we went for the state of the art and the specification for the AR reflectivity was set to be less than 100 ppm at 1064 nm.

2.3.6.2 *Managing very low optical loss*

It may seem like evidence but the coating should not degrade the excellent polishing work, so the surface quality must stay the same for the flatness and roughness, in particular over the central part.

For the roughness, that was not an issue as the technique of Ion Beam Sputtering (IBS) used at LMA, allows very low loss optics and the roughness is preserved even after several micrometers of coating.

To keep the overall flatness is more challenging and required an extensive tuning of the coating machine to improve the uniformity of the deposited layers. At the end on the central part, the flatness is

only increased from 0.3 nm RMS to 0.4 nm RMS after adding 6 µm of coating. At larger diameter, we can notice the coating thickness falls off at the edge of the mirror by several tens of nanometers as shown in figure 4 of the article page 125. However, the impact of this fall-off is minimal as it happens outside the central diameter where 99% of the power of the laser beam is.

The coating should also have very low optical absorption at 1064 nm. That is to limit thermal aberrations in the arm cavities due to thermal expansion of the high reflectivity surface as hundreds of kW of light will be circulating during normal operation. Also, the coating absorption is responsible for the thermal lens in the substrates of the input mirrors, adding wavefront aberrations inside the recycling cavities.

From thermoelastic simulations, the optical absorption requirement for the coating has been set to be less than 0.5 ppm (5×10^{-7}) for 1064 nm. That is a very small number but even with such a low absorption, a complex thermal compensation system is required to ensure an aberration free interferometer [25].

The optical absorption as well as the coating mechanical loss responsible to the coating thermal noise level put severe constraints on the materials for the coating. After several years of test and optimisation, the coating material was selected to be fused silica (SiO_2) for the low refractive index material and tantala doped with titania (Ta_2O_5-TiO_2) for the high index one [24].

2.4 PROCUREMENT OF THE MIRRORS

To give a sense of the timescale to the reader, the history of the production of the mirrors of Advanced Virgo is detailed in this section.

2.4.1 *Substrate procurement*

The final dimensions of the mirrors were decided at an early stage. Those were not free parameters since it was decided to keep the diameter constant between Initial Virgo and Advanced Virgo (350 mm) while the thickness would be doubled to 200 mm. We could think of the thickness of a mirror as not much relevant but that is wrong as for the second generation detector, the total mass of the mirror is a critical parameter regarding the radiation pressure noise (remember equation 4 in chapter 1).

Following preliminary optical characterisation done at LMA on samples of various grades of fused silica, it was demonstrated the excellent properties of the Suprasil material from Hereaus. In particular, extremely low optical absorption could be achieved (below 0.5 ppm/cm for Suprasil 3002/1) which is crucial for the beamsplitter and the IM, the optics used in transmission inside the recycling cavities.

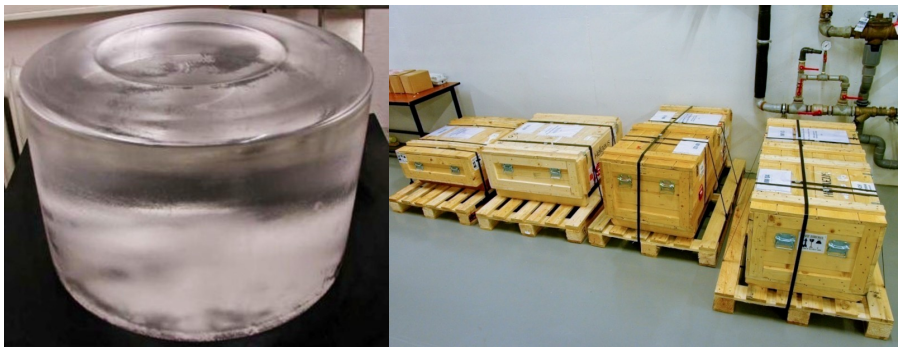

Figure 15: Photo of a IM substrate after the final forming step at Heraeus (left), so before any saw cutting. Example of shipment boxes for the substrates (right), ready for world-wide expedition. Photo credit : Heraeus and Laurent Pinard.

So all the fused silica blanks were ordered at the beginning of 2010 from Heraeus. For the arm cavities, that means 4 IMs and 4 EMs substrates, 2 to be installed on site and 2 to have a set of spare mirrors. For illustration, an example of the glass substrate, straight from the oven is shown in figure 15. The first 2 IMs arrived 6 months after the order and then at the beginning of 2011, all the required 8 parts were at LMA.

The substrates were ordered well in advance since at the beginning of 2011, the polishing specifications were not yet finalised.

2.4.2 *Polishing procurement*

Following the simulations presented at the beginning of this chapter and after a stage of reviews, the polishing specifications were ready in summer 2012 (an example of the final document, accessible to Virgo members can be found here [52]). To find the most suitable polishing companies, meeting all our criteria, a global call for tender was issued with different lots for all the core large optics. It is a rather lengthy procedure with a rigid framework as the amount of money involved is in the order of millions of euros.

At the end of 2012, four offers were received and compared based on technical performances, prices and production time. The company ZYGO was officially awarded the contract in February 2013. Zygo has a solid experience since they have already polished the substrates for Advanced LIGO few years before with similar dimensions and specifications. Moreover, this company has 2 production sites allowing parallel processing. So all the parts with curved surfaces were sent to the US West Coast (California) whereas the flat parts (beamspitter, compensation plates) were manufacturered in the East Coast (Connecticut).

The first two IM polished substrates were received and accepted at LMA in November 2013, by summer time of the following year 2

EMs arrived and by the end of 2015 all the polished parts (including spares) were delivered at LMA.

2.4.3 *Coating deposition*

The coating for such exceptional optics was really a challenge with research and development lasting several years at LMA on the optimisation of the coating materials but also to improve the uniformity inside the coating chamber [53, 54].

The coating process started in autumn 2014 for the IMs and spring 2015 for the EMs. The coating and the following optical characterisation to get a full mirror (so with both the HR and the AR sides) takes around one and half month. After the coating process, the team from the Virgo payload group went to LMA to glue the ears on the side to later attach the suspension glass fibers.

At the end, the arm cavities mirrors were installed on site in summer 2015 for the IMs and end of 2015 for the EMs. So it was a journey of five years for the procurement and installation of the most critical mirrors of the detector.

2.5 CHARACTERISATION OF THE ADVANCED VIRGO ARM CAVITIES

Each mirror is individually optically characterised at LMA, the measurements include: radius of curvature, flatness, roughness, defects, scattering absorption and transmission with lasers at 1064 nm. Those are not single point measurements but a 2D cartography of the parameter is made over the central diameter to check the uniformity. Examples of such maps are presented in the article page 125 which summarise the performances of the Advanced Virgo mirrors. For each optic, a formal acceptance report is also written for reference (see for example the one for the EM-01 [55] available for people within the Virgo collaboration).

After the mirrors are installed on site, it is also essential to check the in-situ performances of the optical cavities. In that case, we can no longer characterise each mirror individually but we look at the global behavior of the optical cavities (which heavily depends on the mirror quality of course).

In the following paragraphs, we will focus on the most relevant parameters of the arm cavities:

2.5.1 *Round Trip Loss*

Likely the most critical parameter as highlighted before, the RTL is the light lost by the cavity during one round trip and excluding the transmission of the IMs (but including the absorption and the

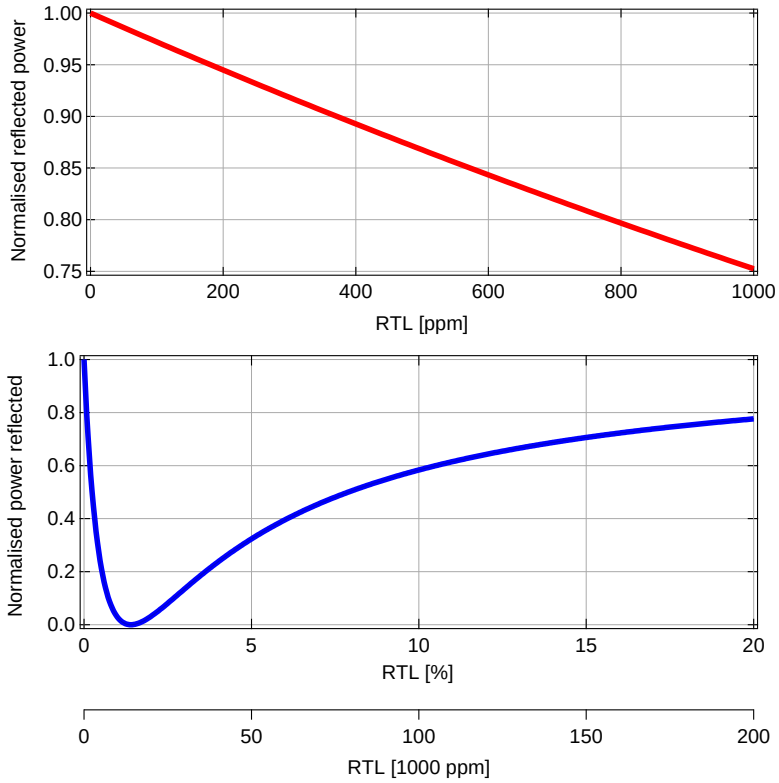

Figure 16: Reflected power as a function of the round trip loss for small losses (top plot) and for substantial losses (bottom plot). In the case of GW detectors thanks to the outstanding mirrors, the losses are less than 100 ppm so the top plot applies. The bottom plot is there for completeness, to be noted the situation when the reflected power is null (critically coupled cavity), that happens when the losses are equal to the transmission of the input mirror (1.4% in the Advanced Virgo case).

EMs transmission). In the case of a perfect cavity, without any loss and since the end mirror is perfectly reflective, all the power must be reflected back from the cavity. So in that case, in resonance (cavity locked) or out of resonance (cavity unlocked), the reflectivity (in power) of the cavity is always 1. As soon as small optical losses are introduced, the reflected power decreases linearly when the cavity is on resonance as shown in figure 18.

Even for low RTL, for example 50 ppm, the effect is already noticeable with the reflected power decreasing by 1.4 %. So to measure the RTL, we successively lock and unlock one cavity and monitor the normalised reflected power.

So the measurement itself is quite simple, since it is a relative measurement we look at the reflected power with the same photodiode when the cavity is unlocked and locked as shown in figure 17. When the cavity is unlocked (and not flashing), the reflected power is equal to the incident power, which is assumed to be also the reflected power

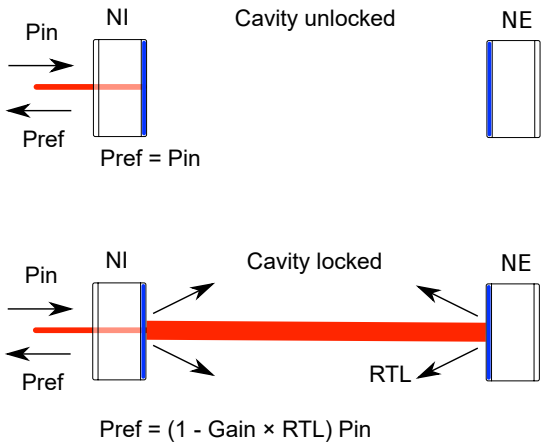

Figure 17: Principle of the RTL measurement when the arm cavity is successively locked and unlocked.

when there is no loss in the locked cavity. Then we lock the cavity and the reflected power decreases, the drop in power is directly related to the RTL as shown in the top plot of figure 18. Since it is a relative measurement, we do not need to know the optical losses between the cavity and the photodiode used for measurement, that is the strong advantage of this technique.

As demonstrated in 2.7.3, for small losses, the reflected power is linearly decreasing as the losses are increased as shown in the top plot of the figure 18. Interestingly, the decreasing slope is the power gain of the cavity.

A measurement for the north arm RTL is shown in figure 18. The cavity is successively locked and unlocked around 1 minute each time and the decrease in reflected power is clearly seen when the cavity is locked.

Averaging the values found in figure 18, we can deduce that the reflected power while the cavity is unlocked is $P_{ref}^{unlocked} = 0.02944$ and while locked it is $P_{ref}^{locked} = 0.02904$. So following equation 34 (demonstrated later in section 2.7.4):

$$RTL = \frac{T_1}{4}\left(1 - \frac{P_{ref}^{locked}}{P_{ref}^{unlocked}}\right) \tag{7}$$

and with $T_1 = 1.4\%$ we can deduce the RTL to be equal to 47 ppm, so well within the specification to be less than 75 ppm.

Another way to look at this measurement is presented in figure 19. The plot was made by Annalisa Allocca while I was the coordinator of optical characterisation for Advanced Virgo.

The same experiment as before is done, recording the reflected power while the cavity is locked and unlocked. But this time, the data is not viewed as a time series but as a histogram of reflected power values to see the variance of the measurement. Also a third

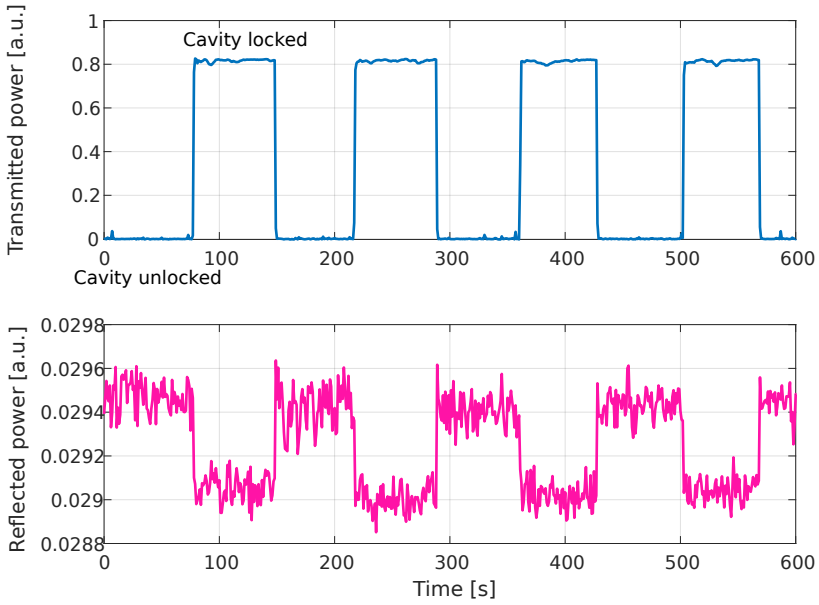

Figure 18: Lock and unlocked of the North arm cavity. The transmitted power is shown in the top plot, whereas the reflected power is shown in the bottom plot. The data are downsampled to 1 Hz, the values are all relative but what is relevant is the ratio between the reflected power in the locked and unlocked state.

case has been added: the cavity is unlocked but with the end mirror misaligned, so the cavity is not flashing and in that case, the reflected power is simply the reflectivity of the input mirror.

In the figure 19, the reflected power when the cavity is unlocked has been normalised to 1, that is the orange distribution on the right. Then there is the yellow distribution in the middle which is when the cavity is misaligned with the end mirror, in that case we found the normalised reflected power to be 98.6 %, the nominal reflectivity of the input mirror, a good sanity check. Finally when the cavity is locked the normalised reflected power is 0.9834, leading to a RTL of 58 ppm.

This plot is quite synthetic as the RTL values can be directly read in the top horizontal scale, highlighting one more time, the linear relation between reflected power and RTL.

The 2 measurements presented here of the RTL are separated by 3 years with different operating points of the interferometer, in particular different alignment, which could explain the difference in the value measured between the 2 arms. Usually, in the same conditions, the 2 arms give similar RTL within 10 %, which is also the typical error bar of such measurement.

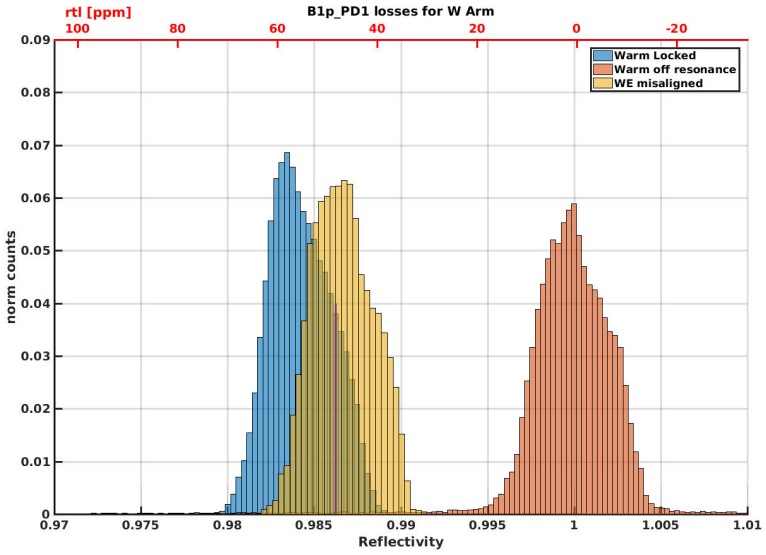

Figure 19: Measurement of the RTL in the west arm with the shape of a histogram of the arm cavity reflectivity. The corresponding RTL is shown in the horizontal top axis. This plot has been extracted from the Virgo logbook [56].

2.5.2 *The finesse*

It is also possible to measure in-situ the finesse of the arm cavities. The finesse value is largely determined by the transmission of the input mirror as other kinds of optical cavity losses are negligible in front of the 1.4 % transmission of the IM. The finesse is calculated by scanning the cavity over several Free Spectral Range (FSR). For that, the damping of the EM suspension is not activated and a gentle kick is given to the mirror to make it free swinging.

Due to the very low linewidth of the cavity, the cavity resonance is passed very quickly, faster than the light buildup time. In that case, the fundamental mode resonance is not appearing like a classical Airy peak in transmission but it looks like dampened oscillations [57]. By fitting the shape of the transmitted power, one can derive the finesse of the cavity but also the speed of the mirror, an example of such fit is shown in figure 20.

The various measurements have shown a finesse between (464 ± 7) ppm and (455 ± 6) ppm respectively for the North and West arms [59]. It is in the range of the expected value of 450 and the difference between the 2 arms may be explained by the etalon effect (uncontrolled at that time) in the input mirrors, slightly modulating the effective transmission of the mirrors.

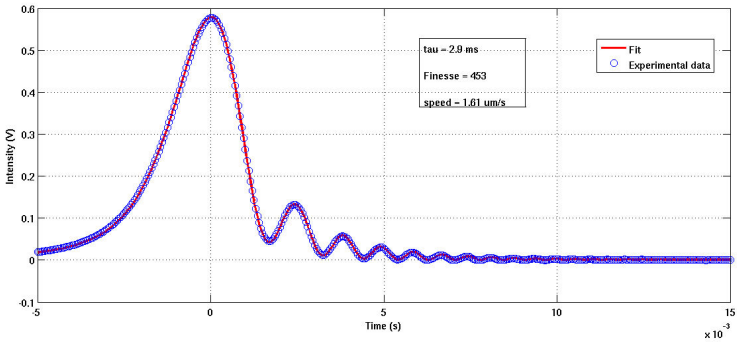

Figure 20: Example of the resonance peak of the fundamental mode during the scan of the cavity. The power is measured in transmission of the cavity and we can clearly see the ringdown due to the fast scanning rate. This example was made by Annalisa Allocca and can be found in the Virgo logbook [58].

Table 6: Relative resonant positions of some higher order modes in unit of the FSR. For comparison, in the same unit, the linewidth of the cavity (defined as full-width half-maximum of the FSR scan) is the inverse of twice the finesse so 0.001.

$(m+n)$	$\Delta Pos_{(m+n)}$ [1/FSR]
1	0.117
8	0.937
9	1.054

2.5.2.1 *The cavity g-factor*

During the scan of the FSR, one can also notice the resonance positions of the higher order modes in the cavity. The relative position of the modes within the FRS is directly linked to the RoC (or g-factor) of the IM and EM by the formula [60]:

$$\Delta Pos_{(m+n)} = \frac{m+n}{\pi} \arccos \sqrt{(1 - L/RoC_{IM})(1 - L/RoC_{EM})} \quad (8)$$

where ΔPos is the relative separation between the fundamental mode and the mode of order (n+m) normalised by the FSR of the cavity. L is the length of the cavity and RoC_{IM} and RoC_{EM} are the radius of curvature of respectively the input and end mirrors. The cavity is degenerated with the resonance of the mode of order (m+n) at the same time as the fundamental mode when $\Delta Pos_{(m+n)}$ is an integer (or close by). A quick calculation of the relevant $\Delta Pos_{(m+n)}$ for some relevant modes is shown in the table 6.

From table 6, one can notice that the resonance of the fundamental mode in the arm cavity for the nominal curvature of the mirrors,

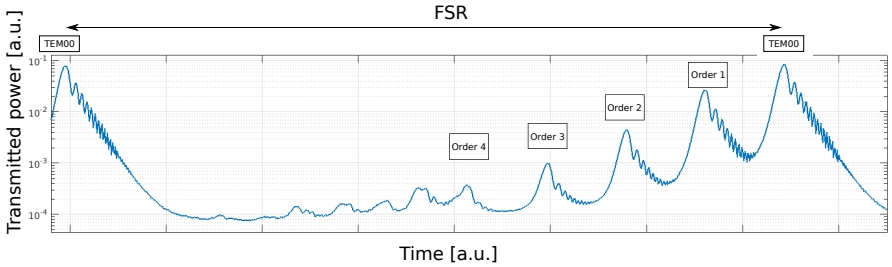

Figure 21: Transmitted power of the cavity during one scan over a FSR, the first mode orders are written above the transmitted peaks. The plot is taken from the Virgo logbook and made by Annalisa Allocca [61].

lies between the resonances of the higher order modes of order 8 and 9. That means in case of imperfections, it is likely the higher order modes we would find in the interferometer, in particular, visible at the dark port where the fundamental mode is absent due to the destructive interference at the beam splitter.

A scan of the cavity over one free spectral range is shown in figure 21.

To achieve the scan presented in figure 21 several precautions have to be taken:

- the modulation depth of the control sidebands (at frequencies of 6 MHz, 8 MHz and 56 MHz) are reduced as much as possible to avoid additional peaks during the FSR scans. For testing purposes, the sidebands may be present and since their frequencies are well known they are used to crosscheck the scaling of the horizontal axis [62].

- to enhance the resonance of higher order modes, the cavity is slightly misaligned. So before the measurement, the end mirror is tilted by 1 µrad.

- to reduce the distortions of the shape of the resonance peaks, not all mirror speeds are considered in the analysis. To reduce the error bars in the estimation of the positions of the transmitted peaks, it was decided to only take into account the peaks when the speed is between 0.3 µm s^{-1} and 0.55 µm s^{-1} [63].

The results from one scan are presented in table 7, in this case for the North arm but the conclusion is identical for the West arm. First, the simulation is tuned to match the measured mode spacing ΔPos_1 and ΔPos_2 without the heating ring acting on the end mirror. That is the difference between what I call the Realistic and Tuned configurations (third and fourth rows). To match the measured mode spacing at Virgo in the simulations, both IM and EM RoCs have to be decreased by 3 m compared to the measurement done at LMA.

Table 7: Simulations and measurement [64] of the relative resonance positions of the modes of order 1 and 2 with respect to the fundamental mode, in unit of the FSR for the North arm cavity. The statistical error on the mode spacing measurement is typically of the order of 1%.

CONFIGURATION	ROC IM [m]	ROC EM [m]	ΔPos_1 [1/FSR]	ΔPos_2 [1/FSR]
Simulations				
Nominal	1420	1683	0.117	0.234
Ordered[a]	1425	1691	0.124	0.248
Realistic[b]	1425	1695	0.125	0.252
Tuned[c] RH off	1420	1690	0.122	0.246
Tuned[d] RH on	1420	1670	0.112	0.225
Measurement				
RH off			0.122	0.246
RH on			0.112	0.225

[a] The central mirror RoC specifications asked to the polisher. It has been shifted from the nominal value to take into account the thermal effects and their corrections.

[b] Simulations done using the measured RoCs, including the 2D surface maps measured after coating.

[c] IM and EM RoCs decreased by 5 meter to match the measured cavity g-factor in case of the Ring Heater (RH) off.

[d] The ring heater on the EM is switched on to reduce the RoC of this mirror. So we assume identical IM RoC as when the RH is off and that the change of the mode spacing is only due to the change of the EM RoC.

We assume the same RoC error on both IM and EM as a systematic effect during the characterisation phase, for example: incertitude in the RoC of the reference sphere of the Zygo interferometer, effect of suspending the mirror in Virgo or different temperatures at LMA and at the site.

The same characterisation is also done with the Ring Heater (RH) switched on the EM. The heating ring is a cylindrical heating element positions around each of the two arm cavity mirrors and is used to fine tune the RoC of the mirrors and compensate for thermal defects. In that case, the heating ring was switched on to reduce the higher order mode content at the dark port. The effect on the mode spacing is clearly visible indicating the effective change of the EM RoC. By matching the simulation to the measurement, we can deduce that the RoC of the EM was decreased by 20 m.

2.5.3 *Thermal transient*

So far the characterisation described in this chapter was done with a single cavity locked and without the recycling cavity so that means with low power circulating in the arm cavities (less than 200 W). That is very different when the interferometer is on its operating point at the dark fringe and with the recycling cavity, in that case, more than 100 kW of light is circulating in the arms.

The effect of the high power can be noticed as the cavity circulating power decreases right after the lock and reaches a steady state within 200 s. The drop in power will depend on the input power of the interferometer and can reach up to 30% for 25 W at the entrance of the power recycling cavity.

By analysing the evolution of the reflected and dark port powers of the interferometer and other monitoring signals, it was deduced that the power drop is not linked to a worsening of the mode matching or the alignment. The culprit seems to be an increase in the arm round trip loss [66]. Such phenomena could be explained by the presence of few absorbing points in the coating as also seen by LIGO [67]. By increasing the laser power, the height of a thermoelastic bump at the surface of the mirror will also increase, leading to additional light scattered into higher order modes. The effect is enhanced by the presence of the resonance of one higher order mode close the resonance of the fundamental one.

Monitoring the power at the different ports and with the help of the interferometer model, it is possible to derive the round trip loss of the arm cavity as a function of the input power. Such a plot is presented in figure 23.

As expected the RTL starts at 55 ppm at very low power, it is the typical value we measured when we only lock one cavity. Then when the full interferometer is locked and the circulating power is max-

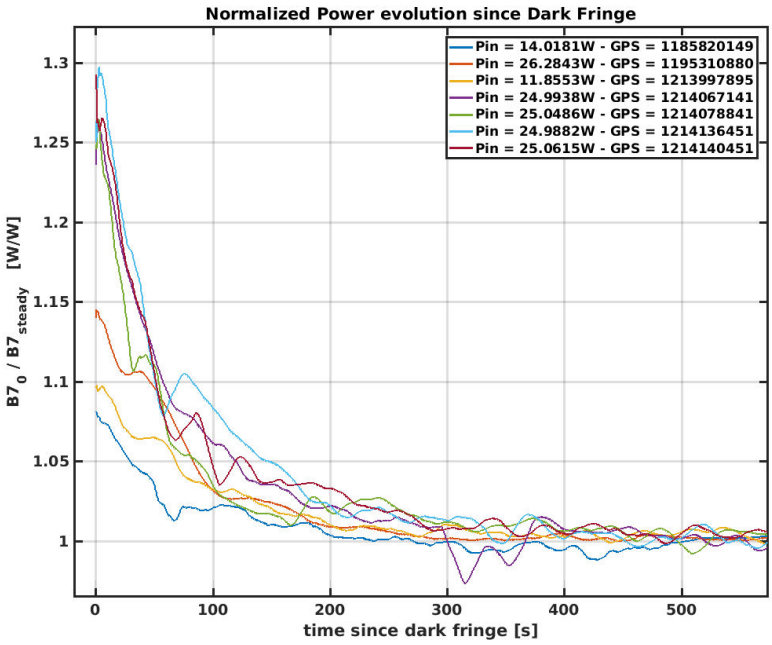

Figure 22: Evolution of the power transmitted by the North arm right after the lock of the full interferometer at time t = 0. The curves are for different input powers and the data are normalised with the steady state arm power (t > 300 second). The plot is taken from the Virgo logbook and made by Annalisa Allocca [65].

imised, the measured RTL during the cavity steady state (so after the transient) is increased as the laser power is increased. A model with one absorbing point on the mirror surface could explain such a trend as shown with the blue dashed curve in figure 23. The size, position and absorption for this absorbing point are roughly tuned by hand to match the measured trend and should be taken as an illustration for a possible explanation rather than the absolute truth.

Several strategies have been tested to mitigate the dependency of the cavity optical loss with the circulating power. First, slightly changing the alignment of the cavity to move the position of the laser beam on the mirror. An offset of 2 cm from the center could be achieved on the end mirror recovering most of the power drop and improving the contrast defect [66]. Unfortunately, the sensitivity for this working point is not practical due to the large coupling between alignment and displacement.

Second, it is also possible to change the RoC of the EM using the heating ring around the mirror. As shown in 2.5.2.1, the RoC could be decreased by 20 m from the initial RoC of 1696 m. The idea is to move away from the resonance of one higher order mode (mode of order 8) whose presence is visible at the dark port. That helped to reduce the power drop from 30% to 10% after the lock which is a very positive

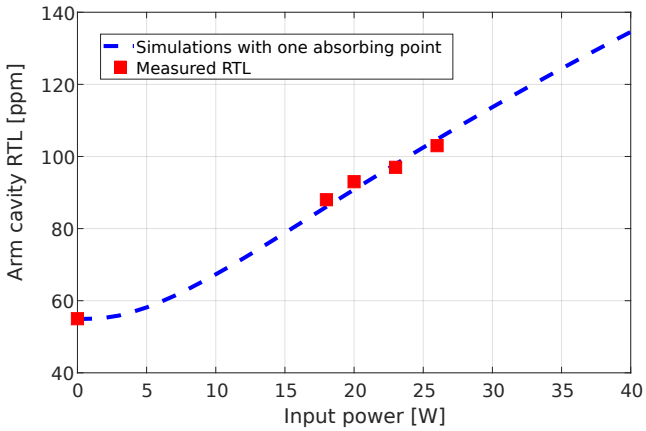

Figure 23: Comparison between the measured RTL and one simulation assuming a point absorber on one mirror. Additional graphs and explanation can be found in [68].

result and the heating ring was permanently on during the science run O3.

2.6 DESIGN OF ADVANCED VIRGO+ PHASE II ARM CAVITIES

While the AdV arm cavities were commissioned and studied, a parallel activity started in 2017 to define the next major upgrade of Virgo. The goal as usual is to further increase the sensitivity of the Advanced Virgo detector. In that framework, the upgrade program called Advanced Virgo plus (AdV+) was decided. It has been divided in two sequential parts:

PHASE I includes higher input laser power (up to 40 W), the signal recycling mirror, Newtonian noise cancellation and up to 4.5 dB of frequency dependent squeezing. The installation and commissioning take place between the science run O3 and O4 (spring 2020 to summer 2022).

PHASE II will have a further increase of laser power with potentially better squeezed light. The most crucial part will be new arm cavity mirrors with hopefully coating with lower thermal noise and larger end mirrors. The end mirrors will have a larger diameter (+60%) to increase the laser beam radius there and further reduce the level of the coating thermal noise, the main limitation of the sensitivity in the mid-frequency range. The installation and commissioning will take place between the science run O4 and O5 (mid 2023 to 2025).

The goal of this ungrade plan is more than triple the range of the detector, scanning a volume of space 30 times larger. The parameters of the new arm cavity of the phase II are presented in the table 8.

Table 8: Comparison of the arm cavity parameters between Advanced Virgo and Advanced Virgo + phase II. The cavity length remains 3 km.

MIRROR	SUBSTRATE DIAMETER [mm]	ROC [m]	LASER BEAM RADIUS [mm]
Advanced Virgo			
IM	350	1420	49
EM	350	1683	58
Advanced Virgo+ phase II			
IM	350	1067	49
EM	550	1969	91

The beam on the end mirror is enlarged on the new cavity to benefit from the larger diameter mirrors there. However, it was decided to keep the same beam size on the input mirrors, in that way, the size of the mirrors in the recycling cavities is unchanged. The flat optics (the beamsplitter, compensation plates and pick off plate) will be kept whereas the curved optics (power and signal recycling mirrors) will be exchanged since they will require new radii of curvature.

The g-factor of the new arm cavity is 0.95 versus 0.87 for the current one. It is a direct consequence of enlarging the beam radius on the end mirror as we are moving closer to the instability (g-factor of 1). The mode spacing between optical modes is also changed with $\Delta Pos_1 = 0.073[1/FSR]$ against $\Delta Pos_1 = 0.117[1/FSR]$ for the initial AdV arm cavity.

As the first starting point, it was decided to keep the same finesse for the new arm cavity as well as the same specification for the maximum allowable round trip loss (75 ppm). To be noted that depending on the astrophysical target, black holes or lighter neutron stars, the arm cavity finesse could be fine tuned to maximise the detector range [69].

So as previously, we calculated the arm cavity round trip loss as a function of the surface flatness of the mirrors. At that time we also scanned the radius of curvature of one mirror, for example, the end one as shown in figure 24.

Several comments can be made about figure 24:

- Without any mirror imperfection (black curve), the RTL rises quickly for RoCs below 1960 m. It is a direct consequence of moving closer to the cavity instability with the beam radius increasing quickly for a small change of RoC. The cavity is

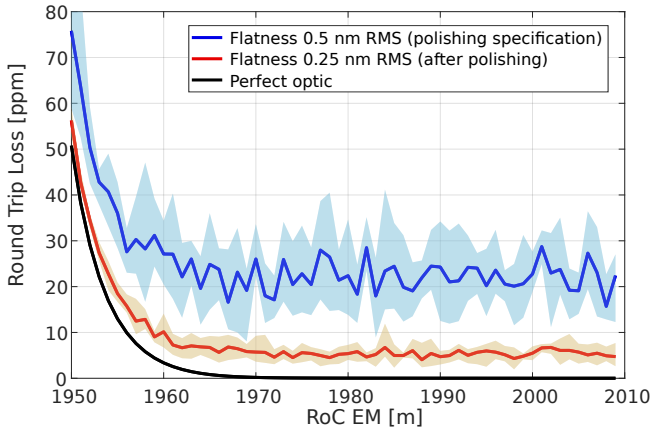

Figure 24: Round trip loss as a function of the RoC end mirrors for different polishing quality: perfect mirror, achieved polishing (flatness of 0.25 nm RMS) and polishing specifications (flatness of 0.5 nm RMS).

marginally stable (g-factor of 1) for a RoC of the EM of 1933 m, assuming the IM RoC of 1067 m.

- 2 RTL curves are plotted with 2 different RMS. In the simulations, surface maps of equal flatness are added on both mirrors of the cavity. The surface height distribution (PSD) follows the same as the current mirrors assuming we will use the same polishing techniques.
- Each of the 2 RTL curves is a result of 5 simulations with random surface maps (but with a given RMS and PSD). The average RTL of the 5 simulations is the dark curve, whereas the envelop as minimum and maximum is shown by the light area.
- The 2 RMS plotted are based on the experience of Advanced Virgo. 0.5 nm RMS was what was ordered to the polisher whereas 0.25 nm RMS was the surface quality after polishing so better what was ordered.
- The ordered EM RoC will be 1969 m. So we are 10 m away for the start of the rise of the RTL during the cavity instability region. That may seem small however from past experience, the RoC of all the mirrors were within 2 m of the target after polishing.

As a result, the same flatness specification will be used for the initial Advanced Virgo. On the central part, a flatness below 0.5 nm RMS would be sufficient to achieve a RTL due to low spatial frequency below 50 ppm. One difference however exists in the diameter of what we call the central part to define the specifications. Since the beam size on the end mirror is larger, the diameter of the central part with

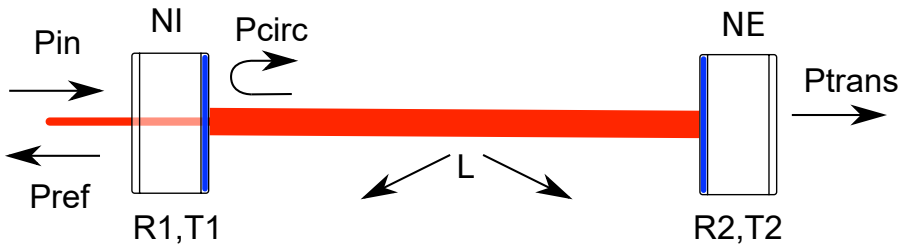

Figure 25: Notation used for the calculations in this section.

the most stringent specifications is 235 mm versus 150 mm for the input mirror.

For Advanced Virgo+ phase II the new substrates were delivered to LMA at the beginning of 2021. At the time of writing, the call for tender for the polishing has been launched for the polishing to start after summer 2021.

2.7 QUICK FORMULAS

Here is a summary of some useful simplified formulas to give the right order of magnitude to the relevant parameters. We will extensively use, one property of the Virgo arm cavities: the end mirror is almost perfectly transmissive with a transmission that must be less than the input mirror. More precisely, the transmission of the IM, T_1 is 1.4 %, while the transmission of the end mirror T_2 is 5 ppm.

Similarly we define the power reflectivity of the IM and EM as respectively $R_1 = 1 - T_1$ and $R_2 = 1 - T_2$. The round trip loss in the cavity, excluding the mirror transmissions is noted L.

The power incident on the cavity is noted P_{in}, P_{circ} is the circulating power whereas P_{ref} and P_{trans} are respectively the reflected and transmitted powers. All these notations are summarized in figure 25.

2.7.1 *Finesse*

The most general formula for the cavity finesse $\mathcal{F}$ can be written as (formula 50 in the article [70]):

$$\mathcal{F} = \frac{\pi}{2}\left[\arcsin\left(\frac{1-\sqrt{R_1 R_2}}{2\sqrt[4]{R_1 R_2}}\right)\right]^{-1} \tag{9}$$

Using $\arcsin x \approx x$ for small x, the previous equation can be simplified to:

$$\mathcal{F} \approx \pi \frac{\sqrt[4]{R_1 R_2}}{1-\sqrt{R_1 R_2}} \tag{10}$$

$$\approx \pi \frac{\sqrt[4]{(1-T_1)(1-T_2)}}{1-\sqrt{(1-T_1)(1-T_2)}} \tag{11}$$

$$\approx \pi \frac{\sqrt[4]{(1-T_1-T_2+T_1T_2)}}{1-\sqrt{(1-T_1-T_2+T_1T_2)}} \tag{12}$$

$$\approx \pi \frac{(1-\frac{T_1}{4}-\frac{T_2}{4})}{1-1+\frac{T_1}{2}+\frac{T_2}{2}} \tag{13}$$

In our case, we have $T_1 \gg T_2$, with T_2 including also the small loss L, we arrive to the formula:

$$\mathcal{F} \approx \pi \left(1-\frac{T_1}{4}\right) / \left(\frac{T_1}{2}\right) \tag{14}$$

$$\approx 2\pi \left(\frac{1}{T_1}-\frac{1}{4}\right) \tag{15}$$

Finally since $2/T_1$ is superior to 140, it could be further simplified to:

$$\boxed{\mathcal{F} \approx \frac{2\pi}{T_1}} \tag{16}$$

To give you an idea of the error made by all the approximations, the original formula eq. (9) gives a finesse of 443, while the last one eq. (38) is equal to 449, so the error is less than 2%.

2.7.2 *Cavity power gain*

On resonance, the circulating power in the cavity can be written as [60]:

$$P_{circ} = \frac{T_1}{\left(1-\sqrt{1-T_1}\sqrt{1-T_2}\sqrt{1-L}\right)^2} P_{in} \tag{17}$$

As T_1, T_2 and L are small compared to 1, we can simply the previous equation as:

$$P_{circ} \approx \frac{T_1}{\left(1-(1-\frac{1}{2}T_1)(1-\frac{1}{2}T_2)(1-\frac{1}{2}L)\right)^2} P_{in} \tag{18}$$

$$\approx \frac{T_1}{\left(1-(1-\frac{1}{2}(T_1+T_2+L))\right)^2} P_{in} \tag{19}$$

As the transmission of the input mirror is much higher than the transmission of the end mirror and the losses, the equation can be further simplified as:

$$P_{circ} \approx \frac{T_1}{\left(\frac{1}{2}T_1\right)^2} P_{in} \tag{20}$$

$$P_{circ} \approx \frac{4}{T_1} P_{in} \tag{21}$$

For comparison, the first equation (17) is giving a power gain of 281, whereas the simplified eq. 21, so neglecting the loss gives 287. The gain of the cavity including the finesse is:

$$\boxed{P_{circ} \approx \frac{2}{\pi}\mathcal{F} \quad P_{in}} \tag{22}$$

From the circulating power, it is very easy to derive the transmitted power P_{trans} simply as:

$$P_{trans} = P_{circ} T_2 \tag{23}$$

$$\tag{24}$$

2.7.3 *Reflected power*

The reflected power P_{ref} from the cavity on resonance is equal to [60]:

$$P_{ref} = \left| \frac{\sqrt{1-T_1} - \sqrt{1-T_2}\sqrt{1-L}}{1-\sqrt{1-T_1}\sqrt{1-T_2}\sqrt{1-L}} \right|^2 P_{in} \tag{25}$$

Assuming as usual that T_1, T_2 and L are much smaller than one and eliminating the smaller terms, the previous equation can be simplified as

$$P_{ref} \approx \left| \frac{1-\frac{1}{2}T_1 - (1-\frac{1}{2}T_2 - \frac{1}{2}L)}{\frac{1}{2}(T_1+T_2+L)} \right|^2 P_{in} \tag{26}$$

$T_2 + L$ is nothing less than the round trip loss RTL used since the start of this chapter. So the equation can be simply written as:

$$P_{ref} \approx \left| \frac{RTL - T_1}{RTL + T_1} \right|^2 P_{in} \tag{27}$$

$$\approx \left| \left(\frac{RTL}{T_1} - 1 \right) \left(1 - \frac{RTL}{T_1} \right) \right|^2 P_{in} \tag{28}$$

$$\approx \left| 1 - 2\frac{RTL}{T_1} \right|^2 P_{in} \tag{29}$$

$$\approx \left(1 - 4\frac{RTL}{T_1} \right) P_{in} \tag{30}$$

Recalling equation 21, the equation 30 can be written as:

$$\boxed{P_{ref} \approx (1 - Gain \times RTL)\, P_{in}} \tag{31}$$

So we found the formula described in figure 18 with $Gain$ the power gain of the cavity. For completeness and to take into account more terms in T_1 and RTL in the Taylor expansion of P_{ref}, the initial equation 25 of P_{ref} could be written as:

$$P_{ref} \approx \left(\frac{T_1 - 2RTL + \frac{T_1^3}{8}}{T_1 + 2RTL + \frac{T_1^3}{8}} \right) P_{in} \tag{32}$$

The development is rather long and tedious and so it is not detailed here. The simplified equation 31 gave an error of 4% whereas for the last equation 32, the error would be less than 0.1%.

2.7.4 *Round Trip Loss*

The measurement of the arm cavity Round Trip Loss (RTL) is based on equation 30. When the cavity is unlocked, the reflected power $P_{ref}^{unlocked}$ is equal to P_{in}, so the equation becomes:

$$P_{ref}^{locked} = \left(1 - 4\frac{RTL}{T_1} \right) P_{ref}^{unlocked} \tag{33}$$

Which gives the simple equation for the RTL:

$$\boxed{RTL = \frac{T_1}{4} \left(1 - \frac{P_{ref}^{locked}}{P_{ref}^{unlocked}} \right)} \tag{34}$$

3

THE BMV CAVITY

For the second main part of this document, the focus will be another optical cavity but this time inside the cleanroom at LMA. The goal of this cavity is to characterise the round trip loss of very high reflectivity mirrors. It was initiated thanks to a long standing collaboration with the Laboratoire National des Champs Magnétiques Intenses of Toulouse (LNCMI-T [71]) where a similar cavity is used to measure the magnetic birefringence of vacuum.

After experiencing Virgo, it is refreshing to work with a stand-alone cavity in the lab, right next to my office. The experiment is flexible and can be mastered up to the smallest details since much simpler. Moreover, it does not come with the (unavoidable) numerous meetings from a large collaboration. In short, you could say that it is my own little secret garden.

3.1 INTRODUCTION

BMV (standing for Biréfringence Magnétique du Vide) is the name of the experiment at the LNCMI Toulouse which started in the years 2000. It aims to experimentally demonstrate a prediction from the quantum electrodynamic theory: a linearly polarised electric field will become elliptic while passing through a magnetic field. This effect is extremely small and represents an experimental challenge [72].

Conceptually, the experiment could be rather simple, a perfectly linear polarised laser beam passes through a magnetic field and then its polarisation is analysed with a polarising beamsplitter. It can be shown [73] that the ellipticity of the transmitted field is directly proportional to the square of the magnetic field and to the interaction length between the magnetic field and the light.

The magnetic field can either be modulated (like for PVLAS [33] with a magnetic field of 2.5 T) or pulsed (BMV approach with a 6 T magnetic field [73]). To further increase the interaction between the light and the magnetic field, the magnet is inserted within a high finesse resonant Fabry-Perot cavity. The typical finesse of the cavity is around half a million for a length of few meters.

This chapter focuses on the replication of such cavity at LMA with the support of the BMV Toulouse team. The aim of the cavity at LMA is to measure the round trip loss of the mirrors using the ringdown method: once the cavity is locked, the input light is suddenly blocked and the exponentially decreasing cavity transmitted power is then

recorded. The higher the half life time of the photons, the higher the cavity finesse.

3.2 THE INITIAL BMV CAVITY AT LMA

A BMV style cavity at LMA was initiated through a successful ANR proposition submitted in 2014, which practically started in 2015. Part of the project was to replicate the cavity housed at the LNCMI (but without the magnetic field) and installed it in the cleanroom at LMA. In that way, the very high reflectivity mirrors coated at LMA could be characterised in a similar cavity as in Toulouse. Only the best mirrors could then be sent and any degradation due to contamination could be highlighted.

Since BMV Toulouse was upgrading its vacuum infrastructure for bigger tanks, their previous vacuum chambers were transferred and installed at LMA during autumn 2015. For illustration, two photos of the installation are shown in figure 26. For the LMA experiment, the vacuum level requirement is less stringent than the one in Toulouse. For us, a primary vacuum (0.1 mbar) is enough whereas in Toulouse reaching a high vacuum of 1×10^{-7} mbar is mandatory to not be limited by the Faraday effect[1] from the residual gas.

The whole setup must fit on a 3 m $\times$ 1.5 m optical table mounted on isolated feet. At first, we only have a laser directly injected into the cavity with an approximate mode matching. The following year was dedicated to complete the optical setup to reach the layout shown in figure 27.

3.2.1 *Details of key components*

In this section, we will mention briefly the key parts of the optical setup. The main goal is to be able to lock the laser frequency to the cavity (uncontrolled) resonance length and hence to maximise the transmitted power. This is achieved using well-known techniques that are described in the literature. A photo of the whole experiment (excluding the electronic rack) is shown in figure 28. The experiment is installed in the same clean room as where the mirrors are coated, hence reducing the risk of dust contamination.

3.2.1.1 *The laser*

The source of light for this experiment is a laser Mephisto 500 NE from the company Coherent. At the heart of the laser, there is a monolithic Nd:YAG crystal for the amplification medium within a non-planar ring oscillator (NPRO) to create the cavity. It is actually

1 Rotation of the polarisation of the electric field in media due to the presence of a magnetic field.

Figure 26: Installation of the BMV vacuum chambers in the clean room at LMA. This work was performed by Mathilde Fouché and Rémy Battesti.

the same kind of laser as the master laser of Virgo. The wavelength is 1064 nm and the maximum output power is 500 mW. It has excellent stability both in power and frequency. During our measurement, the pump current is set to 1.2 A to deliver 360 mW of light.

As the output of the laser, the polarisation is partially elliptic, a quarter and half waveplates are installed before the first Faraday isolator to maximise the light throughput.

3.2.1.2 *The AOM path*

The acousto-optic modulator (AOM) is mounted in double pass configuration and will serve two purposes:

1. a fast actuation on the laser frequency to keep the cavity locked. To stay far away from the resonance frequencies of the PZT in the laser head, all the frequency feedback above few kHz will be achieved by the AOM only.

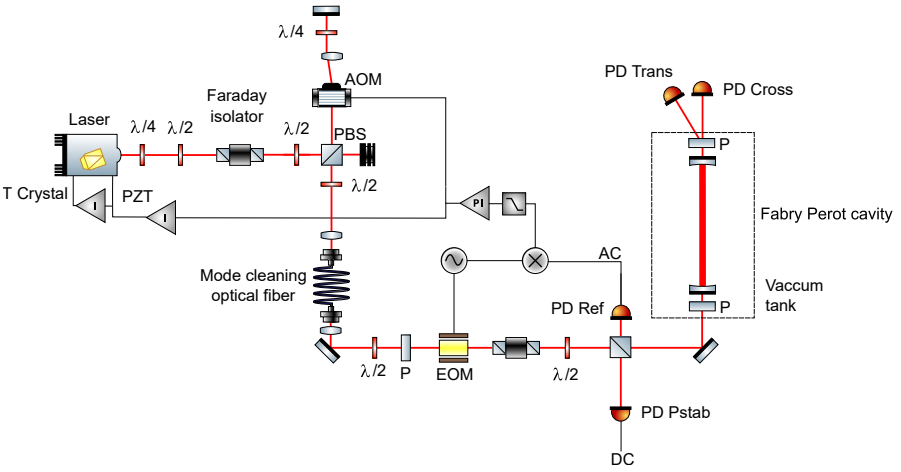

Figure 27: Schematic of the optical setup of BMV at LMA. As the first incarnation, it has been copied from the one in Toulouse.

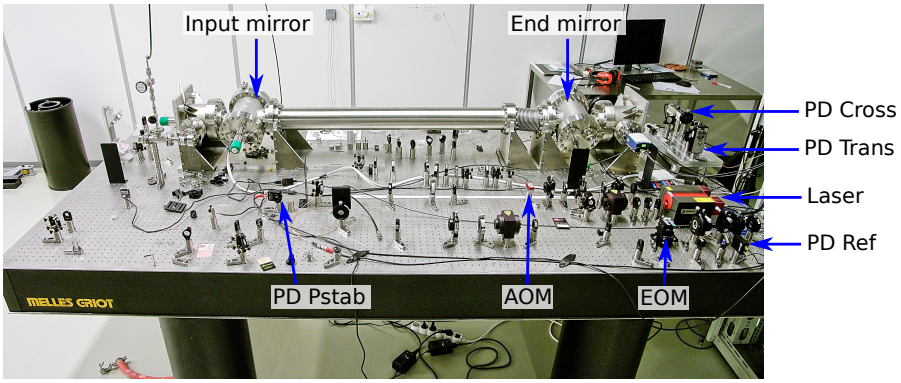

Figure 28: Photo of the experiment as at the end of 2018. The physical positions of the photodiodes and some components described in the text are shown.

2. the possibility to actuate on the laser amplitude to stabilize the laser power in entrance of the cavity. Moreover by switching off the modulation of the AOM it is possible to extinct the laser within few microseconds much faster than the decay time of the high finesse cavity.

The AOM used is the model MT80-B30A1 made with a tellurium dioxide (TEO_2) crystal from Opto-Electronic, its optical transmission is 99% and its aperture is 1.5 mm. To drive the AOM a Voltage Controlled Oscillator (VCO) has been implemented, it is a custom version of the model RFA10Y-B-0-60.150 from the same manufacturer. To be fully compatible with the locking electronics, the frequency tuning gain has been decreased and the input is now symmetric between –5 V and 5 V instead of the initial 0 V to 10 V.

3.2.1.3 *The optical fiber*

After the double pass through the AOM, the laser beam is injected to a polarization-maintaining monomode optical fiber (5 m long, reference P1-1064PM-FC-5 from Thorlabs). The fiber delivers a well defined TEM_{00} with a stable alignment. The fiber reduces the laser beam jitter at the price of increasing the intensity noise. As such, it is not an issue as we will see later the power of the laser is actively stabilised before entering the cavity.

The transmission of the fiber has been measured to be around 70% with the optimal alignment giving an output power of around 50 mW. The current fiber has non tilted fiber ends (PC) and so we can notice an etalon effect in the fiber as the fiber itself behaves as a very low finesse cavity. It is particularly obvious when the laser frequency is scanned with a triangle waveform, the intensity at the output of the fiber is then modulated too. Fiber with APC connectors would have been a better choice however the intensity modulation due to the fiber in our case has little incidence since the power entering the cavity is actively stabilised (more later on that).

3.2.1.4 *The EOM and the PDH error signal generation*

To be able to keep the cavity on resonance, maximising the circulating power, one has to actively tune the laser frequency to match the cavity length. For this setup, we use the Pound Drever Hall (PDH) technique [74] to lock the laser to the cavity. The PDH scheme allows deriving an error signal proportional to the frequency mismatch between the cavity resonance and the laser. The error signal is then fed back to the AOM (fast actuation, small range), laser PZT and also to the laser crystal temperature to remove any long term drift.

An example of a real PDH signal is shown in figure 29 for a low finesse cavity. We can notice that the error signal change sign at the resonance and is proportional to the frequency detuning between the cavity resonance and the laser. Those are the good properties we need however it has one drawback: the error signal is only present near the resonance. So we will have to scan the laser frequency and only engage the control loop when we are near the resonance, the trigger is done when reaching a certain cavity transmitted power.

To derive the PDH signal, one needs a Electro-Optic Modulator (EOM) to apply a sinusoidal phase shift to the laser field. This creates a pair of sidebands around the carrier field which are not resonating in the cavity and could be seen as phase reference which will be compared to the phase of the carrier reflected field near the resonance.

The EOM and the modulation-demodulation electronics are made by the company Qubig [75]. The EOM is a lithium niobate ($LiNbO_3$) crystal with a 3 mm aperture, the modulation frequency is fixed at 9.959 MHz due to the nature of the EOM resonant LC circuit.

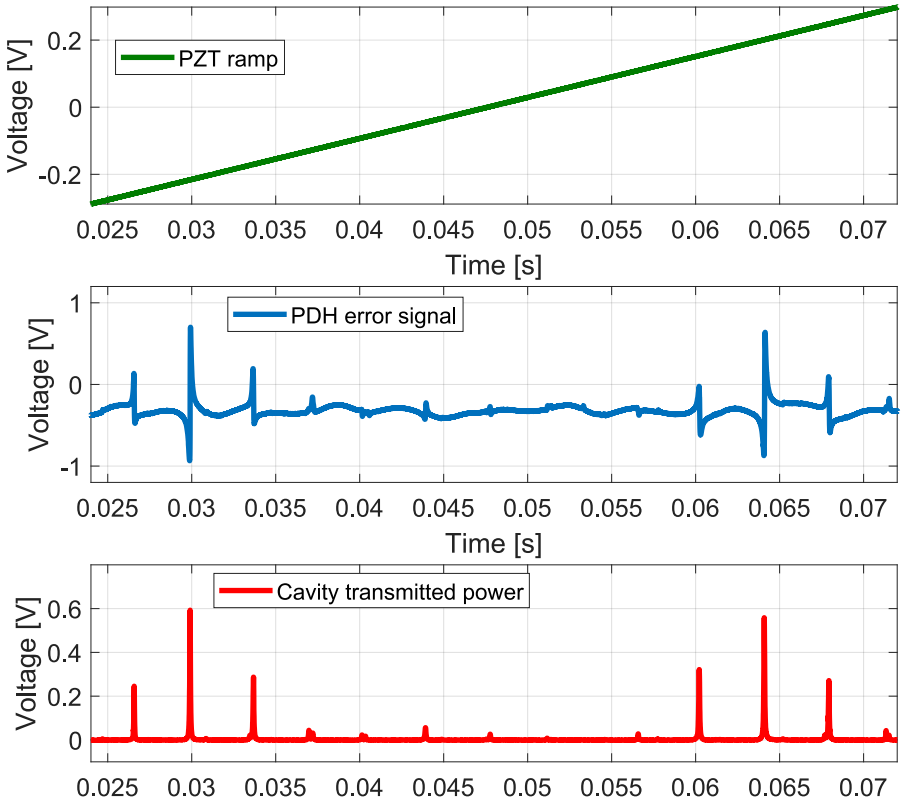

Figure 29: Example of a FSR scan of the cavity with the associated PDH signal. The laser frequency is scanned thanks to a ramp applied to the PZT of the laser head (top plot). For this figure, we used a cavity with low finesse 780.

3.2.1.5 *The photodiodes*

Four photodiodes are used to monitor and control the cavity. One photodiode (PD Pstab) is sampling part of the beam entering the cavity and is used for the stabilisation of the laser intensity. One photodiode (PD Ref) is looking at the reflected beam from the cavity and once demodulated is used to derive the PDH error signal. Finally, in transmission of the cavity two photodiodes are present: one to monitor the transmitted power in the incident polarisation (PD Trans) and one to look at the power in the cross (perpendicular) polarisation (PD Cross).

A summary of the characteristics of the different photodiodes is presented below:

PD Pstab is a versatile large diameter Si photodiode (Throlabs PDA36A) with adjustable gain. The incident power is few mW on it and since we use it with low gain the bandwidth is rather larger (MHz), much more for what is necessary to stabilise the laser intensity where the actuation is below 100 kHz.

PD REF is a small (0.5 mm diameter) InGaAs photodiode (Qubig PD-AC200-IR). The photodiode was provided with the Qubig controller with fixed very high gain (16 kV/A) while keeping a high bandwidth up to 200 MHz. Due to the high gain, we attenuate the power before reaching the photodiode to have around 30 µW of incident light.

PD TRANS is a multi-purpose Newfocus 2011 InGaAs 0.2 mm diameter photodiode with adjustable gain. When the very high finesse is locked, several mW of light can reach this detector.

PD CROSS monitor the amount of light in the polarisation perpendicular to the incident light. In a perfect case, no light is expected at this output. However, due to imperfections in the polarisers, birefringence or even scattered light 10 nW to 100 nW could still be present. There, a photodiode FEMTO 02-200-IN1 has been installed. It is a high speed high gain photoreciever with 0.3 mm InGaAs photodiode. This photodiode has 2 purposes: to measure the birefringence and also to trigger the longitudinal lock of the cavity when we are close to resonance.

3.2.1.6 *The cavity mirrors*

The most critical optics are the two cavity mirrors. They are 25.4 mm in diameter for a thickness of 6.35 mm and a photo of one of them has already been shown in figure 5. The substrate is super-polished with a flatness of $\lambda/20$ (P-V measured at λ 633 nm) and a specified RoC of 8 m. The coating is made by IBS in the same machine as the Advanced Virgo mirrors to guarantee the lowest possible absorption.

The mirrors in its aluminium mount inside the vacuum chamber is presented in the photo in figure 30. The mirror is itself installed on a Newport Agilis mount where the tilt and rotation (also called pitch and yaw) could be remotely adjusted with PZT actuators. This is crucial to properly align the cavity to the incoming laser beam and to thus maximise the circulating power. The whole mirror mount can also rotate on itself to measure the mirror birefringence or to align the two mirrors along the same axis. That is achieved by turning the gearwheel which is shown on its side in figure 30.

The circular mount where the mirror is inserted has been specially designed to limit the stress on the substrate to not induce additional birefringence to the mirrors. During the installation, special care is taken to tighten at minima the mirrors to their mounts.

3.2.1.7 *The two polarisers before and after the cavity*

Located at the closest of the cavity mirrors but outside of the cavity, very selective polarisers are installed inside the vacuum chambers. Both polarisers are identical and are from the Glan-Taylor kind with

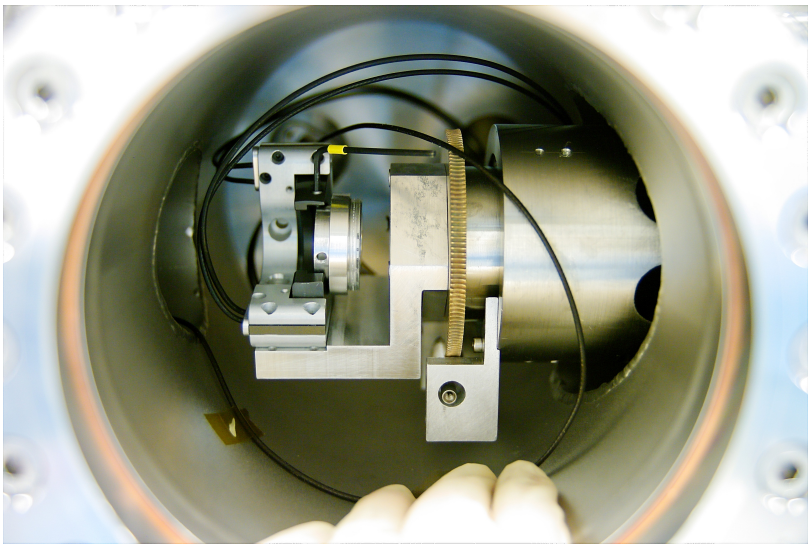

Figure 30: Inside the vacuum chamber, the mirror in its mount is at the center of the image. The installation of the mirror is not particularly difficult but requires some practice due to the limited amount of space available.

one escape window to reflect the unwanted polarisation. They are made by the Karl Lambrecht company and have a clear aperture of 10 mm (model MGLS-SW-10 [76]) with AR coating at 1064 nm. The extinction ratio is specified to be less than 2×10^{-5}.

The polariser right before the input mirror is used in transmission and guarantees that the laser beam enters the cavity with a very pure polarisation. A second identical polariser is inserted after the cavity end mirror and is turned by 90° compared to the first polariser (cross polarisation configuration). The very faint transmitted beam which quantifies the change of light polarisation in the cavity is sent to the photodiode PD Cross, whereas the reflected beam containing the cavity transmitted light is extracted from the vacuum chamber by a steering mirror and is sent to the photodiode PD Trans.

3.2.2 *The control system*

We have two separate and independent control loops in the setup: one longitudinal loop to keep the cavity on resonance and one to stabilise the laser intensity.

3.2.2.1 *Longitudinal lock of the cavity*

To achieve (and maintain) the lock of the cavity, two components are required. The first one is to derive a PDH error signal, a signed[2] signal proportional to the frequency mismatch between the laser and the

2 positive or negative

cavity resonance. Once we have such error signal, the second component is the feedback electronics to close the loop and to actuate properly on the laser frequency.

The generation of the PDH error signal is provided by a system from the company Qubig which includes: a signal generator to create the 9.959 MHz sidebands with the EOM, the photodiode PD Ref in reflection of the cavity as well as the demodulation (and low pass filtering) electronics. After optimising the demodulation phase by turning a knob to maximise the error slope around the resonance, the typical error signal looks like the one shown in figure 29 for a low finesse cavity.

The first attempt to lock the low finesse cavity was achieved with a FPGA board Red Pitaya [77] with the toolbox PyRPL developed at the LKB [78]. It works fine with only an actuation on the laser PZT but that was impractical for the very high finesse cavity. For this latter case, much more demanding, all the feedback electronics was bought from the company Sisyph [79].

The technical solution proposed by Sisyph was already tested at BMV Toulouse and we can confirm the excellence of the various modules. The PHD error signal from the Qubig controller is first amplified by a factor 10 and an adjustable DC offset is manually added to guarantee the PDH signal zero crossing at the maximum of the circulating power. The error signal is then sent internally to the high speed module, a PID feedback system whose output is sent to the AOM for the fast frequency correction. Two extra integrators are added to boost the low frequency correction.

To avoid that the AOM correction channel saturates, the low frequency part of the feedback signal is sent to the laser PZT inside the laser head. That is another module internally linked with an independent PID system. Finally, the slow (< 1 Hz) but large amplitude frequency drift is corrected by actuating on the temperature of the laser crystal with thermo-electric cooler (TEC) also in the laser head.

For the lock acquisition, a ramp is sent to the laser TEC to linearly scan the laser frequency. The control loops are only closed once we are near the resonance inside the cavity. In practice, the control is engaged only when the output of the fast, very high gain, PD Cross reaches a certain threshold, indicating that the light starts to resonate inside the cavity.

Time series of the relevant signals during lock of the cavity are shown in figure 31. First, the cavity is unlocked and so the transmitted power is zero as shown in the top trace. Then the locking procedure is engaged as seen by the ramp in the laser TEC (bottom plot). There is a short first lock lasting only 5 s interrupted by the saturation of the PZT feedback channel at < 10 V. The cavity is then relocked within 2 s and this time the lock lasts for more than one minute, a lapse of time largely sufficient to do a ring-down measurement.

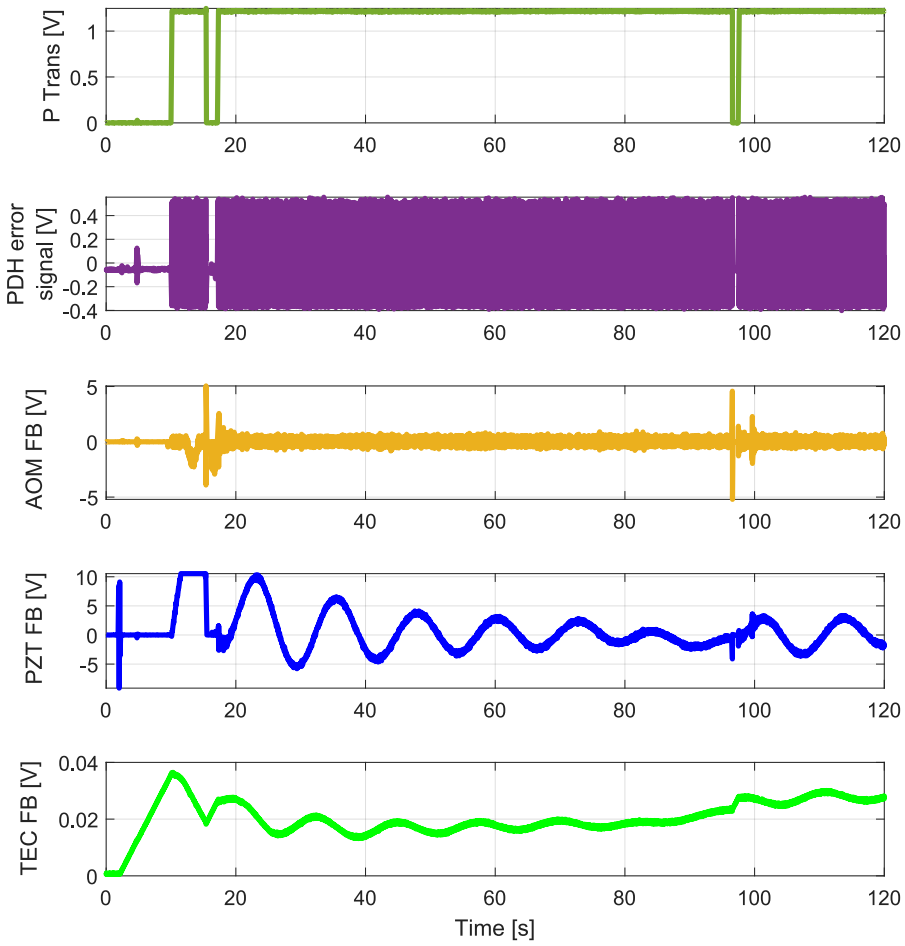

Figure 31: Evolution of the control signals during two minutes of a lock acquisition for the high finesse cavity. Traces from top to bottom: transmitted power, PDH error signal, feedback to the AOM, feedback to the laser PZT and at bottom feedback to the laser TEC.

Unfortunately due to my limited time availability, it was not possible to characterize the feedback loops in the frequency domain.

3.2.2.2 *Power stabilisation*

The output of the laser is very stable but after the mode cleaning fiber, any beam jitter or misalignment is converted to power fluctuations. So to stabilise the cavity input power, around 4% of the power of the beam entering the cavity is extracted and sent to the monitoring photodiode PD Pstab. The signal from this photodiode is compared to a target value and after a controller, the power is stabilised by acting on the amplitude modulation at the level of the AOM, using the Mod In input of the Voltage Control Oscillator (VCO) driving the AOM.

The controller in that case was the Red Pitaya board since we no longer used it for the lock of the high finesse cavity. A simple Proportional Integrator (PI) feedback was enough to stabilise the laser as illustrated in figure 32.

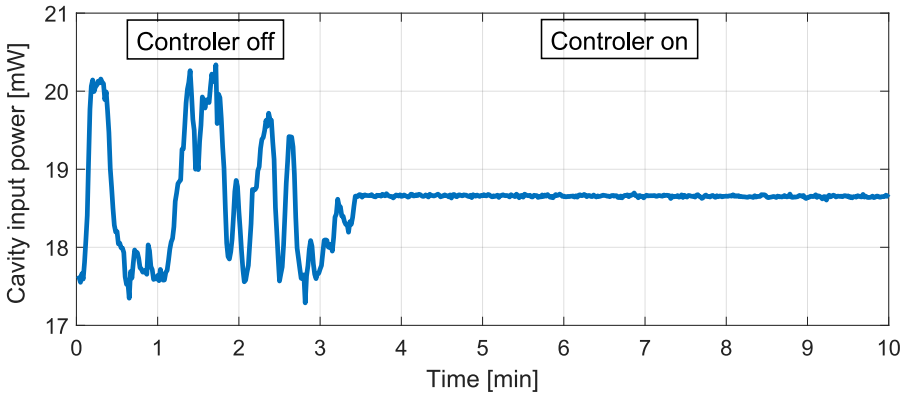

Figure 32: Effect of the power stabilisation loop on the input power of the cavity. The data were taken with a power meter interfaced directly to the computer with a sampling frequency of 1 Hz.

3.2.3 *Optical characterisation*

The characterisation of the cavity was done with two sets of mirrors. To maximise the transmission, for each set the input and end mirrors are identical, polished with the same specifications (so same RoC) and also coated at the same time (so same transmission). The first set is a low finesse mirror with a transmission at 1064 nm of 0.44% (expected finesse around 700) and the second one with mirrors of transmission 2 ppm and average scattering of around 7 ppm (expected finesse around 350 000).

3.2.3.1 *Low finesse characterisation*

The characterisation of the low finesse cavity is rather straightforward but still insightful. We even do not have to lock the cavity to retrieve the most relevant parameters, everything could be achieved by scanning the laser frequency over several FSR. An example of such FSR has already been presented in figure 29 and another one with useful annotations is shown in 33.

The analysis described below is not done on a single FSR, but during the same scan more than 500 FSR are acquired sequentially at the speed of around 20 FSR per second. So the analysis is done automatically on all the FSR, given some statistics on the parameters measured. The error bars are mentioned to give the fitted parameter with a 95% confidence interval. This work was done by Philippe Birembaux during his M2 internship at LMA.

CAVITY LENGTH The cavity length measurement is based on the measurement of the FSR calibrated in frequency thanks to the well defined sidebands position. We know by construction that the sidebands are separated from the carrier by exactly 9.959 MHz. So from the FSR measurement, we calculate the frequency difference between

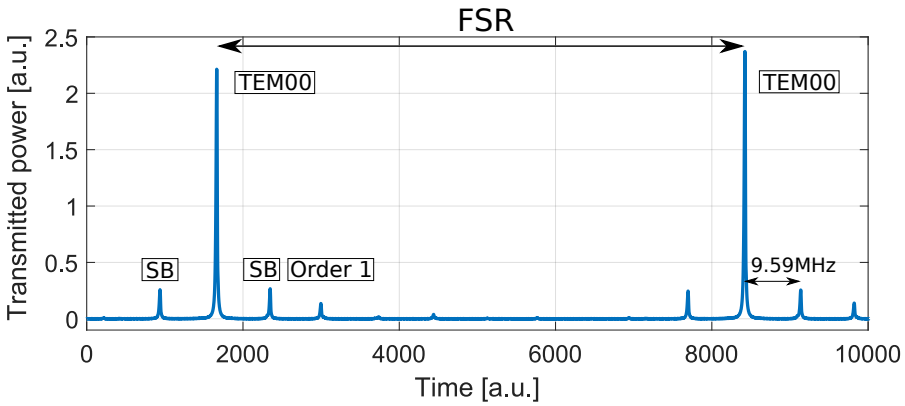

Figure 33: Zoom over one FSR for the low finesse cavity where the resonances of the sidebands (SB) and the first order higher mode are highlighted.

two consecutive resonances of the carrier. Then the cavity length L is simply given by $L = c/2FSR$ with c the speed of light. Using this approach, the cavity length was measurement to (158.4 ± 5.3) cm.

FINESSE The finesse is also measured by recording several FSR scan and then by fitting the transmission of the cavity using the theoretical Airy function. For this measurement, the sidebands are removed (modulation depth set to zero) to not degrade the fitting procedure. The finesse is found to be 780 ± 160.

MIRROR RADIUS OF CURVATURE The mirror RoC is determined in the same way as described previously for the optical characterisation of Advanced Virgo (see section 2.5.2.1). The relative position of the resonance of the first higher order optical mode with the respect to the resonance of the fundamental mode is measured. That is directly linked to the g-factor of the cavity and hence to the mirrors RoC. In the BMV case, we assume both input and end mirrors to have the same RoC since they are from the same polishing batch. The same Airy function used to fit the fundamental mode for the finesse is now also used to fit the smaller HG01 peak, returning the difference in position of the two normalised by the FSR. In this way, the measured RoC is found to be (7.7 ± 0.7) m to be compared to the RoC of 8 m ordered from the polishing company[3].

3.2.3.2 *The very high finesse characterisation*

For the very low transmission mirrors, we are only interested to measure the finesse as we can safely assume that the length of the cavity and the mirror RoC must be similar as in the low finesse case (remember that for both cases the polished substrates are identical). The

3 It is not possible to measure directly very low RoC at LMA with the Zygo interferometer since we do not have a matching reference sphere with such a high curvature.

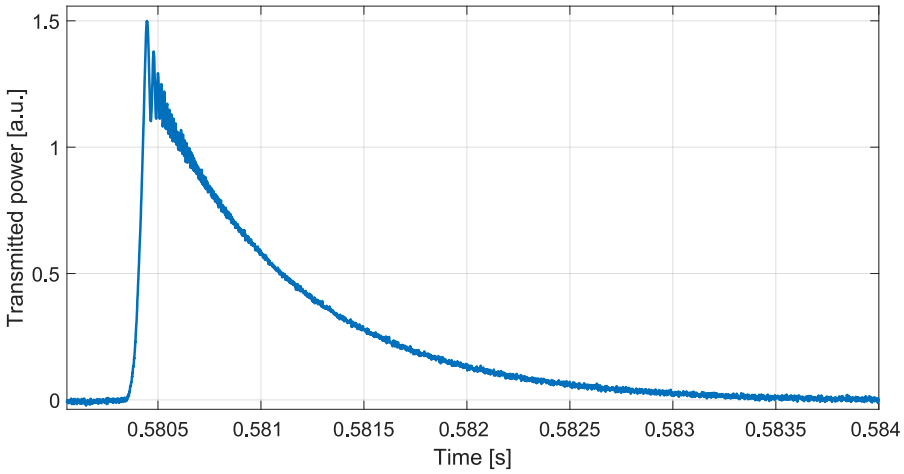

Figure 34: Passing through the resonance of the cavity with the very low transmission mirrors. The fitting of the decay time could already give a reasonable estimate of the cavity finesse.

finesse could still be estimated by scanning the cavity over several FSR, however in that case the transmission across the resonance is not a symmetric Airy peak but rather some dampened oscillations as shown in figure 34.

The round trip losses are extracted by calculating the finesse of the cavity derived from the measurement of the light life time in the cavity. For that the cavity is locked and then suddenly we switch off the laser power and record the decay time of the light in transmission. To extinct quickly the input laser light, a manual switch was built to switch off the input of the modulation command of the VCO driving the AOM. Using a fast response photodiode, we measured the extinction time of the laser to be in the order of 1 µs.

The measurement of the light decay time of the high finesse cavity is shown in figure 35 as measured by the photodiode in transmission PD Trans. The signal is acquired without difficulty and is repeatable, the fitting is also straightforward with a single decreasing exponential function whose time constant τ is extracted.

From the decay time τ of the light, the finesse $\mathcal{F}$ could be calculated using the formula [73]: $\mathcal{F} = \pi c\tau/L$ with L the cavity length and c the speed of light in vacuum. The length L is 1.58 m as measured with the low finesse mirrors and τ is given by the ringdown measurement 630 µs. That gives a cavity finesse of 376 000 and assuming the transmission of the mirrors to be 2 ppm, we can deduce the RTL to be of 13 ppm coherent with the scattering measurement of 7 ppm per mirror.

Due to other commitments, it was not possible to exhaustively characterise the cavity and the control system. Also for the same reason, no birefringence measurement of the mirror was made. However, while working on the cavity, I noticed several sources of improvement

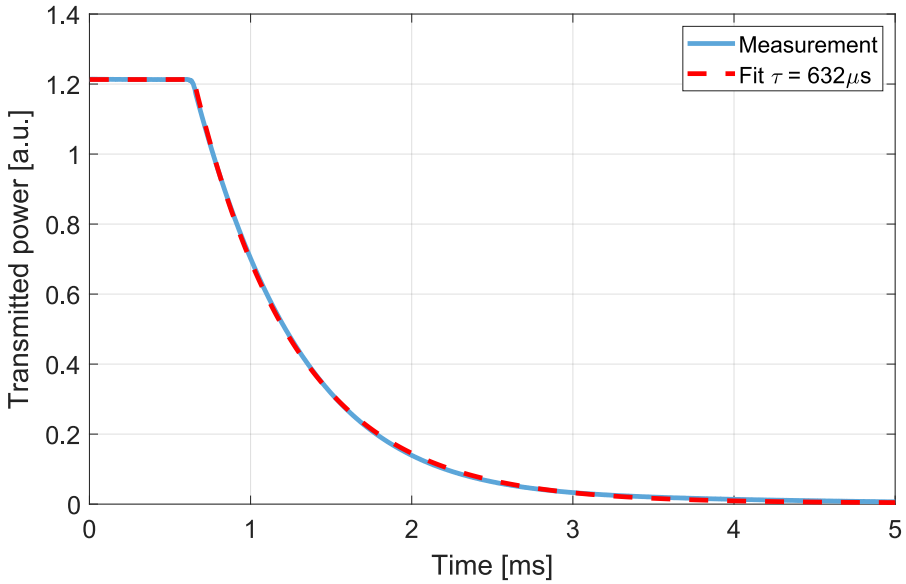

Figure 35: Measurement of the cavity decay time for the high finesse mirrors. The fit is a single decreasing exponential.

and came to mind to realise a new version of the experiment. That is the topic of the next section.

3.3 THE UPGRADED SETUP

While operating during several years the original BMV setup at LMA (even if not continuously), it was clear that several improvements could be made to make life more comfortable as well as improving the science reach. The most concern was coming from the in-vacuum part of the experiment, the installation of the mirror is tedious due to space constraints, the rotation of the mirror on itself to measure the birefringence is done manually with the risk of twisting the PZT wires attached to it. Finally, it was noted during the alignment of the cavity that the cavity losses depend on the position of the laser beam on the mirror surface.

So the ideas were present to have an upgraded version of the BMV experiment but unfortunately not the adequate funding. The opportunity came with the project OSAG[4], project funded by the (now deceased) IDEX of Lyon. In this project, we will demonstrate that mirrors with sapphire substrates could also be used in the most demanding optical experiments as they can provide extremely low optical losses. Sapphire has numerous advantages such as very high thermal conductivity, high density and operation at low temperature however it is difficult to polish and the birefringence and absorption could be an issue in high precision or high power experiments.

4 OSAG stands for Optiques en Saphir pour l'Astronomie Gravitationnelle, project in collaboration with institut Lumière Matière (iLM) also in Lyon campus.

I should mention that this work was done with Napoléon Gutierrez who had a 1 year research engineer contract to work on upgrading the setup.

3.3.1 *The new requirements*

The focus of the upgrade was the new mounting and positioning of the high finesse mirrors in vacuum. In particular, we wanted to:

- move transversally the mirrors to be able to perform 2D scans of the optical losses as a function of the position of the laser beam on the mirror
- move longitudinally the mirror to change the length of the cavity, so the degeneracy of the cavity for certain lengths (or g-factor) could be avoided
- be able to rotate the mirror on itself automatically.

As previously, the mirrors should also be adjusted in angle to align the cavity. Only including, the need to move the mirrors transversally, longitudinally and to rotate them, required at least a mount with 5 degrees of freedom. So to avoid the stacking of displacement and rotation stages, it was decided to mount the mirrors on hexapods [80], a platform able to move with 6 degrees of freedom.

To perform better statistical analysis and to scan a larger surface of the mirrors, it was decided to use 50 mm diameter optics instead of 25 mm ones. So the installation of hexapods and larger mirrors are the main highly visible upgrades but the remaining of the experiment will also benefit from updates, some of them detailed in the next sections.

3.3.2 *The hexapods*

The hexapods, one for each cavity mirror are at the core of the upgrade of the experiment. Hexapods are all based on the same principle of a moving platform attached to 6 linear actuators. By moving the pistons in a coordinated way, it is possible to arbitrarily position and orient the platform or any reference point attached to it. On top of the complex mechanical system, the difficulty comes from the computation required to drive 6 linked actuators to reproduce any position in a user selected arbitrary Cartesian system.

The two hexapods have been acquired after a call for tender and they are based on a modified BORA model from the company Symétrie [81]. The main specifications are detailed in the table 9. A photo of them, before installation in the vacuum chambers is shown in figure 36.

Table 9: Specifications of the hexapods.

Environment	
Clean room compatibility	up to ISO 5
Vacuum	up to 10^{-6} mbar
Low outgassing grease	Krytox low vapor pressure
Platform diameter	160 mm
Maximum weight	10 kg
Positioning	
Maximum displacement[a]	30 mm for $T_{X,Y}$,15 mm for T_Z
Maximum rotation[a]	10° for $\theta_{X,Y}$m 20° for θ_Z
Minimum displacement	0.1 µm
Minimum rotation	2 µrad
Repeatability displacement	1.5 µm

[a] Obtained for one axis at a time.

We also paid attention that the hexapods could be controlled by an external programming software (such as python or Matlab) so that a complex routine script could be written. This remark is also valid for all the other pieces of equipment of the setup which are connected either through the network or by serial ports to the main computer.

3.3.3 *Around the hexapods*

To measure the birefringence of the mirrors, one should be able to rotate them over a full circle, motion that is of course not possible with the sole hexapods. So we attached a custom small breadboard with M6 tapped holes on the hexapod platform to later install a rotation stage that will house the mirrors.

The choice of the rotation stage was not trivial as it must meet several of our requirements: first, it must be vacuum compatible, then it must have a clear aperture for the light to pass in transmission and then it must induce minimal misalignment while rotating the mirror (called wobble). Moreover, The aperture should be large enough to not clip the laser beam as the whole rotation stage and mirror will be shifted transversally by the hexapods.

After doing a market survey for such stage, our choice went for a Physik Instrumente model (reference L-611.991200V6 [82]). It is compatible up to 10^{-6} mbar and with a clear aperture of 35 mm diameter. The smallest rotation step is 10 µrad with a repeatability in one direction of 20 µrad and a wobble of ±15 µrad. The rotation accuracy is largely enough for your purpose and a misalignment of 15 µrad

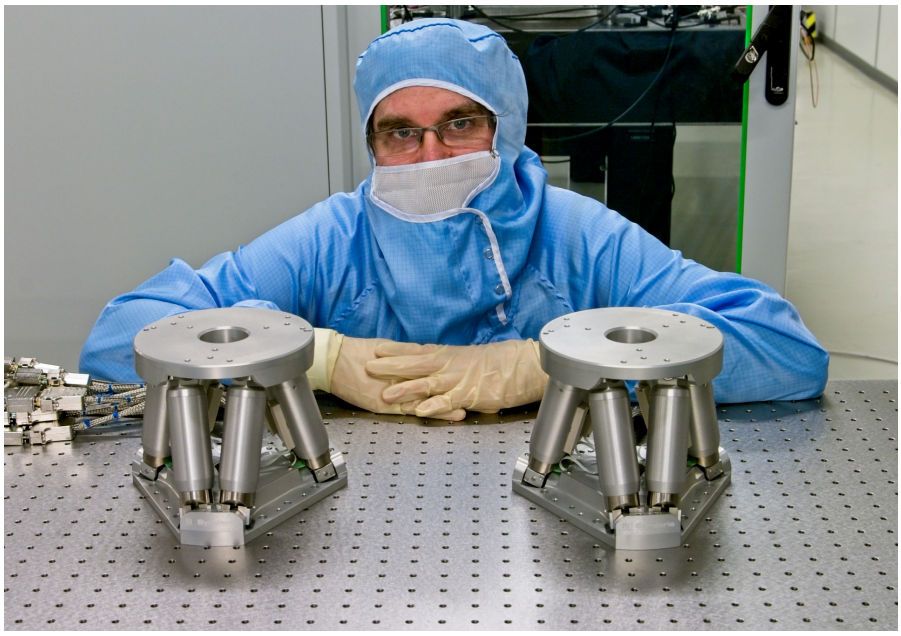

Figure 36: Photo of the 2 hexapods, a standard size human is also shown for scale.

only induces a drop in the circulating power of less than 5% when the cavity is locked.

To mount the mirror to the rotation stage, a custom adapter has to be made based on the same principle as the initial BMV mount. The mirror resting on two teflon rings is inserted into a cylindrical mount. To hold the mirror in place a diaphragm that we can screw comes on top of it. Mounts have been produced for mirrors with diameters of 50 mm and 25.4 mm.

A 3D sketch of the assembly including the hexapod and rotation stage is shown in the right part of figure 37.

To house the hexapods, new vacuum tanks had to be ordered. The new ones are much more spacious than the previous ones, easing the

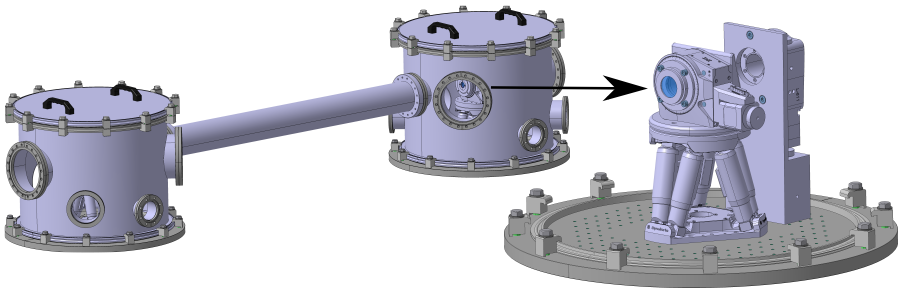

Figure 37: 3D CAD of the new vacuum tanks (left) with the view inside the tank of one hexapod with the mirror rotation mount (right). On the right of the hexapod, outside the cavity, there is another rotation stage to mount the Glan-Taylor polarisers which are at the input and output of the cavity.

mounting of the mirrors. The new tanks have a cylindrical shape as shown in figure 37 with a diameter of 550 mm for a height of 450 mm. Custom ports are inserted for the various electrical feedthroughs and viewports. For a latter use, we added a large window in front of the mirror to record qualitatively the amount of scattering light as a function of the position of the incident beam on the mirror.

3.3.4 *Photodiodes and electronic upgrades*

Several photodiodes have been upgraded. Here I detail the list and the motivation.

The photodiode in transmission of the cavity PD Trans is now a mode 2053-FS-M from Newfocus instead of the model 2011-FS-M, the casing is the same, the detector has the same diameter and gain but it has a much higher bandwidth (10 MHz vs 200 kHz) and it can operate with a power supply instead of a battery. The last point is important since in case of trouble with very little light at the output of the cavity, the level of the battery was always under suspicion as it is easy to forget to switch off the detector.

The previous transmission photodiode (model 2011-FS-M) has been moved to monitor the input power level (PD Pstab) instead of a Thorlabs one.

The photodiode looking at the reflection of the cavity PD Ref and used to derive the PDH error signal, is still from Qubig but it is custom made to have a larger diameter (twice larger, now 1 mm diameter) with a DC output. The last two points ease greatly the alignment of this photodiode. The larger diameter photodiode comes at a price of a reduced bandwidth (< 60 MHz) but it has no impact on our use since the sidebands frequency is at 10 MHz.

A new photodiode was added to look at the power entering the cavity (model S1 from Sisyph). It is a photodiode with a DC and AC outputs (cross over frequency at 500 kHz, bandwidth of 120 MHz) and it serves 2 diagnostic purposes: as a out of loop sensor to monitor the power stabilisation of the laser (DC output) and to monitor the Amplitude Residual Modulation (RAM) from the EOM (AC output).

Finally a quadrant photodiode (model Newfocus 2903) has been installed in reflection of the cavity and is used for the pre-alignment of the mirrors when we install them. This step is crucial to have from the start a relatively good alignment of the cavity and see the resonance peaks in transmission when scanning the laser frequency. Once the peaks are visible, in particular the fundamental one, a fine alignment of the two mirrors is done to maximise the transmission of this peak.

On the electronic front, the main upgrade is on the PID controller for the intensity stabilisation of the laser. Before it was done with a Red Pitaya and now it is a solution from Stanford Research Systems with the module SIM960 which can be used as stand-alone with a

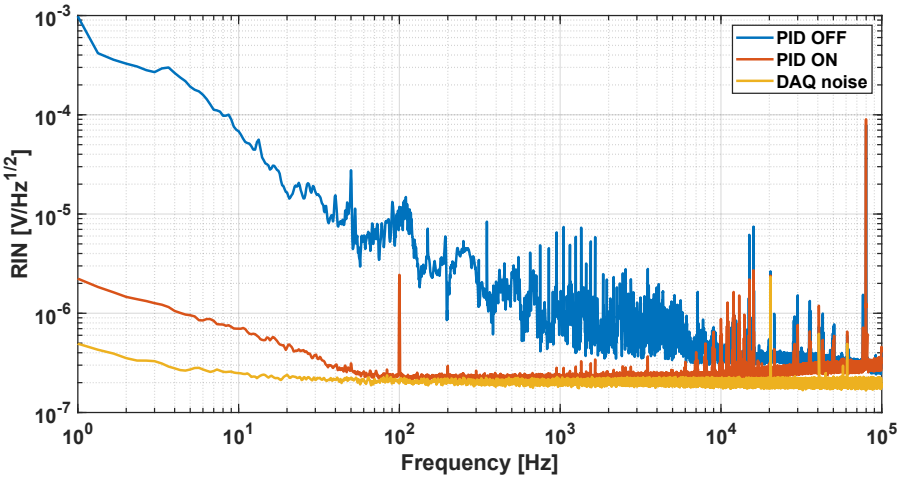

Figure 38: Amplitude power spectral density of the laser intensity noise at the entrance of the cavity. The intensity is measured with the out-of-loop photodiode S1.

bandwidth up to 100 kHz. It can also be controlled by the computer by sending a set of serial commands. That is particularly useful to remotely switch off the input laser light when the cavity is locked to perform the ringdown measurement. So far, for the stabilisation loop, only a proportional and integral gains are used with satisfactory results. An example of the intensity stabilisation in the frequency domain is shown in figure 38.

We replaced all the DC power supplies in the setup (24 V and ±15 V) by creating a derivation from the first stage of the stabilised power supply of the Sisyph box. This new cabling replaces the first price switching power supplies from Radiospare that we initially bought due to the tight budget.

A special effort was made to reduce the RAM from the EOM. To minimise the RAM, the EOM was re-centered and aligned and the input light polarisation finely tuned to matched the EOM crystal axis. The EOM crystal is also now actively stabilised in temperature with a thermistor monitoring the crystal temperature and a peltier module in its mount, achieving a temperature stabilisation of the order of 0.01K. As we have not yet relocked the cavity, it is difficult to estimate the benefit of this last change.

3.3.5 *Scattered light mitigation*

One thing we paid little attention to the first version of the experiment is regarding scattered light. The PVLAS experiment has shown it should not be taken lightly as it can create spurious signals and may limit the birefringence measurement [33]. So we decided to damp all the secondary beams and add light baffles wherever possible.

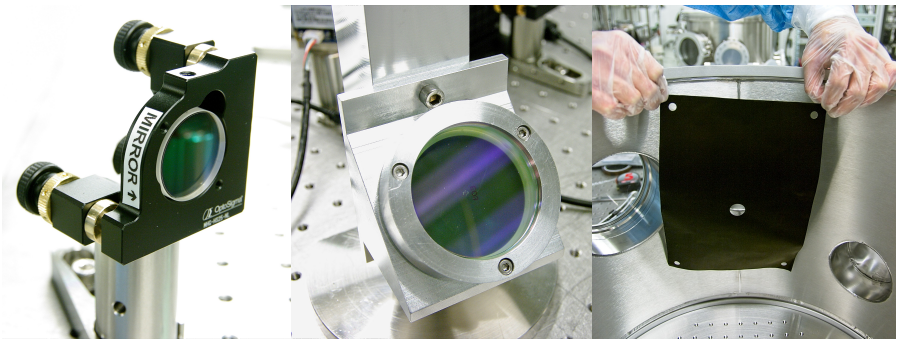

Figure 39: The installation of the Acktar absorbing material behind all the steering mirrors (left), periscope mirrors (middle) and later to be installed inside the cavity (right) to block the scattered light and limit the resonances of higher order optical modes by reducing the visible aperture of the cavity mirrors.

The baffles are made of disk or sheet of Acktar [83], one of those super-black materials which absorb most of the visible and infrared light. The sheet can even be cut to produce complex 2D geometry. The material has a low damage threshold so it can not be used to block or dump a direct laser beam but it is perfect to add baffles to stop the propagation of scattered light or faint secondary beams from imperfect AR coatings.

All the steering mirrors in the experiment have now a black disk behind them and all the known secondary beams are blocked with diaphragms or Aktar disk as seen in the figure 39. Not yet implemented at the time of writing but anticipated to be installed: a proper extraction of the reflected beam from the first in-vacuum polariser and two baffles made of Acktar with a clear aperture of 15 mm diameter to be inserted inside the cavity if needed to block the scattered light and also reduce the visible diameter of the mirror and so limit the generation of very high order optical modes (more in the section 3.4).

To avoid visible light from fluorescent tubes adding offset or harmonics to the measured signals, photodiodes with very low incident power (< 1 µW) have now a black tube in front with an optical passband filter centered on 1064 nm. The tube is threaded so a focusing lens could also be inserted and held in position by two rings.

3.3.6 *The complete assembly and status*

During the construction of the vacuum chambers, we anticipated all the custom mechanical parts needed to assemble everything together. The cavity beam height has changed so we also have to adjust the optics before and after the cavity. The assembly itself went smoothly and we quickly reached a vacuum of 0.2 mbar when we did the leak detection with a rough and turbo vacuum pumps. After several days

of pumping a level of 1×10^{-3} mbar was obtained, which is very satisfactory as in practice we only require a primary vacuum level of (0.1 mbar).

For illustration, photos of the assembly and the final look of the experiment can be found in 40.

At the time of writing, we are re-installing the mirrors for the low finesse cavity to characterise the new setup. This phase is rather quick and around autumn 2021, we should be able to lock the high finesse cavity and do the first ring down measurement and scan the cavity length.

Figure 40: Photo from the assembly including the final look of the new setup at the bottom.

Table 10: Comparison of the ratio of mirror clear aperture over the laser beam size between the AdV and BMV cavities.

		AdV	BMV
Substrate diameter	[mm]	350	25
Coating diameter	[mm]	330	23
Laser beam diameter	[mm]	107[a]	1.9
Ratio coating / laser		3.1	12

[a] Averaged beam size between input and end mirrors.

3.4 THEORETICAL CAVITY SCAN

We have seen in the previous chapter (section 2.3.5.1) that for particular cavity geometry or particular g-factor, the resonances of higher order optical modes could happen at the same time as that of the fundamental one. That is a detrimental situation as it could generate additional optical losses. In the Advanced Virgo cavity example, we scanned the RoC of the mirrors as seen in figure 14, in this section we will scan the length of the BMV cavity. Practically, thanks to the hexapods, we can translate the mirror longitudinally, changing the cavity length at maximum by 6 cm, compared to the overall cavity length of 158 cm.

We can already anticipate that the resonances of higher modes could be more an issue for the BMV cavity compared to Virgo. That is due to the higher finesse of the cavity, making the optical loss more critical but also because of the much larger mirrors compared to the laser beam size as detailed in the table 10.

A rough estimate about the maximum higher order mode which can be supported by the cavity could be derived knowing that a mode of order n will have a spatial extend $\sqrt{n}$ larger than the fundamental mode [60]. So for a higher order mode to not be supported by the cavity because it is heavily clipped by the finite aperture of the mirror, its order must be superior to the square of the ratio between the coating aperture and the laser fundamental mode diameters.

Using this criterion, for Advanced Virgo, only modes below the order 9-10 can resonate inside the cavity. For BMV, the situation is different as modes up to order 100 could still be present with moderate losses (several tens of ppm). Those very high order modes can theoretically resonate in the cavity but can they really be present since in practice they have a very small overlap with the laser fundamental mode that we inject ?

To answer this question, we set up an optical simulation of a BMV style cavity similar to the one we have at LMA. In the simulation, we assume excellent mirrors with a surface quality better than $\lambda/20$.

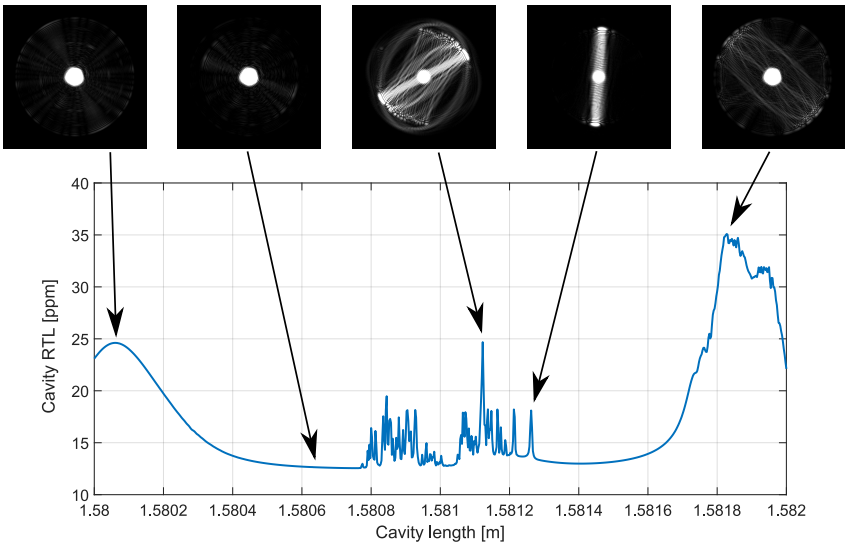

Figure 41: Cavity round trip loss when the length is scanned over 2 mm. The image of the circulating field is shown on top for some lengths. All the images have the same vertical scale with the central TEM_{00} saturated to reveal the higher order modes. Without the RTL, the cavity finesse is set to 500 000. A movie of the scan has been uploaded to youtube [84].

The input beam in a TEM_{00} is optimally aligned with the cavity and mode matched to the equivalent perfectly spherical mirrors.

Due to the incertitude in the positioning of the element of the cavity, it is very difficult to build the cavity to a very precise fixed length. So we do the hypothesis that after the installation of the mirrors, the length of the cavity will be between 1580 mm and 1582 mm. This 2 mm tolerance can greatly change the round trip loss of the cavity as seen in figure 41. The peaks in the RTL for some cavity lengths are due to the resonances of higher order modes at the same time as the fundamental one. Due to the high density of the peaks, we can not rely only on sheer luck to achieve the lowest cavity RTL, we have to tune and scan the cavity length, which is another motivation for the installation of the mirrors on the hexapods.

The figure 41 illustrates one of the drawbacks of having too large mirrors, a very large number of higher order modes could be resonating with almost the same gain as the fundamental mode. What is remarkable is that such modes could be excited even if our cavity is near perfect: very good surface mirrors, optimal alignment and mode matching do not prevent the generation of higher order modes. The phenomenon is exacerbated by the very high finesse of the cavity since even if only a very small fraction of the fundamental mode is converted to the resonant higher order modes at each round trip, the very high number of round trip (order of 10^5) makes the presence of the parasite mode well noticeable in the scan.

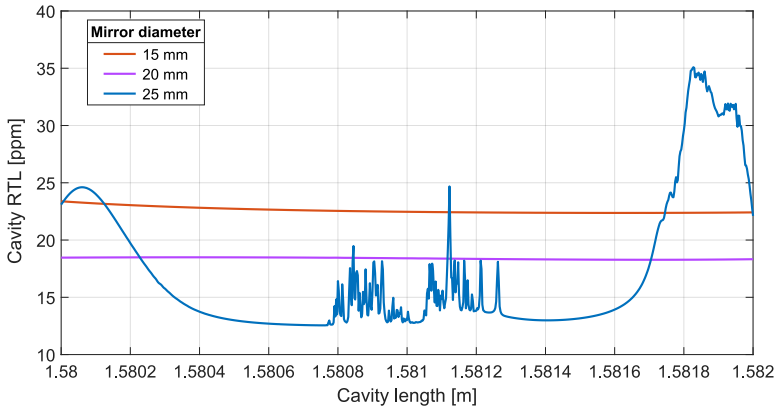

Figure 42: Cavity round trip loss when the length is scanned over 2 mm for three different mirror diameters.

Based on this understanding, one can try two hypotheses first to reduce the clear aperture of the mirrors in the cavity. In the simulation it is done by reducing the coating diameter, in practice, we will add a baffle with a hole centered on the optical axis as shown in the right part of figure 39.

The same cavity scan as before with reduced mirror apertures is shown in figure 42 for three coating diameters: 25 mm, 20 mm and 15 mm. As expected, decreasing the mirror size eliminates the resonances of the optical modes of very high order. However, it comes at the price of an increase of the losses of the TEM_{00} as well.

The impact of the finesse on the round trip loss is shown in 43 for the same scan of the cavity length. As expected, lowering the finesse helps to achieve lower round trip loss when higher order optical modes are present. However, only by reducing the finesse by 100, from 500 000 to 5000 that the change is noticeable. So, this approach is seldom possible in practice as it also reduces the amplification gain of the Fabry-Perot cavity and so strongly limits its interest. To be noticed that the loss of the fundamental mode is insensitive to the change of the finesse.

3.5 SIMPLE FORMULAS

As for the Advanced Virgo arm cavity (section 2.7), we can derive simple formulas helpful to get the right order of magnitude of the relevant parameters. In the case of a BMV style cavity, several assumptions could be made: first the transmission T_1 and T_2 of the input and end mirrors are identical and called T, $T = T_1 = T_2$, second, T is in the order of few ppm. Then the cavity loss L (excluding the mirrors transmission) is assumed to be also very small and on the same magnitude as the transmission T.

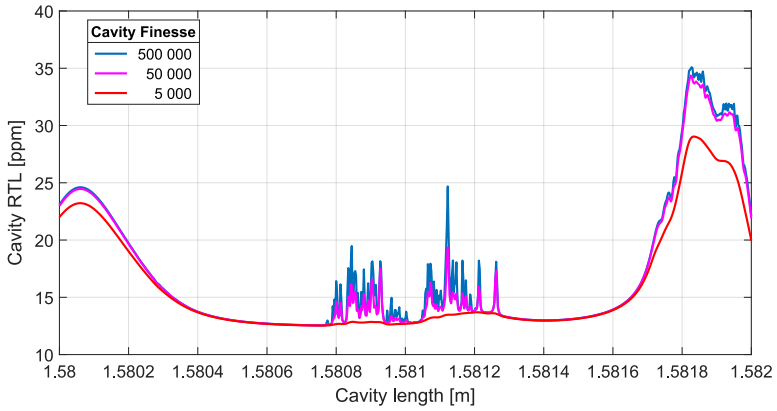

Figure 43: Cavity round trip loss when the length is scanned over 2 mm for three different finesse. The finesse is lowered by increasing the transmission of both input and end mirrors.

3.5.1 *Finesse*

Using the same starting point as for the Virgo arm cavity (see section 2.7.1), the finesse $\mathcal{F}$ could be approximated as:

$$\mathcal{F} \approx \pi \frac{\sqrt[4]{(1-T)(1-T)(1-L)}}{1-\sqrt{(1-T)(1-T)(1-L)}} \tag{35}$$

$$\approx \pi \frac{\sqrt[4]{(1-2T-L)}}{1-\sqrt{(1-2T-L)}} \tag{36}$$

$$\approx \pi \frac{(1-\frac{T}{2}-\frac{L}{4})}{1-1+T+\frac{L}{2}} \tag{37}$$

Since the transmission and loss are very small ($T, L, \ll 1$), that leads to the final simplified formula:

$$\boxed{\mathcal{F} \approx \frac{2\pi}{2T+L}} \tag{38}$$

3.5.2 *Cavity power gain*

Similarly, starting from equation 19 from section 2.7.2. The circulating power in the cavity P_{circ} could be written as:

$$P_{circ} \approx \frac{T}{\left(1-(1-T-\frac{1}{2}L)\right)^2} P_{in} \tag{39}$$

$$\approx \frac{T}{\left(T+\frac{1}{2}L\right)^2} P_{in} \tag{40}$$

$$\boxed{P_{circ} \approx \frac{4T}{(2T+L)^2} P_{in}} \tag{41}$$

Which can not be further simplified without some restrictive assumptions. It can also be expressed as a function of the finesse but it is not necessarily easier to remember:

$$P_{circ} \approx T \left(\frac{\mathcal{F}}{\pi} \right)^2 P_{in} \tag{42}$$

Same as in the previous chapter, the transmitted power P_{trans} is:

$$P_{trans} = P_{circ} T_2 \tag{43}$$

$$\tag{44}$$

3.5.3 *Reflected power*

Same as usual, we start from the generic equation derived in the previous chapter, in that case, the equation 26 from section 2.7.3. From that equation, one can directly arrive to:

$$P_{ref} \approx \left(\frac{\frac{1}{2}L}{T + \frac{1}{2}L} \right)^2 P_{in} \tag{45}$$

$$\tag{46}$$

So giving the final simplified formula:

$$\boxed{P_{ref} \approx \left(\frac{L}{2T + L} \right)^2 P_{in}} \tag{47}$$

4 CONCLUSION

Even if Fabry-Perot cavities are rather straightforward devices: a laser with two mirrors facing each other separated by a length, the behavior of such a system is complex and the research is still going on to master this simplest form of optical resonators. Personally, I still see myself working in this domain for the remaining of my career as more and more challenging cavities are expected in the future. I have already some plans for my future work that I detailed in the next sections.

4.1 THE COMING FEW YEARS

4.1.1 *Advanced Virgo+*

At the time of writing (summer 2021), Advanced Virgo+ phase I is in commissioning mode after a set of upgrades (higher laser power, addition of a signal recycling mirror, new quantum reduction scheme at the detection). The goal is to achieve better sensitivity, increasing the range of the detector by at least 50% to start a new data taking period O4 in September 2022. The arm cavity mirrors have not been changed and so are already well characterised from previous commissioning periods.

However optical characterisation activities are still performed to understand the performances of the detector. First, new techniques of characterisation are explored since the control of the interferometer has changed with the installation of the signal recycling mirror. As an example the lock acquisition is different and our previous analysis scripts are no longer valid as the interferometer now passes through different steps to reach the operating point.

Second, it is important to monitor the optical losses in the arm cavities to spot any degradation over time since the mirrors were installed already six years ago. Moreover, practically the losses are dependent on the circulating power in the cavity. As the input power is gradually increased, a change of losses should also be expected (even if we are looking for ways to mitigate this effect).

Third, this work is usually done with PhD students and post-docs, remotely and partially on site. So every 2-3 years, it is necessary to initiate new people in the art of optical characterisation.

Around the years 2023-2024, at the end of the science run O4, new arm cavity mirrors will be installed on site. Those new optics will likely benefit from better coating and also the end mirrors will be

larger (diameter of 550 mm) to further reduce the coating thermal noise. A new campaign of measurement will be performed on site to measure the finesse, g-factor and round trip loss of the cavities following the same techniques previously validated.

I still plan to be the coordinator of the optical characterisation of Advanced Virgo for several years. It is a way to keep contact with the detector and this work mixes nicely experiments and simulations. Once we notice a deviation from the expected parameters on site, we try to explain it by testing hypothesis in simulations. The measured parameters are also fed back to the simulations of the interferometer for other sub-systems to provide more realistic results and also investigate strategies to further increase the sensitivity.

4.1.2 *BMV@LMA*

For the second topic of this memoir, the BMV style cavity at LMA, the road map is also clear. Since the installation is more or less completed, the next phase is the automation of the setup to perform automatic cavity ring-down measurements. That would mean locking the cavity, unlock and record the transmitted power, move one cavity mirror and redo. The various steps have been tested separately but they must now be integrated in the same script and also would need to be tested over several hours to check that any drifts are well-handled (slow misalignment comes to mind).

Two kinds of scans will be performed: the 2D transverse scans of one mirror to check the uniformity of the optical loss on the surface and then cavity length scans to check the impact of the cavity degeneracy on the loss measurement as highlighted by the simulations. The last scan could also be repeated with different mirror apertures to confirm that adding an aperture may reduce the optical loss by suppressing the resonance of very high order optical modes.

At the end of 2021, new polarisers will also be installed before and after the cavity to measure the birefringence of substrates or coatings. It is the second use of this cavity. In the short term, several campaigns will be made to measure the birefringence of several sapphire substrates and correlate the results with the growth parameters of the crystals (pulling speed, seed rotation and crucible rotation). The final goal is to reduce the optical absorption as well as the birefringence of sapphire, first on small samples (diameter 30 mm) and then on larger ones (diameter 450 mm), size compatible for future cryogenic GW detectors.

In the longer term, we should aim to match the measured optical loss with surface measurements and have a model for the loss induced by point defects which are the main source of scattering of very high reflecting coatings. So before installation, the surface of the mirrors could be characterised with the optical profilometer to mea-

sure the roughness and density and size of defects. Viewports have already been installed facing the mirror surfaces, so infrared cameras will be installed to quantify the amount of scattered light when the cavity is on resonance with more than 1 kW of light circulating. As before, transverse scans will be done and excess optical losses for certain positions should be matched with the presence of surface defects.

4.1.3 *OSCAR*

I hope to be able to continue developing my optical simulation code OSCAR. All the cavity simulations from this memoir were made with OSCAR and this tool is also used within several groups, even outside the GW community. Two main large tasks are on the development plan: first, include polarisation effects in the simulations and in particular the possibility to add 2D birefringence maps and the second task is to perform the most intensive calculations in the computer GPU (Graphics Processing Unit). GPUs are high specialised processors for graphic cards which excel in parallel computing tasks. That would benefit to OSCAR as most of the operations are multiplication element wise of large matrices and 2D FFT. From very preliminary results a gain in speed of 14 could be expected when using a grid size of 512×512 pixels.

An effort should be made also to update the documentation but unfortunately, my free time is missing but the will is there.

4.1.4 *Einstein Telescope*

Einstein Telescope will be the successor of Virgo in the European continent. It will be the next generation GW detector able to listen to all the stellar-mass black hole fusions since the big bang with a cosmological reach up to redshift $z = 100$. With hourly detection and events with very high SNR, it opens the realm of high precision testing of general relativity. The observatory is a very ambitious project, with 10 km long underground arm cavities, mirrors of 200 kg with cryogenic and room temperature interferometers at the same location. So far the project is unfunded but it has a high priority in the list of the future European large research infrastructures. It is expected to record its first data around 2035.

Presently, we are in the design phase, with the goal to release a Technical Design Report (TDR) for the infrastructure around 2023 and another one for the interferometer 2 years later. Thanks to my experience acquired with Virgo, I am co-chair of the division interferometer (which manages 6 work packages) and a member of the Instrumental Science Board (ISB).

I will continue this leading role and participate in the design of the Einstein Telescope. The aim is to find the best optical configuration

to have a robust detector against aberrations with well diagonalised error signals for easy control. The mirror substrates for the cryogenic interferometer is already expected to be one of the main challenges as we are looking for very large ingots of silicon or sapphire, defect-free and with a very high purity.

4.2 NEXT GENERATION MIRRORS OPTICS

One trend is already obvious in the field of GW detection: the next generation of instruments will be longer and so the mirrors will be larger. We mentioned already the Einstein Telescope, but its American counterpart Cosmic Explorer will even be more gigantic with 40 km long arms and 300 kg mirrors. The procurement of such mirrors is likely possible but will require substantial technological development for the large substrates but also to achieve the polishing and coating on very large diameters. So the future is big and we can already see a similar tendency for optical dichroic filters for visible and near-infrared astronomy as telescopes are getting larger and larger.

For much smaller optics, new technologies are emerging to replace the traditional coating deposition. Two ideas I found fascinating which open new possibilities: the technique of transferring coatings from one substrate to the other which has opened the way to crystalline coatings [85] but the same principle could also be achieved with amorphous coating. So the coating could be produced and characterised in advance, even on different kinds of substrates and then at a later time transferred to the final polished substrate. In this way, we could have access to coating machines or deposition techniques that can only process very thin substrates (wafers) and then later transfer the coating on a much thicker substrate.

The second idea is even more disruptive as the high reflectivity function is no longer made of Bragg reflectors. Current mirrors are a cumulative stack of the two layers of different refractive indexes, the higher the number of layers, the higher the reflectivity. A nanostructuring of a surface can also achieve great reflectivity. A controlled pattern of holes with sub-wavelength diameters made by lithography can reflect 99.95% for a given wavelength [86]. Other optical functions can be also be achieved depending on the spacing and geometry of the holes [87].

In conclusion, numerous challenges are ahead as never-been-done mirrors in size or specifications are required for future experiments, pushing further the technological limits of very low loss optics. In this context, I hope that my contribution will still be relevant and help to achieve scientific progress.

Part I

APPENDIX

A SELECTION OF PUBLISHED ARTICLES

In this chapter, a selection of 5 articles where I have a large direct contribution during my time at LMA. Those articles reflect directly my research activities but are only a small fraction of all my published articles during the last 10 years. The majority of my publication list is made of articles on astrophysical results from the LIGO-Virgo collaboration where I am one author among one thousand other ones.

In chronological order, my selection:

1. On page 87, my first article done in the framework of the Einstein Telescope preliminary design study. A cryostat was installed at LMA around an optical absorption measurement setup, based on the mirage effect. This characterisation technique is well mastered at LMA since two other benches are already present but working mainly at 1064 nm. This new bench was dedicated to measure the optical absorption of silicon at 1550 nm and we were able to measure one of the lowest published absorptions for this material. The link between resistivity and optical absorption was also highlighted.
   Degallaix, J., et al. "Bulk optical absorption of high resistivity silicon at 1550 nm." Optics letters 38.12 (2013): 2047-2049.
   https://doi.org/10.1364/OL.38.002047

2. One year after this first publication, a second article (page 90) with the measurement of the absorption of silicon at cryogenic temperatures. This research was done in collaboration with the group of Jena working on the same topic at that time. We demonstrated that the silicon optical absorption is not necessarily reduced by free carrier freezeout as the temperature is lowered. It has an important implication for the Einstein Telescope as we should not expect large a improvement in optical absorption as the arm cavity mirrors are cooled down.
   Degallaix, J., et al. "Measurement of the optical absorption of bulk silicon at cryogenic temperature and the implication for the Einstein Telescope." Classical and Quantum Gravity 31.18 (2014): 185010.
   https://doi.org/10.1088/0264-9381/31/18/185010

3. On page 103, the reproduction of an article describing the round trip loss of a Fabry-Perot cavity with realistic surface maps. This work was particularly relevant to design filtering cavities in laser GW interferometers which allow the manipulation of the quantum properties of light. It is the only paper of the list

where I am not the first author (but second), the first one being the PhD student I was supervising.
Straniero, N., et al. "Realistic loss estimation due to the mirror surfaces in a 10 meters-long high finesse Fabry-Perot filter-cavity." Optics express 23.16 (2015): 21455-21476.
https://doi.org/10.1364/OE.23.021455

4. A review of the outstanding large mirrors which have detected gravitational waves is on page 125. The properties of the fused silica substrates, the polishing and coating performances are all detailed in a single article. It was written for a special issue of JOSA: classical optics in France.
Degallaix, J., et al. "Large and extremely low loss: the unique challenges of gravitational wave mirrors." JOSA A 36.11 (2019): C85-C94.
https://doi.org/10.1364/JOSAA.36.000C85

5. The article on page 135 summarises the possibilities of the simulation code OSCAR that I developed. I put a special emphasis on the contribution of the code to the design of Advanced Virgo. The article was published in a special issue on softwares that contributed to gravitational wave discovery.
Degallaix, J. "OSCAR: A MATLAB based package to simulate realistic optical cavities" SoftwareX 12 (2020): 100587.
https://doi.org/10.1016/j.softx.2020.100587

June 15, 2013 / Vol. 38, No. 12 / OPTICS LETTERS 2047

Bulk optical absorption of high resistivity silicon at 1550 nm

Jerome Degallaix,* Raffaele Flaminio, Danièle Forest, Massimo Granata, Christophe Michel, Laurent Pinard, Teddy Bertrand, and Gianpietro Cagnoli

Laboratoire des Matériaux Avancés, IN2P3/CNRS, Université de Lyon, 7 Avenue Pierre de Coubertin, Villeurbanne 69100, France

**Corresponding author: j.degallaix@lma.in2p3.fr*

Received April 2, 2013; revised May 13, 2013; accepted May 13, 2013; posted May 13, 2013 (Doc. ID 188197); published June 4, 2013

We report on the measurement of the optical absorption of bulk crystalline silicon at 1550 nm. Using the photodeflection technique, absorption as low as 5 ppm/cm has been measured on a sample with a resistivity of $10\,k\Omega \cdot \mathrm{cm}$. The absorption as a function of the resistivity has been derived for n-type silicon.

OCIS codes: (300.1030) Absorption; (040.6040) Silicon.
http://dx.doi.org/10.1364/OL.38.002047

For the third generation of gravitational wave detectors (an astronomical instrument based on laser interferometry [1]), silicon has been selected as the material candidate for the main mirror substrates [2]. Some unique features make silicon particularly attractive for future large cryogenic interferometers: for example, silicon high purity substrates are available in large diameters and now wafer diameter up to 450 mm. Moreover, silicon has very good physical properties at low temperatures, such as low mechanical loss [3] and high thermal conductivity [4], properties essential to mirrors for gravitational wave interferometers.

To keep the mirror at a low temperature (~10 K) during interferometer operation, it is necessary for the mirror to present very low optical absorption in order to not generate excess heat. As an example, for the transmissive mirror of the Fabry–Perot arm cavity, an absorption of a few ppm/cm at 1550 nm is required [5].

The intrinsic absorption of high resistivity silicon is supposed to be very low at 1.5 μm [6] but direct measurements have only recently been attempted [7,8]. The Laboratoire des Matériaux Avancés, building on its experience with low optical loss measurement [9], has setup a new metrology bench to measure the optical absorption of silicon at 1550 nm. Even if all the measurements reported here are done at room temperature, the silicon sample tested is housed within a cryostat for further experiments. To our knowledge, the crystalline silicon bulk absorption reported in this Letter (4.3 ppm/cm) is the lowest ever measured.

This Letter is organized as follows: first, the techniques used to measure the optical absorption are explained. Then, the characteristics of the tested samples and the analysis of the experimental data are detailed. Finally, the intrinsic absorption at 1550 nm as a function of the material resistivity is given.

Depending on the range of expected absorption to be measured, two techniques of measurement can be used. The first one is based on energy conservation while, the second is based on the photodeflection technique.

The first technique is straightforward but only works for highly absorptive material, typically with bulk absorption $\alpha > 0.1$ /cm. It is based on the power balance: what is not reflected or transmitted by a sample is absorbed, assuming negligible scattering.

Practically, a laser beam at 1550 nm is sent toward the sample, while the total powers transmitted and reflected by the sample are measured using a powermeter. It is a relative measurement since all the powers are normalized by the laser's incident power. From the normalized transmitted and reflected powers, the coefficient of reflectivity of silicon as well as the volume absorption can be derived. Since we are testing uncoated silicon samples, this last calculation must take into account the multiple reflections occurring within the samples.

The photodeflection technique is commonly used to measure the very low optical absorption of the material [10]. As an example, using this method, fused silica bulk absorption as low as 0.3 ppm/cm at 1064 nm has been measured for the mirror substrates of the gravitational wave detectors. We are now applying the same technique to test silicon substrates.

A photodeflection bench is composed of two lasers. The first one, the pump laser, is a high power laser at the wavelength of interest for the absorption. The second one, the probe laser, is at low power and at a different wavelength in the transparency domain of the test sample. The pump laser is partially absorbed in the sample and thus a temperature gradient is created within the substrate. The temperature gradient induces a refractive index gradient, which deviates the probe beam. The deviation of the probe beam is then proportional to the optical absorption of the sample.

The typical setup is shown in Fig. 1. In order to not be limited by the beam jitter noise of the two lasers, a standard technique of modulation/demodulation is used with a modulation frequency typically of a few hundred hertz. The beam radius of the pump laser is 700 μm within the sample, a good compromise to allow a large deviation signal linked to the absorption while limiting the non linear effect due to the high intensity beam. The probe beam is focused on the sample and has a beam radius of 230 μm.

In addition to its high sensitivity, the photodeflection technique presents other advantages: it is possible to measure either the volume (bulk) absorption or the

0146-9592/13/122047-03$15.00/0

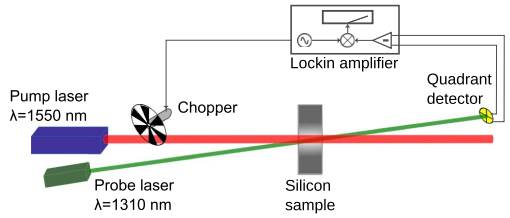

Fig. 1. Setup of a metrology bench using the photodeflection technique. In our case, the pump laser has a maximum continuous power of 30 W, while the probe laser is only 2 mW.

surface absorption in the presence of a high reflectivity coating by adjusting the respective position of the pump and probe beams. Moreover, by moving the sample while measuring, one can also produce two-dimensional or even three-dimensional absorption maps of the sample [11].

One drawback of this measurement is the difficulty to calibrate the bench accurately. The deviation of the probe beam, proportional to the absorption, is measured as the difference of intensity between two photodiodes and then demodulated by a lock-in amplifier. The absorption raw results are usually in V and can only be converted in the unit of absorption (cm^{-1}) using reference samples with known absorption.

The tested samples were made of silicon with different resistivities, but all were doped with phosphorus (n-type). The bulk samples have all a diameter of 50.8 mm and their thicknesses varies from 20 to 31 mm. The two parallel surfaces are flat with a roughness less than 5 Å. No coating (high reflectivity or anti reflectivity) has been deposited on the samples. A summary of the five samples tested is shown in Table 1.

The resistivity has been measured at five different points on both sides on the samples ST1, ST2, and ST3 and the variation is below 12%. For ST4, the resistivity was measured only in one point at the center. Regarding the sample SiMat, the resistivity is an estimate from the vendor but no measurement results were provided.

For each sample, the same measuring protocol and analysis has been applied. The different steps are described below for one sample:

1. The probe beam deviation due to the absorption is recorded for 11 different powers of the pump laser. For each power, the deviation signal is recorded for 4 min.
2. During the analysis, the deviation signal is first normalized by the optical power of the probe beam. In that way, the measurement is insensitive to the variation of the power of the probe laser due to the absorption in the sample or due to internal laser fluctuations. Then, the averaged signal over the 4 min for each pump power is derived.
3. The plot of the deviation as a function of the pump power is shown in Fig. 2 for sample ST4. From this data, the coefficient of proportionality (the slope of the fitted line) S between the deviation and pump power is calculated as well as the errors.

Table 1. Characteristics of the Silicon Samples Tested

Name	Resistivity [Ω · cm]	Growth Technique	Orientation
ST1	0.167 ± 0.014	Czochralski	⟨110⟩
ST2	2.84 ± 0.24	Czochralski	⟨100⟩
ST3	13.0 ± 1.43	Czochralski	⟨111⟩
ST4	808	Float zone	⟨111⟩
SiMat	10,000	Float zone	⟨100⟩

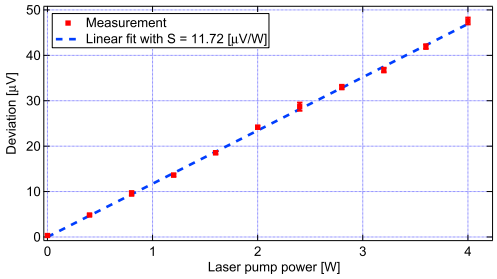

Fig. 2. Uncalibrated deviation as a function of the laser pump power for the silicon sample ST4. Linear fit with the derived parameter S is also shown.

Through this Letter, for all the analysis and results presented, the measurement error bars are calculated as twice the standard deviation to give a confidence interval of 95%.

As mentioned earlier, to be able to calibrate the photodeflection measurement a reference absorption is required. Such a reference can be given with the ST1 sample, the most absorptive sample in our possession. For that purpose, the bulk absorption must be measured with an independent method such as the one based on the energy conservation principle. Using this method the absorption has been found to be:

$$\alpha_{ST1} = 0.272 \pm 0.015/\text{cm}. \tag{1}$$

The absorption measurement has also been confirmed independently by spectroscopic measurements. Once the absorption of ST1 is known, all the deviation measurements can be calibrated against with a simple formula. Taking the example of sample ST4, its absorption α_{ST4} can be calculated as:

$$\alpha_{ST4} = \frac{S_{ST4}}{S_{ST1}} \times \alpha_{ST1}, \tag{2}$$

where S is the deviation slope previously calculated. From Eq. (2), one can also derive the error σ_α on the absorption measurement by knowing the error on the slope (σ_S) as well as the error measurement of the absorption of ST1 ($\sigma_{\alpha ST1}$) [12] (still with ST4 as example):

$$\left(\frac{\sigma_{\alpha ST4}}{\alpha_{ST4}}\right)^2 = \left(\frac{\sigma_{SST4}}{S_{ST4}}\right)^2 + \left(\frac{\sigma_{SST1}}{S_{ST1}}\right)^2 + \left(\frac{\sigma_{\alpha ST1}}{\alpha_{ST1}}\right)^2. \tag{3}$$

The error on absorption is typically dominated by the error on the absorption of ST1, which is used for the calibration. Only for the SiMat sample, the error on calibrated absorption is due to the incertitude on the

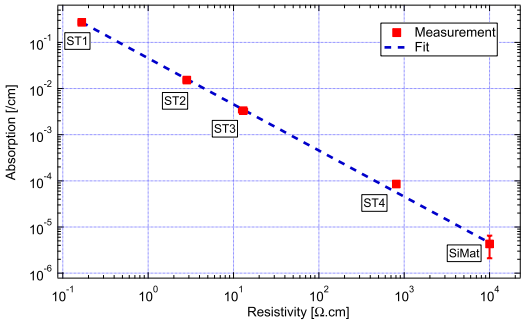

Fig. 3. Bulk optical absorption as a function of the resistivity for silicon material at 1550 nm. For the samples ST1 to ST4, the error bars are within the square data points.

deviation slope S, a consequence of the deviation signal being close to the detection noise (SNR ~ 2).

The calibrated absorption measurement on the five different samples as a function of the resistivity is shown in Fig. 3. The fit is also shown, and the following relationship between optical absorption α[/cm] and resistivity R [$\Omega \cdot$ cm] is derived as:

$$\alpha = (0.0454 \pm 0.0007)\frac{1}{R}. \quad (4)$$

In our measurement, the lowest optical absorption measured is 4.3 ppm/cm for the silicon sample with a resistivity of 10 kΩcm. The source of the absorption at 1550 nm is due to the presence of an absorption band in n-type silicon centered around 2300 nm as shown by Spitzer and Fan [13]. This absorption band is associated with the excitation of a free carrier in the conduction band to a higher energy level and hence the absorption is proportional to the concentration of the conduction electrons.

We have measured the intrinsic optical absorption of silicon at 1550 nm as a function of the resistivity. The lowest absorption measured at room temperature is 4.3 ppm/cm which confirms silicon as a promising material for transmissive mirror substrates. For the Einstein telescope, the influence of temperature on substrate absorption will have to be determined and the next step will be to attempt similar absorption measurements at a low temperature.

A similar study, absorption versus resistivity, will also be done on p-type silicon which does not present the absorption band previously mentioned. In that case the absorption may be lower and dominated by the free carrier absorption.

The authors gratefully acknowledge the support of the European Gravitational Observatory (EGO) and of the Lyon Institute of Origins (LIO).

References

1. M. Pitkin, S. Reid, S. Rowan, and J. Hough, Living Rev. Relativity **14**, 5 (2011).
2. ET science team, Class. Quantum Grav. **27**, 194002 (2010).
3. R. Nawrodt, A. Zimmer, T. Koettig, C. Schwarz, D. Heinert, M. Hudl, R. Neubert, M. Thürk, S. Nietzsche, W. Vodel, P. Seidel, and A. Tünnermann, J. Phys. Conf. Ser. **122**, 012008 (2008).
4. C. J. Glassbrenner and G. A. Slack, Phys. Rev. **134**, A1058 (1964).
5. ET science team, "Einstein gravitational wave Telescope conceptual design study," Tech. Rep. ET-0106C-10 (Einstein Telescope Project, 2011).
6. M. A. Green, Sol. Energy Mater. Sol. Cells **92**, 1305 (2008).
7. J. Steinlechner, C. Krüger, N. Lastzka, S. Steinlechner, A. Khalaidovski, and R. Schnabel, Class. Quantum Grav. **30**, 095007 (2013).
8. R. Bassiri, M. R. Abernathy, R. L. Byer, K. Craig, and K. Evans, "Coatings Research Overview," Tech. Rep. LIGO-G1300266 (LVC Meeting, 2013).
9. B. Cimma, D. Forest, P. Ganau, B. Lagrange, J.-M. Mackowski, C. Michel, J.-L. Montorio, N. Morgado, R. Pignard, L. Pinard, and A. Remillieux, Proc. SPIE **5252**, 322 (2004).
10. W. B. Jackson, N. M. Amer, A. C. Boccara, and D. Fournier, Appl. Opt. **20**, 1333 (1981).
11. Z. Yan, L. Ju, C. Zhao, S. Gras, D. G. Blair, M. Tokunari, K. Kuroda, J.-M. Mackowski, and A. Remillieux, Appl. Opt. **45**, 2631 (2006).
12. P. Bevington and D. Robinson, *Data Reduction and Error Analysis for the Physical Sciences* (McGraw-Hill, 2003).
13. W. Spitzer and H. Y. Fan, Phys. Rev. **108**, 268 (1957).

IOP Publishing Classical and Quantum Gravity
Class. Quantum Grav. **31** (2014) 185010 (13pp) doi:10.1088/0264-9381/31/18/185010

Measurement of the optical absorption of bulk silicon at cryogenic temperature and the implication for the Einstein Telescope

J Degallaix[1], J Komma[2], D Forest[1], G Hofmann[2], M Granata[1], D Heinert[2], C Schwarz[2], R Nawrodt[2], L Pinard[1], C Michel[1], R Flaminio[1] and G Cagnoli[1]

[1] Laboratoire des Matériaux Avancés, IN2P3/CNRS, Université de Lyon, 7 Avenue Pierre de Coubertin, F-69100 Villeurbanne, France
[2] Friedrich-Schiller-Universität Jena, Institut für Festkörperphysik, Helmholtzweg 5, D-07743 Jena, Germany

E-mail: j.degallaix@lma.in2p3.fr

Received 23 May 2014, revised 10 July 2014
Accepted for publication 17 July 2014
Published 28 August 2014

Abstract
We report in this article on the measurement of the optical absorption of moderately doped crystalline silicon samples at 1550 nm, which is a candidate material for the main optics of the low temperature interferometer of the Einstein Telescope (ET). We observe a nearly constant absorption from room temperature down to cryogenic temperatures for two silicon samples presenting an optical absorption of 0.029 cm^{-1} and 780 ppm cm^{-1}, both crystals doped with boron. This is in contradiction to what was assumed previously—a negligible optical absorption at low temperature due to the carrier freezeout. As the main consequence, if the silicon intrinsic absorption can not be lowered, the cross section of the mirror suspension of the ET must be increased to be able to carry away the excess heat generated by the partially absorbed laser beam during the operation of the interferometer.

Keywords: silicon, Einstein Telescope, optical absorption
PACS numbers: 78.40.Fy, 04.80.Nn, 95.55Ym

(Some figures may appear in colour only in the online journal)

1. Introduction

The Einstein Telescope (ET) is a European project aimed at directly detecting gravitational waves from astrophysical sources on a daily basis [1]. This detector is the planned successor

of the Advanced LIGO and Advanced Virgo interferometers currently in their installation phase and early commissioning [2]. Those advanced detectors are expected to achieve the first direct detection of a gravitational wave within the next five years and hence open a new window to study the universe, complimentary to our current vision based on the electromagnetic spectrum.

To greatly increase the detection rate in the following decade, the ET has been designed to be ten times more sensitive than the advanced detectors [1], probing a volume of space a thousand times larger. To achieve this goal, this observatory will be composed of two complementary interferometers sharing a common underground infrastructure. One high frequency interferometer (ET-HF) will be at room temperature with fused silica mirrors similar to the advanced detectors. The low frequency interferometer (ET-LF) will be more innovative using silicon mirrors operating at cryogenic temperatures.

Since the cavity input test masses made of silicon will be used in transmission, the optical absorption is an essential parameter which determines the amount of heat generated in the optics, which is equal to the amount of heat to be removed through the suspensions in order to keep the mirrors at their operating cryogenic temperature [3]. Additionally it seems unlikely that high purity silicon (or even intrinsic silicon having no significant doping/impurities) will be available in large enough pieces being suited for ET. Thus the focus of this work lies on moderately doped silicon that can be provided by Czochralski growth of single crystals; by 'moderately' we mean samples with resistivities ranging from few Ω cm to few kΩ cm.

Contrary to the low temperature regime, the optical absorption of bulk silicon at room temperature and in the near infrared is well understood and characterized [4, 5]. The optical absorption is proportional to the amount of free carriers (the proportionality coefficient been simply called the free carrier coefficient). At room temperature the concentration of the free carriers is itself equal to the concentration of dopant impurities as every atom of dopant is ionized and gives either one electron in the conduction band (n-type) or one hole in the valence band (p-type). In the case of moderately doped samples all dopants are ionized at room temperature. Thus, the concentration of free carriers is equal to the concentration of doping elements.

At cryogenic temperatures, below 40 K, the thermal energy is not enough to ionize the impurities and hence the amount of free carrier drops and rapidly becomes very small. It was reasonably expected that the optical absorption of such samples also drops rapidly proportionally to the free carrier concentration. However, we demonstrate in this paper that although the concentration of free carriers drops as expected the optical absorption nearly stays constant throughout a wide temperature range from 300 K down to 5 K.

The measurements are done using two independent techniques based on photodeflection and calorimetry. Using a third technique (based on spectrophotometric measurement) Spitzer and Fan [6] already showed no change in absorption for highly doped silicon wafers from room temperature down to 5 K.

This article is organised as follows: first the two techniques used to measure the optical absorption are explained; second, the experimental setup as well as the silicon samples tested are described and third the experimental results are presented. Finally, the consequences of theses measurements for the ET are derived.

2. Measurement techniques and experimental setups

In this section, the two experimental techniques used to derive the optical absorption of bulk silicon are presented. The two techniques applied in this paper—the mirage effect and the

heating of the sample by light—are sensitive enough to measure the absorption of moderately doped bulk silicon, the expected material of the ET cryogenic mirror. For samples with higher optical absorption (larger than 0.1 cm^{-1}), a direct measurement of the transmission is enough to derive the absorption [6].

After the measurement principles are summarized, the experimental setups as well as the silicon samples which have been measured are explained in detail.

2.1. The photothermal deflection technique

The photodeflection technique based on the mirage effect is one of the most sensitive methods to measure low optical absorption in materials [7]. Using this very same technique, it has already been shown that pure silicon can present an absorption as low as 5 ppm cm^{-1} at room temperature [5].

The typical setup of a photodeflection bench is composed of two lasers: one high power laser called the pump laser and one low power laser, the probe laser. The pump laser is focused on the material and so is partially absorbed within the sample. The absorbed optical power, converted to heat creates a gradient of temperature. The gradient of temperature induces a gradient of refractive index via the thermo-optic coefficient. The probe beam is aligned to intersect the pump beam in the sample and is then deflected by the gradient of refractive index. The deviation of the probe beam is read out by a quadrant photodetector and is directly proportional to the amount of power absorbed in the sample and hence to the optical absorption.

In order to increase the signal-to-noise-ratio of the deviation method, the pump beam is intensity modulated and the deviation is then detected by a lock-in amplifier. The calibration which links the deviation amplitude to the optical absorption is performed with a sample with a high optical absorption that was directly measured by a spectrophotometer.

2.2. Calorimetric measurement

A calorimetric measurement technique determines the temperature increase of a sample under illumination by a laser of wavelength under study [8]. The temperature increase is directly linked to the optical absorption if the heat capacity of the setup as well as all thermal losses are known. Calorimetric techniques using lasers as a light source are routine techniques allowing the measurement of absorptions below 1 ppm cm^{-1} for high purity optical elements or fiber materials [9, 10].

A laser beam is passed through a sample and a temperature sensor is measuring the increase in temperature under illumination. Care must be taken to avoid any scattered light to hit the sensor directly. This method probes the integral optical absorption of the sample—both possible surface absorption as well as intrinsic bulk absorption. By changing the length of the sample it is possible to disentangle these effects.

In order to reduce extrinsic surface absorption effects great care was taken to clean the samples. A sophisticated cleaning technique available from the semiconductor industry was used and described in section 3.1.

The calorimetric technique becomes especially very sensitive at cryogenic temperatures as the heat capacity of the samples rapidly drops below 50 K following Debye's law ($\propto T^3$).

2.3. Description of the setup at LMA

The photodeflection bench used for the measurement presented in this article is composed of a 30 W pump laser at a wavelength of 1550 nm which is the same wavelength planned for ET

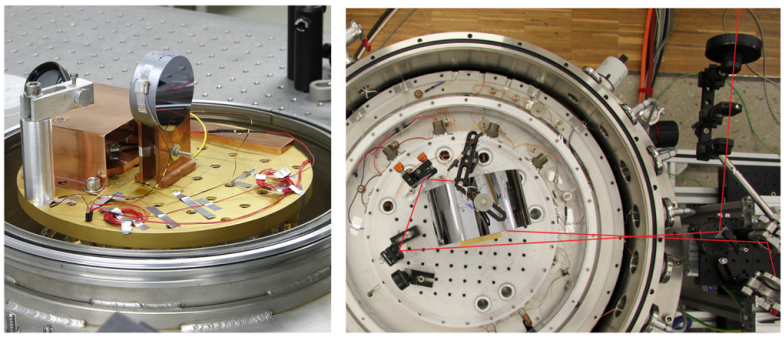

(a) (b)

Figure 1. Photography of the silicon samples in the cryostats at LMA (a) and at the FSU Jena (b). See the text for additional details.

and a 1 mW probe laser at 1310 nm. The wavelength of the probe beam is selected to be in the transparency region of the silicon and close enough to 1550 nm to ensure a similar thermo-refractive coefficient [11]. The pump beam is focused in the silicon sample with a measured waist radius of 0.7 mm (measured with the knife edge technique at the position of the sample) resulting in power densities of maximum 4 kW cm^{-2}.

The tested silicon sample is located in a continuous flow cryostat linked to a liquid helium reservoir. The cooling from room temperature to 10 K is achieved within 24 hours with the sample mounted to a 20 cm diameter cryogenic breadboard via a holder made of copper. A calibrated temperature sensor (Cernox-1070-BO) is directly attached to the sample to continuously record the temperature of the silicon substrate, as shown in figure 1(a). Several optical glass windows with a diameter of 2 inches have been installed to ensure the correct injection and extraction of the pump and probe laser beams. Further details on the cryostat performance can be found in a previous article [12].

For the LMA cryogenic run described in this article, the tested silicon sample has a diameter of two inches and is 20 mm long. The sample is doped with boron atoms, giving an averaged resistivity of 2.4 Ω cm (concentration of boron atoms of 5.7×10^{15} cm^{-3}). The optical absorption at room temperature due to the free carriers was measured to be 0.029 cm^{-1} at 1550 nm.

2.4. Description of the setup at the FSU Jena

The setup at the FSU Jena consists of a 5 W CW 1550 nm fiber laser system (NKT Photonics Koheras Adjustic seed laser and Boostik HPA amplifier) and a custom-made bath cryostat [13] for measurements between room temperature and 5 K. The laser beam has a measured waist radius of 0.9 mm inside the sample resulting in a power density of 0.4 kW cm^{-2}. The sample under investigation is a float zone 100 Ω cm silicon single crystal having a diameter of 150 mm and a thickness of 86 mm as shown in figure 1(a). The concentration of boron atoms is about 1×10^{14}cm^{-3}.

A temperature sensor (Cernox CX1070-SD) is directly attached to the sample by means of varnish (VGE 7031). Additionally, an electrical heater is attached to the sample for calibration purposes. Using such a heater avoids the need of a careful treatment of heat losses

in the setup. Applying an electric heating power of 1 mW results in the same heating as is caused by 1 mW of absorbed optical power—independent of all heat losses through the mount, wires or even radiation. These heat losses are kept small by avoiding too much heating of the sample as all heat losses are driven by temperature differences. Typically, no temperature difference larger than 100 mK was used in the experiments.

The sample is mounted inside the cryostat and a weak thermal link is established between the sample and the cold plate. For initial cooling He gas can be applied to the probe chamber allowing an efficient and fast cooling of the sample. The laser beam is aligned in a way that the sample is illuminated under the Brewster angle to avoid unwanted reflections. By means of a set of mirrors the laser beam is then aligned in a way that it leaves the cryostat through the same window as it enters. This technique is needed as the cryostat is only equipped with one window.

3. Experimental investigations

The optical absorption measured at low temperature is summarized in the following sections and compared to the values found at room temperature.

3.1. Investigation of a possible surface absorption

Optical absorption measurements done before on a monolithic cavity [14] reported a high surface absorption. Also, the calorimetric measurements will be extremely sensitive to such absorptions—either being caused by intrinsic surface effects or simply dirt on the surface. Thus, a special run was initially carried on to check the cleaning procedure used for the samples. All samples have been cleaned using a hot mixture of sulfuric acid (96%) and hydrogen peroxide (35%). This mixture does not attack silicon but efficiently removes all organic contamination from the surface. After this cleaning process all samples are given a methanol rinse using ultra pure solvents.

As the surface is the potential origin of unwanted absorption thin wafers have been used for testing surface effects. These wafers are made from high purity material (typically between 10–100 kΩ cm) whose intrinsic absorption is expected to be below 4 ppm cm^{-1} [5]. Such samples have been used to refine the cleaning procedure. A minimum average absorption over at least ten subsequent runs of (12 $\pm$ 9) ppm has been observed. As all absorption values reported in this paper are well above 100 ppm cm^{-1} any influence of the surface to our measurements can be excluded. Additionally, these results make the hypothesis of potential intrinsic strong surface absorptions in silicon very unlikely [14].

3.2. Freeze-out of free carriers

As the optical absorption of silicon is dominated by free carrier absorption at room temperature, it is an interesting step to investigate the change of free carriers during cooling. In order to do so, a moderately doped silicon wafer sample (1–10 Ωcm, p-type boron-doped) was contacted in a four point geometry as shown in figure 2. Four aluminium pads were evaporated onto the surface of the sample forming electronic contacts. Low contact resistivity Ohmic contacts have been achived by a careful annealing of the sample. The four contact pads have been attached to wires of a cryogenic probe station by means of indium. The two outer contacts have then be used to feed a constant current through the sample while the inner contacts have been used to measure the voltage created by the current. An Agilent B2901A SMU has been used to apply the current and measure the voltage. The finite geometry of the

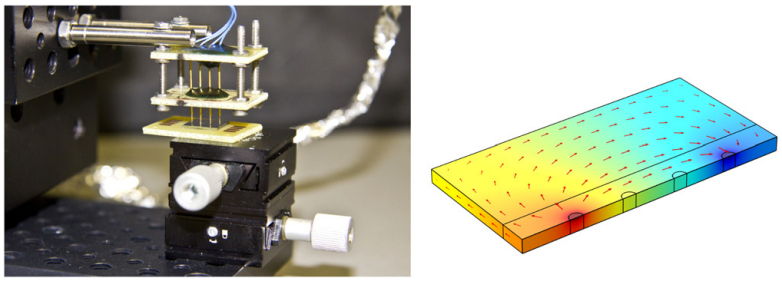

(a) (b)

Figure 2. (a) 4-probe-setup for measuring the resistance of the silicon sample. (b) Distribution of the electrical potential within the sample to include boundary effects of the finite sized sample using COMSOL.

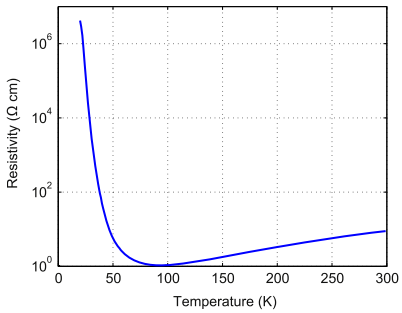

Figure 3. Measured values of the resistivity of the silicon sample (1–10 Ω cm, boron doped) under investigation in a wide temperature range from 5 K to 300 K.

sample in use (typically 10 mm ×10 mm) has been taken into account numerically by means of a FEA using COMSOL .

Figure 3 shows the results obtained from a voltage-current-measurement over a wide range of temperatures from 5 K to 300 K. It can be seen that the resistivity starts at around 8 Ω cm at room temperature, decreases to about 1 Ω cm at 80 K and then steeply rises to more than 10 MΩ cm at cryogenic temperatures. Here, the measurement is limited by the finite input resistance of the pre-amplifier in use.

The resistivity ρ of a semiconductor is given by [15]

$$\rho = \frac{1}{-en\mu_n + ep\mu_p} \tag{1}$$

with the mobility of the electrons μ_n and the holes μ_p and the density of electrons n and holes p. In the case studied here holes are mainly carrying the current (as the sample is p-doped). Thus, the concentration of electrons can be approximated to be zero. The observed behaviour of the resistivity by changing the temperature cannot be described by the temperature dependence of the mobility μ_p (see e. g. [16]) thus the change in hole concentration is the only

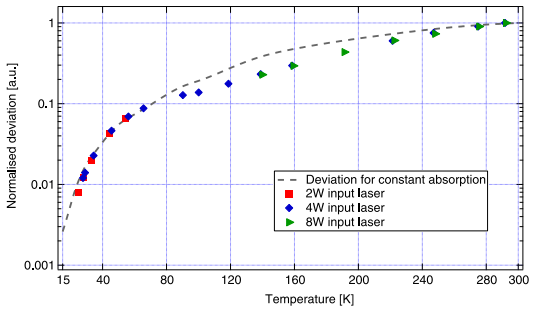

Figure 4. Normalized deviation of the probe beam as a function of the temperature for the photodeflection bench. The dashed curve represents the expected theoretical deviation if the optical absorption is constant with the temperature.

explanation for the measured trend presented in figure 3. The concentration of free carriers is therefore strongly reduced by cooling below 50 K.

3.3. Bulk absorption measurement at LMA

The photodeflection technique presented in section 2.1 has been very successful at room temperature however it remains an indirect measurement where physical parameters of the substrate play an important role. For example, the deviation of the probe beam is different for two samples presenting the same optical absorption if they have different thermal conductivities or thermo-refractive coefficient.

The same phenomenon happens when the temperature of the silicon sample changes. The measured deviation will change not only because of a possible change in the absorption but also since the specific heat, the thermal conductivity and the thermo-refractive coefficient depend on temperature. We can already predict that the deviation signal for a constant optical absorption will decrease with temperature as the thermooptic coefficient decreases and the thermal conductivity increases for silicon substrate.

More precisely, for silicon the thermo-refractive coefficient will decrease by a factor 100 from room temperature to 20 K [17], hence reducing the gradient of refractive index responsible for the deviation of the probe beam. That would be the major effect, the change in thermal conductivity [18] and specific heat having a smaller effect [19]. That statement is valid for our setup and dependent on the modulation frequency of the pump beam as well as the size of the pump laser beam. So we already expect that the deviation signal will decrease by a factor 100 between room temperature and cryogenic temperature if the absorption is constant. So, for this reason, we tested a sample with relatively high optical absorption ($0.029\,\mathrm{cm}^{-1}$) in order to have large enough deviation signal from 300 K to 10 K (the SNR of the deviation signal is around 2×10^3 at room temperature).

The theoretically predicted deviation signal as a function of temperature is shown as the dashed line in figure 4, and assuming a constant absorption for the silicon sample. On that figure, the deviation is normalized to be 1 at room temperature. The measured deviation, also normalized to the value at room temperature, is also added to the figure.

The deviation has been measured at different pump powers to rule out nonlinear effects. Also near room temperature, high pump power is used to generate a noticeable rise in the

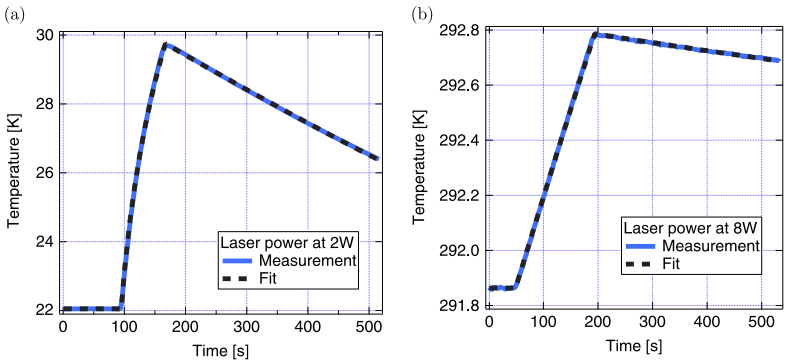

Figure 5. Example of a temperature rise at cryogenic temperature (a) and room temperature (b) when the pump laser is switched on for few minutes. For the left plot, the pump (heating) laser is switched on at 94 s and switched off at 164 s and for the right plot the times are respectively 48 s and 193 s. The laser power is set to 2 W at cryogenic temperature but to 8 W at room temperature in order to create a noticeable temperature rise.

temperature of the sample in order to still derive the absorption also from calorimetric measurement. The deviation measurement were also normalized with the pump power to compare all the data points to the same theoretical curve.

At low temperature, below 50 K, we can notice from graph 4 that the measured deviation matches the theoretical deviation from constant absorption within 20%. This result indicates that the optical absorption is the same at room temperature and low temperature for bulk silicon.

At the same time as the measurement is done with the photodeflection technique, the temperature of the sample is monitored. In that way, the heating due to the pump laser beam is recorded. Such a plot of the temperature evolution is shown in the left part of the figure 5.

To derive the heating power from the temperature rise a fit is performed. The fitting function is given by solving the heat equation in the simple case of assuming an isothermal behaviour of the sample. This assumption is valid for silicon since the thermal conductivity is very high in the temperature range under investigation (with the thermal conductivity being always larger than 150 W (m K)$^{-1}$). Such fits are presented in figure 5. The fit is remarkably good, considering the simplicity of the model and that only two parameters are fitted: the absorbed optical power and the heat lost by conduction through the mount of the sample.

From the fit, at low temperature (22 K), the heating power absorbed by the sample is found to be 0.11 W for an input laser of 2 W, giving an optical absorption of 0.030 cm^{-1}. At room temperature we found an absorbed power of 0.44 W for an input power of 8 W which gives the same absorption as at low temperature. The uncertainty on such measurement is within five percent coming from the uncertainty on the specific heat (especially at low temperature) and on the measured laser power. The measured absorption at room temperature derived from the calorimetric measurement is within 2% of the value found by spectroscopic measurement.

The results from the calorimetric measurement suggest that no decrease (nor increase) in the optical absorption of silicon should be expected by cooling the substrate from room

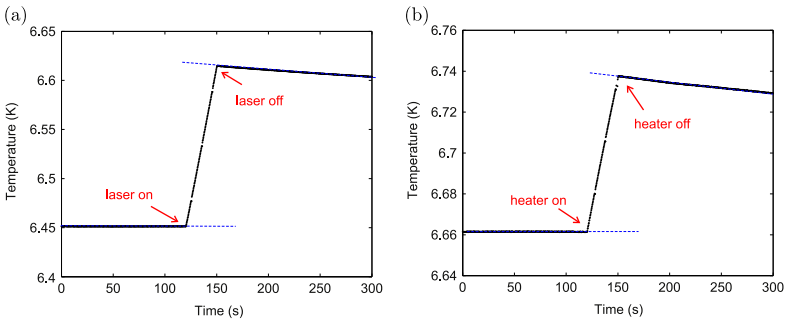

Figure 6. Example for a calorimetric measurement run. The sample is heated by a laser (a) and by an electrical heater (b). The electric heating is used for calibration purposes. The laser power was 0.26 W and the electrical heater power 0.73 mW. In both curves the heating time was 30 s.

temperature to 20 K. That is the same conclusion as the measurement based on the photo-deflection technique.

3.4. Bulk absorption measurement at the FSU Jena

Figure 6 represents a typical set of measured values at cryogenic temperatures. The temperature of the sample is first stabilized and recorded for a given time of a few minutes. Then the laser illuminates the sample for a certain time interval with a certain laser power. Illumination time and laser power are adjusted in a way that the resulting temperature increase can be easily measured and is not too large. Under this assumption the thermal properties of the sample can be assumed to be constant. Typical temperature differences of a few 10 mK are used. After the thermal equilibrium is reached again an electrical heater is used to measure the temperature increase for a given electrical heating power. The power is roughly adjusted to give a similar temperature increase during this period. This method allows to eliminate unknown parasitic heat fluxes to the surroundings.

Heating the sample over a time Δt with a power P results in a temperature increase ΔT of

$$P\Delta t = C\Delta T \tag{2}$$

with C being the net heat capacity of the sample. This is independent whether the power is delivered by a laser or an electrical heater. Using the subscript L for laser and H for heater allows the substitution of the unknown heat capacity C. The absorbed laser power P_L is then given by

$$P_L = \frac{\Delta T_L}{\Delta T_H}\frac{\Delta t_H}{\Delta t_L}P_H. \tag{3}$$

All input parameters can be easily measured assuming that the heat capacity is the same during laser illumination and electrical heating. Under the experimental constraints used in this study this is always fulfilled.

The absorbed laser power P_L is linked to the illuminating laser power P_0, the absorption coefficient α and the optical path of the laser beam inside the sample L by means of

$$P_L = P_0 e^{-\alpha L}. \tag{4}$$

Equations (3) and (4) are used to determine the optical absorption α. The measurement of the 150 mm bulk sample shows the same absorption at room temperature and at 6 K, which is 780 ppm/cm. An independent cross-check using the photodeflection technique at LMA revealed a similar value for the room temperature value. Thus, also this second sample exhibiting a reduced concentration of dopants shows similar absorption values at 300 K and 6 K. This independently confirms the findings on the sample previously discussed in section 3.3 and suggests that the obtained behaviour might be inherent to silicon.

The measurement has been repeated at least ten times at the different temperatures resulting in a typical statistical fluctuation of 10% at room temperature and 1% at cryogenic temperatures. The higher accuracy at low temperatures is based on the larger temperature difference that needs to be measured due to the smaller heat capacity. Further including the inaccuracy of the laser power sensors as well as of the heater power results in a total relative error of 20% at room temperature and 10% at cryogenic temperatures.

4. Consequences for ET

To derive the numbers presented in this section, several parameters of the ET have to be taken into account. Relevant parameters are taken from the ET conceptual design study [20] and are presented below.

The circulating power in the core interferometer is expected to be 65 W (measured on the recycling mirror) and the power circulating in the arm cavity is 18 kW, that is also the power incident to the high reflectivity coating of the input mirror.

The silicon mirror has a cylindrical shape with a diameter of 50 cm and a thickness of 46 cm. The operating temperature is assumed to be 10 K and at the time of writing the design study the absorbed power was estimated to be 20 mW.

Potentially, Czochralski grown silicon having a resistivity between 500 Ω cm and 1000 Ω cm will be available in large enough pieces for optics that can be used in ET-LF [21]. Here, silicon single crystals with a diameter of 50 cm and thicknesses of about 50 cm are needed. Higher purities (and hence nominally low absorptions [5]) can be obtained by means of the float zone technique—however, it is not expected that it can be produced in such large pieces within the next years as currently a technical limitation in size to about 200–250 mm exists.

As we have shown in this article, the optical absorption at cryogenic temperatures is roughly the same as at room temperature. Thus, silicon of the purity discussed here will have an absorption of about 300 ppm cm^{-1} throughout the whole temperature range from 300 K down to 5 K [5]. This assumption is already conservative accounting for a safety margin in the following estimates.

The most crucial mirror affected by optical absorption is the input test mass of the arm cavities of ET-LF. Here, a laser beam of approximately 65 W will pass through the whole material made of silicon. The total absorption is then given by

$$P_{\mathrm{abs}} = \alpha \times L \times P_0 \tag{5}$$

with the absorption coefficient α, the length of the substrate L and the laser power P_0. Using the above values, the total absorbed power within the silicon material is around 1 W. This heat needs to be removed by the suspension elements being planned to be fabricated by highly conductive silicon material.

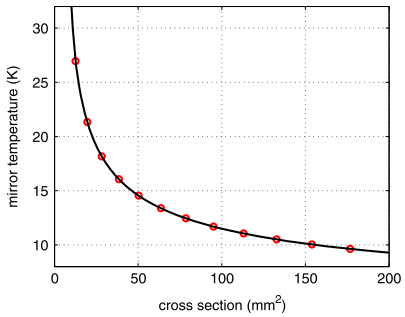

Figure 7. Equilibrium temperatures in the input test mass assuming a realistic optical absorption as well as a temperature dependent thermal conductivity for silicon. The temperature at the cold end of the fiber was assumed to be 4 K, the lengths of the fiber is set to 1 m.

Assuming a suspension length of 1 m, the equilibrium temperature of the mirror was calculated using an FEA model in COMSOL. Here, the temperature dependence of the thermal conductivity of silicon as well as its size dependence was accounted for. As a simplification a single suspension fiber was assumed—a simple scaling using the real number and length of the fiber can be done easily. Figure 7 summarizes the results.

It can be directly seen that the expected operational temperature of 10 K at the test mass for ET-LF is only possible with a total cross section of more than 150 mm^2. This might result in a very stiff suspension showing bad thermal noise performance [22]. Thus, a higher operational temperature for the ET-LF mirrors is preferred which is also compatible with the tolerable mirror thermal noise level. At around 20 K a total cross section of about 25 mm^2 is needed which can be provided by four suspension wires or ribbons.

A further reduction of the temperature of the cold end does not give any benefits for the heat extraction as the thermal conductivity of silicon is small between 2 K and 4 K. This does not lead to a better cooling performance. However, using LHe in the superfluid state might result in a dramatic reduction of mechanical disturbances and could be appealing for the overall performance.

In parallel to the development of suitable cryogenic suspension, research on silicon substrates will continue with the aim to find the silicon with the lowest possible absorption at low temperature and available in sizes required for ET.

The larger thermal absorption in the bulk material relaxes the constraints on the coating absorption significantly. Considering the laser power of 18 kW in the interferometer arm cavities and assuming that the coating is allowed to absorb a tenth of power absorbed in the substrate (i. e. 0.1 W), a maximum coating absorption of 5 ppm (≈0.1 W/18 kW) can be tolerated. A higher tolerable coating absorption has some important consequences since it opens the possibility to coating technology different from the usual alternative layers of fused silica/tantala [23]. More specifically, crystalline coating [24] or hafnia layers [25] to replace tantala may be acceptable.

5. Conclusion

Based on independent measurements on two silicon samples, we have shown that no significant modification in the optical absorption at 1550 nm of bulk crystalline silicon must be expected by cooling the substrate from room temperature to cryogenic temperature. This result is in contradiction to what was assumed for the cryogenic silicon mirrors of the ET, since it was thought that the free carrier freezeout happening at low temperature will guarantee a negligible optical absorption. Further, no significant surface absorption has been observed during our measurement.

Our conclusion implies that a relatively large amount of heat will have to be extracted from the cryogenic mirrors in order to keep the desired temperature of the interferometer if the current silicon absorption cannot be lowered. As a result, in the current design of the suspension the cross section of the fiber holding the mirrors must be significantly increased with the risk of increasing the thermal noise. Further detailed studies are needed to optimise the shape, material selection as well as the optimum operational temperature.

If the heat absorbed within the mirror substrate is relatively high, the constraints on the other potential sources of heat occurring in the mirrors can be relaxed. In particular, the coating absorption could be as high as 5 ppm and more heat from radiation could be tolerated from the room temperature vacuum enclosure.

According to our tests for all practical purposes the absorption can be considered constant between room temperature and low temperature. So, in order to select the suitable silicon quality for the ET mirrors, a measuring campaign for the optical absorption at room temperature is likely to be sufficient without the need of expensive cryogenic runs. Of course, once a particular quality of silicon has been selected, a confirmation of the absorption at low temperature will still be required.

The measured absorption at low temperature is so far unexplained by any theory known by the authors. Research to understand why the absorption is only marginally dependent on the temperature is ongoing.

Acknowledgements

The authors from LMA gratefully acknowledge the support of the European Gravitational Observatory (EGO) and the LABEX Lyon Institute of Origins (ANR-10-LABX-0066) of the Universit de Lyon for its financial support within the program Investissements dAvenir (ANR-11-IDEX-0007) of the French government operated by the National Research Agency (ANR). The support of the German Science Foundation DFG is acknowledged under contract SFB TR7. The EU supports this activity under the APPEC grant ET R&D.

References

[1] Punturo M *et al* 2010 The Einstein telescope: a third-generation gravitational wave observatory *Class. Quantum Grav.* **27** 194002
[2] Losurdo G 2012 Ground-based gravitational wave interferometric detectors of the first and second generation: an overview *Class. Quantum Grav.* **29** 124005
[3] Tomaru T *et al* 2002 Maximum heat transfer along a sapphire suspension fiber for a cryogenic interferometric gravitational wave detector *Phys. Lett.* A **301** 215–9
[4] Soref R A and Bennett B R 1987 Electrooptical effects in silicon *IEEE J. Quantum Electron.* **23** 123–9

[5] Degallaix J *et al* 2013 Bulk optical absorption of high resistivity silicon at 1550 nm *Opt. Lett.* **38** 2047–9

[6] Spitzer W and Fan H Y 1957 Infrared absorption in n-type silicon *Phys. Rev.* **108** 268–71

[7] Jackson W B, Amer N M, Boccara A C and Fournier D 1981 Photothermal deflection spectroscopy and detection *Appl. Opt.* **20** 1333–44

[8] Tomaru T *et al* 2001 Cryogenic measurement of the optical absorption coefficient in sapphire crystals at 1.064 μm for the large-scale cryogenic gravitational wave telescope *Phys. Lett.* A **283** 80–84

[9] Willamowski U, Ristau D and Welsch E 1998 Measuring the Absolute Absorptance of Optical Laser Components *Appl. Opt.* **37** 8362–70

[10] Stone F T, Gardner W B and Lovelace C R 1978 Calorimetric measurement of absorption and scattering losses in optical fibers *Opt. Lett.* **2** 48–50

[11] Frey B J, Leviton D B and Madison T J 2006 Temperature-dependent refractive index of silicon and germanium *Astron. Telesc. Instrum. Int. Soc. Opt. Photonics* 62732J

[12] Degallaix J *et al* 2012 The new cryogenic facility at LMA *J. Phys.: Conf. Ser.* **363** 012008

[13] Nawrodt R, Zimmer A, Nietzsche S, Thürk M, Vodel W and Seidel P 2006 A new apparatus for mechanical Q-factor measurements between 5 and 300 K *Cryogenics* **46** 718–23

[14] Khalaidovski A, Steinlechner J and Schnabel R 2013 Indication for dominating surface absorption in crystalline silicon test masses at 1550 nm *Class. Quantum Grav.* **30** 165001

[15] Grundmann M 2010 *The Physics of Semiconductors: An Introduction Including Nanophysics and Applications* (*Graduate Texts in Physics*) (Berlin: Springer)

[16] Jacoboni C, Canali C, Ottaviani G and Quaranta A A 1977 A review of some charge transport properties of silicon *Solid-State Electron.* **20** 77–89

[17] Komma J, Schwarz C, Hofmann G, Heinert D and Nawrodt R 2012 Thermo-optic coefficient of silicon at 1550 nm and cryogenic temperatures *Appl. Phys. Lett.* **101** 041905

[18] Thompson J C and Younglove B A 1961 Thermal conductivity of silicon at low temperatures *J. Phys. Chem. Solids* **20** 146–9

[19] Flubacher P, Leadbetter A J and Morrison J A 1959 The heat capacity of pure silicon and germanium and properties of their vibrational frequency spectra *Phil. Mag.* **4** 273–94

[20] ET science team 2012 *Einstein Gravitational Wave Telescope Conceptual Design Study* code: ET-0106C-10 (https://tds.ego-gw.it/ql/?c=7954)

[21] Nishi Y and Doering R 2012 *Handbook of Semiconductor Manufacturing Technology* 2nd edn (Boca Raton, FL: CRC Press)

[22] Cumming A V *et al* 2014 Silicon mirror suspensions for gravitational wave detectors *Class. Quantum Grav.* **31** 025017

[23] Harry G M *et al* 2007 Titania-doped tantala/silica coatings for gravitational-wave detection *Class. Quantum Grav.* **24** 405

[24] Cole G D, Zhang W, Martin M J, Ye J and Aspelmeyer M 2013 Tenfold reduction of Brownian noise in high-reflectivity optical coatings *Nat. Photonics* **7** 644–50

[25] Abernathy M R *et al* 2011 Cryogenic mechanical loss measurements of heat-treated hafnium dioxide *Class. Quantum Grav.* **28** 195017

Realistic loss estimation due to the mirror surfaces in a 10 meters-long high finesse Fabry-Perot filter-cavity

Nicolas Straniero,[1,*] Jérôme Degallaix,[1] Raffaele Flaminio,[2] Laurent Pinard[1] and Gianpietro Cagnoli[1]

[1]*Laboratoire des Matériaux Avancés, CNRS-IN2P3, Université de Lyon, Villeurbanne, France*
[2]*National Astronomical Observatory of Japan, 2-21-1 Osawa, Mitaka, Tokyo, 181-8588, Japan*
**n.straniero@lma.in2p3.fr*

Abstract: In order to benefit over the entire frequency range from the injection of squeezed vacuum light at the output of laser gravitational wave detectors, a small bandwidth high finesse cavity is required. In this paper, we investigate the light losses due to the flatness and the roughness of realistic mirrors in a 10 meters-long Fabry-Perot filter cavity. Using measurements of commercial super-polished mirrors, we were able to estimate the cavity round trip losses separating the loss contribution from low and high spatial frequencies. By careful tuning of the cavity g-factor and the incident position of the light on the mirrors, round trip losses due to imperfect mirror surfaces as low as 3 ppm can be achieved in the simulations.

OCIS codes: (230.4040) Mirrors; (220.5450) Polishing; (050.2230) Fabry-Perot; (220.2740) Geometric optical design.

References and links

1. F. Acernese, M. Agathos, K. Agatsuma, D. Aisa, N. Allemandou, A. Allocca, J. Amarni, P. Astone, G. Balestri, G. Ballardin, F. Barone, J.-P. Baronick, M. Barsuglia, A. Basti, F. Basti, T. S. Bauer, V. Bavigadda, M. Bejger, M. G. Beker, C. Belczynski, D. Bersanetti, A. Bertolini, M. Bitossi, M. A. Bizouard, S. Bloemen, M. Blom, M. Boer, G. Bogaert, D. Bondi, F. Bondu, L. Bonelli, R. Bonnand, V. Boschi, L. Bosi, T. Bouedo, C. Bradaschia, M. Branchesi, T. Briant, A. Brillet, V. Brisson, T. Bulik, H. J. Bulten, D. Buskulic, C. Buy, G. Cagnoli, E. Calloni, C. Campeggi, B. Canuel, F. Carbognani, F. Cavalier, R. Cavalieri, G. Cella, E. Cesarini, E. C. Mottin, A. Chincarini, A. Chiummo, S. Chua, F. Cleva, E. Coccia, P.-F. Cohadon, A. Colla, M. Colombini, A. Conte, J.-P. Coulon, E. Cuoco, A. Dalmaz, S. D'Antonio, V. Dattilo, M. Davier, R. Day, G. Debreczeni, J. Degallaix, S. Deléglise, W. D. Pozzo, H. Dereli, R. D. Rosa, L. D. Fiore, A. D. Lieto, A. D. Virgilio, M. Doets, V. Dolique, M. Drago, M. Ducrot, G. Endrőczi, V. Fafone, S. Farinon, I. Ferrante, F. Ferrini, F. Fidecaro, I. Fiori, R. Flaminio, J.-D. Fournier, S. Franco, S. Frasca, F. Frasconi, L. Gammaitoni, F. Garufi, M. Gaspard, A. Gatto, G. Gemme, B. Gendre, E. Genin, A. Gennai, S. Ghosh, L. Giacobone, A. Giazotto, R. Gouaty, M. Granata, G. Greco, P. Groot, G. M. Guidi, J. Harms, A. Heidmann, H. Heitmann, P. Hello, G. Hemming, E. Hennes, D. Hofman, P. Jaranowski, R. J. G. Jonker, M. Kasprzack, F. Kéfélian, I. Kowalska, M. Kraan, A. Królak, A. Kutynia, C. Lazzaro, M. Leonardi, N. Leroy, N. Letendre, T. G. F. Li, B. Lieunard, M. Lorenzini, V. Loriette, G. Losurdo, C. Magazzù, E. Majorana, I. Maksimovic, V. Malvezzi, N. Man, V. Mangano, M. Mantovani, F. Marchesoni, F. Marion, J. Marque, F. Martelli, L. Martellini, A. Masserot, D. Meacher, J. Meidam, F. Mezzani, C. Michel, L. Milano, Y. Minenkov, A. Moggi, M. Mohan, M. Montani, N. Morgado, B. Mours, F. Mul, M. F. Nagy, I. Nardecchia, L. Naticchioni, G. Nelemans, I. Neri, M. Neri, F. Nocera, E. Pacaud, C. Palomba, F. Paoletti, A. Paoli, A. Pasqualetti, R. Passaquieti, D. Passuello, M. Perciballi, S. Petit, M. Pichot, F. Piergiovanni, G. Pillant, A. Piluso, L. Pinard, R. Poggiani, M. Prijatelj, G. A. Prodi, M. Punturo, P. Puppo, D. S. Rabeling, I. Rácz, P. Rapagnani, M. Razzano, V. Re, T. Regimbau, F. Ricci, F. Robinet, A. Rocchi, L. Rolland, R. Romano, D. Rosińska, P. Ruggi, E. Saracco, B. Sassolas, F. Schimmel, D. Sentenac, V. Sequino, S. Shah, K. Siellez, N. Straniero, B. Swinkels, M. Tacca, M. Tonelli, F. Travasso, M. Turconi, G. Vajente, N. van Bakel, M. van Beuzekom, J F J. van den Brand, C. Van Den Broeck, M. V. van der Sluys, J. van Heijningen, M. Vasúth, G. Vedovato, J. Veitch, D. Verkindt, F. Vetrano, A. Viceré, J.-Y. Vinet, G. Visser, H. Vocca, R. Ward, M. Was, L.-W. Wei, M. Yvert, A. Z. żny, and J.-P. Zendri, "Advanced Virgo: a second-generation interferometric gravitational wave detector," Class. Quantum Gravity **32**(2), 024001 (2015).

#240769 Received 12 May 2015; revised 30 Jun 2015; accepted 30 Jun 2015; published 7 Aug 2015

2. G. M. Harry, "Advanced LIGO: the next generation of gravitational wave," Class. Quantum Gravity **27**(8), 084006 (2010).
3. K. Somiya, "Detector configuration of KAGRA - the Japanese cryogenic gravitational-wave detector," Class. Quantum Gravity **29**(12), 124007 (2012).
4. C. M. Caves, "Quantum-mechanical noise in an interferometer," Phys. Rev. D Part. Fields **23**(8), 1693–1708 (1981).
5. The LIGO Scientific Collaboration (LSC), "A gravitational wave observatory operating beyond the quantum shot-noise limit," Nat. Phys. **7**, 962 (2011).
6. H. Grote, K. Danzmann, K. L. Dooley, R. Schnabel, J. Slutsky, and H. Vahlbruch, "First long-term application of squeezed states of light in a gravitational-wave observatory," Phys. Rev. Lett. **110**(18), 181101 (2013).
7. The LIGO Scientific Collaboration (LSC), "Enhanced sensitivity of the LIGO gravitational wave detector by using squeezed states of light," Nat. Photonics **7**, 613 (2013).
8. H. J. Kimble, Y. Levin, A. B. Matsko, K. S. Thorne, and S. P. Vyatchanin, "Conversion of conventional gravitational-wave interferometers into quantum nondemolition interferometers by modifying their input and/or output optics," Phys. Rev. D Part. Fields **65**(2), 022002 (2001).
9. J. Harms, Y. Chen, S. Chelkowski, A. Franzen, H. Vahlbruch, K. Danzmann, and R. Schnabel, "Squeezed-input, optical-spring, signal-recycled gravitational-wave detectors," Phys. Rev. D Part. Fields **68**(4), 042001 (2003).
10. M. Evans, L. Barsotti, P. Kwee, J. Harms, and H. Miao, "Realistic filter cavities for advanced gravitational wave detectors," Phys. Rev. D Part. Fields Gravit. Cosmol. **88**(2), 022002 (2013).
11. S. Chelkowski, H. Vahlbruch, B. Hage, A. Franzen, N. Lastzka, K. Danzmann, and R. Schnabel, "Experimental characterization of frequency-dependent squeezed light," Phys. Rev. A **71**(1), 013806 (2005).
12. E. Oelker, T. Isogai, J. Miller, M. Tse, L. Barsotti, N. Mavalvala, and M. Evans, "Audio-band frequency-dependent squeezing via storage of entangled photons, " (in preparation).
13. T. Isogai, J. Miller, P. Kwee, L. Barsotti, and M. Evans, "Loss in long-storage-time optical cavities," Opt. Express **21**(24), 30114–30125 (2013).
14. K. Dupraz, K. Cassou, N. Delerue, P. Fichot, A. Martens, A. Stocchi, A. Variola, F. Zomer, A. Courjaud, E. Mottay, F. Druon, G. Gatti, A. Ghigo, T. Hovsepian, J. Y. Riou, F. Wang, A. C. Mueller, L. Palumbo, L. Serafini, and P. Tomassini, "Design and optimization of a highly efficient optical multipass system for γ-ray beam production from electron laser beam Compton scattering," Phys. Rev. ST Accel. Beams **17**(3), 033501 (2014).
15. A. Cadène, P. Berceau, M. Fouch, E. R. Battesti, and C. Rizzo, "Vacuum magnetic linear birefringence using pulsed fields: status of the BMV experiment," Eur. Phys. J. D **68**(16), 1–7 (2014).
16. J. Degallaix, "OSCAR a Matlab based optical FFT code," in IOP proceedings of Journal of Physics: Conference Series (2010).
17. H. Kogelnik and T. Li, "Laser beams and resonators," Appl. Opt. **5**(10), 1550–1567 (1966).
18. H. Yamamoto, "1D PSD of mirror maps," LIGO Internal Note, LIGO-T1100353-v1 (2011), https://dcc.ligo.org/DocDB/0066/T1100353/T1100353-v1.pdf.
19. J.C. Stover, *Optical Scattering: Measurement and Analysis* (SPIE, 1995).
20. F. Magaña-Sandoval, R. X. Adhikari, V. Frolov, J. Harms, J. Lee, S. Sankar, P. R. Saulson, and J. R. Smith, "Large-angle scattered light measurements for quantum-noise filter cavity design studies," J. Opt. Soc. Am. A **29**(8), 1722–1727 (2012).

1. Introduction

The sensitivity of gravitational wave detectors such as Advanced Virgo, Advanced LIGO and KAGRA will be limited by quantum noise over a large portion of the detector frequency range [1–3]. Above a few hundred hertz quantum noise appears as photon shot noise at the interferometer output port. Below hundred hertz quantum noise appears in the form of radiation pressure noise perturbing the test masses positions. Both can be seen as due to the vacuum fluctuations entering the interferometer from the output port.

The injection of a squeezed vacuum state from the interferometer output port allows changing the amplitude of quantum noise. In particular the injection of a frequency independent squeezed vacuum is equivalent to an increase of the interferometer input power [4]. Shot noise is decreased at the cost of increasing radiation pressure. Such a solution is interesting since it will allow decreasing the input power without decreasing the detector sensitivity. Decreasing the input power allows reducing all the difficulties related to running an interferometer with a high heat load on the mirrors.

The reduction of shot noise of laser interferometer gravitational wave detectors by means of squeezed states of light was demonstrated both at GEO 600 [5,6] and at LIGO Hanford [7].

It is possible to reduce the quantum noise at all frequencies if a frequency dependent squeezed vacuum state is injected into the interferometer from the output port [8,9]. By

#240769 Received 12 May 2015; revised 30 Jun 2015; accepted 30 Jun 2015; published 7 Aug 2015

properly changing the so called squeezing angle as a function of frequency it is possible to decrease both the radiation pressure noise at low frequency and the shot noise at high frequency. The squeezing angle frequency dependence should be such that the squeezing angle is changed at the frequency where the interferometer noise turns from being radiation pressure dominated to being shot noise dominated. According to the design sensitivities of Advanced Virgo, Advanced LIGO and KAGRA such a transition frequency should be around 50 Hz.

The envisaged solution to produce a frequency dependent squeezed vacuum state is to reflect a frequency independent squeezed vacuum state on an optical cavity [8,9]. By keeping the cavity locked off resonance by one cavity half-bandwidth, the squeezing angle of the reflected vacuum squeezed state will change as a function of the frequency. The transition frequency will coincide with the cavity bandwidth. As a consequence the cavity half bandwidth has to be around 50 Hz [10] i.e. its finesse will depend on the cavity length:

For a cavity 10 m long, the cavity finesse has to be about 150000. For a cavity ten times longer (100 m) a lower finesse (15000) would be sufficient.

$$\frac{c/4L}{F} = 50\ Hz \ \Rightarrow\ F = \frac{c/4L}{50} \tag{1}$$

The demonstration of frequency dependent squeezed light was first realized in the megahertz region a decade ago [11]. More recently frequency dependent squeezed light has been demonstrated also in the audio band [12].

The main limitation to the level of squeezing one can achieve are the optical losses in the cavity [13]. The squeezing level of a squeezed state is decreased when passing through a lossy optical element. Losses can be seen as the coherent addition of the squeezed state with an unsqueezed vacuum, thus reducing the squeezing level of the final state. In the case of an optical cavity what matters is relative weight of the cavity round trip losses compared to the cavity input mirror transmission. For a given bandwidth, longer cavities require smaller finesse and thus higher input mirror transmissions. As a consequence the impact of the cavity round trip losses will be smaller for longer cavities so that in the end the important parameter is the round trip loss per cavity unit length (ppm/m). As a consequence the total losses requirements are less stringent for longer cavities.

The need for meter long and very high finesse cavity is not limited to filtering cavities, several other modern optical experiments also requires such cavities, for example for the emission of gamma rays by Compton backscattering [14] or to measure the magnetic birefringence of the vacuum [15].

In the following of this paper we consider the case of a 10 m long cavity since a cavity of this length can be accommodated in present infrastructures such the LIGO and Virgo corner areas and the losses requirements seem still achievable [10]. The goal of this article is to identify the best optical design for such a cavity and to evaluate the round trip losses that one can achieve with present mirror technology. In section 2 we first identify the overall cavity geometry design. Then we describe the flatness and roughness measurements that we made on some commercially available substrates (Sec. 3 and Sec. 4). In section 5 we use the result of the flatness measurement to estimate the losses in the cavity using OSCAR [16], an optical simulation based on FFT field propagation. We study the losses dependence upon several parameters including the surface height RMS, the cavity finesse and the mirrors radius of curvature. Then in section 6 we used the roughness measurements to estimate the additional losses due to high spatial frequencies in the surface profile. Finally in section 7 we discuss the results and then provide some conclusions.

#240769 Received 12 May 2015; revised 30 Jun 2015; accepted 30 Jun 2015; published 7 Aug 2015

10 Aug 2015 | Vol. 23, No. 16 | DOI:10.1364/OE.23.021455 | OPTICS EXPRESS 21457

2. Choice of the mirrors size and mirrors radius of curvature

As the cavity mirrors have a finite size, the first optimization to be done is to find the smallest possible beam size on the mirror in order to limit the clipping loss. To this purpose we choose to have the same radius of curvature (RoC) for the two mirrors.

For a 10 m long cavity the beam diameter is always smaller than 4 mm if both RoC's are below 20 m [17]. The minimum beam size is achieved when the RoC's are equal to 10 m but in that configuration the cavity is degenerated. If we investigate the choice of the best radius of curvature in order to minimize the losses in the cavity and avoid degeneracy, we must also anticipate the polishing specifications and the stress induced by coating. (Here we consider the thermal deformation due to the low power of the laser beam to be negligible). The tolerances due to the manufacturing process of the mirror can add a random offset to the curvature of the mirrors. Moreover experiments done in the lab with low loss IBS coating shows that the coating induces a compression stress on the surface and increases the radius of curvature of the mirror. From those considerations, it is necessary to choose the radius of curvature above and close to 10 meters but far enough from 10 meters in order to avoid the cavity degeneracy. Since the standard specifications of the polisher are typically 1% from the target radius, we will only consider radii of curvature above 11 meters in order to keep a comfortable safety margin inside the requirement of manufacturing, and avoiding the degeneracy. The next simulations in this paper will later help us to choose a more accurate range of radius of curvature in order to minimize the losses in the cavity.

In the following loss investigation, we will focus on the physical uniformity of the substrate and the radius of curvature as specific requirement. We will not consider the other mirror surface misbehavior as the coating uniformity and the coating induced stress. We will just take into account the surface defects and aberrations due to the polishing process, that is to say the flatness and the roughness on the surface of the optics. The flatness derived from the wave-front measurement includes all the low spatial frequencies below 1400 m^{-1}. The roughness measured with an optical profilometer represents the high spatial frequency range around 1000 m^{-1} up to 200 000 m^{-1}. So, in this article, the flatness will quantify the deviation from the nominal profile with the low spatial frequencies whereas the roughness will quantify the small scale details.

Finally, we will only consider commercial micro-polished mirrors of 1 inch or 2 inches for all roughness and flatness measurements and for all cavity loss simulations. 1 inch as mirror diameter is an appropriated size since it is 6 times greater than the laser beam diameter and the light falling outside the mirror is negligible, less than 0.02 ppm per reflection.

3. Wave-front measurement

In order to estimate the round-trip losses in a 10 meters-long filtering cavity, we measure the mirror surfaces which could potentially be used in such a cavity.

First we measured four micro-polished substrates of 2 inches diameter and one of 1 inch. These measurements will help to compare the micro-polished surface uniformity. Secondly, the wave-front map measurement will be used as mirror surface in the cavity simulation.

All the measured substrates are made in standard fused silica and have the same specifications. The flat mirrors are super-polished and the manufacturers announced surface roughness better than 1 Angstrom and also a flatness quality better than $\lambda/10$ (peak-to-valley) at 633 nm of wavelength. The 2 inches mirrors are 10 mm thick versus 6 mm for the 1 inch mirror.

The low spatial frequency flatness of the substrates is measured with a Fizeau Phase Shifted Interferometer (PSI) illuminated by a laser with a 1064 nm wavelength. The PSI uses a flat reference of 6 inches diameter and has a lateral resolution of 350 micrometers. In order to check the reproducibility error of measurement, optics are measured 3 times, unmounted

#240769 Received 12 May 2015; revised 30 Jun 2015; accepted 30 Jun 2015; published 7 Aug 2015

10 Aug 2015 | Vol. 23, No. 16 | DOI:10.1364/OE.23.021455 | OPTICS EXPRESS 21458

and mounted, between 2 consecutive measurements. Piston and tilt are subtracted from the wave-front measurement. An example of the mirror surface is given in Fig. 1.

In order to characterize the flatness of the optics, we calculate the Root Mean Square of the surface map height. The Root Mean Square (RMS) is defined as following:

$$\sigma_{RMS} = \sqrt{\frac{1}{n}\sum_{i=1}^{n}(h_i - \bar{h})^2} \qquad \text{where} \quad \bar{h} = \frac{1}{n}\sum_{i=1}^{n} h_i \tag{2}$$

where n is the number of elements in the sample (in our case the number of pixel). The h_i values are the height of each i-point of the map.

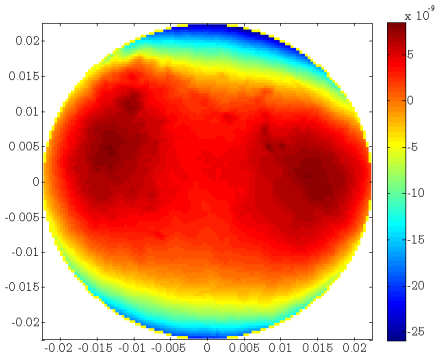

Fig. 1. 2" map flatness measured with the "Phase Shifting Interferometer" over 45mm diameter. The RMS height is 1.3 nm over 23mm of diameter.

Table 1. RMS height measurements of some substrates calculated over different diameters at the center of the substrate.

	Flatness at the center: RMS and PV [nm]							
	45mm diam.		23mm diam.		10mm diam.		4mm diam.	
Mirrors	PV	*RMS*	PV	*RMS*	PV	*RMS*	PV	*RMS*
1 inch substrate 0			39	*9.9*	9.2	*1.8*	5.3	*0.9*
2 inches substrate 0	36	*6.7*	7.6	*1.3*	1.3	*0.3*	0.50	*0.12*
2 inches substrate 1	53	*12*	8.0	*1.3*	2.9	*0.64*	0.60	*0.12*
2 inches substrate 2	42	*9.4*	9.0	*2.0*	2.3	*0.5*	0.77	*0.17*
2 inches substrate 3	47	*10*	9.8	*2.2*	2.1	*0.44*	0.65	*0.14*

: Reference substrate used for the simulations.

We calculate the RMS height of the wave-front measurement in the central part and over different diameters. The RMS of the different mirrors are shown in the Table 1. We see that the RMS flatness is slightly different depending on the substrate and according to the diameter of calculation. A relevant diameter of calculation is the diameter seen by the laser beam. We assume here that it is 4 mm, corresponding to twice the beam radius of the laser on the mirror surface. Concerning the 2 inches measured substrates, the RMS flatness is around 0.125 nm +/–20% according to the sample. While over the full aperture the flatness is only

#240769 Received 12 May 2015; revised 30 Jun 2015; accepted 30 Jun 2015; published 7 Aug 2015

slightly better than the specification, over the central 4 mm diameter all the measured mirror surfaces are well below the specifications of λ/10.

While the 2 inches substrates and the 1 inch substrates have the same specification of λ/10 over the entire surface, we notice that the 2 inches substrates are better in the central part over 10 mm diameter (and also over 23 mm diameter). The 1 inch substrate, highlighted in blue in the Table 1, has the worst RMS flatness substrate over the laser beam size. For the next loss simulations, we always used this measured map, in order to have an upper limit for the RTL.

4. Roughness measurement

In principle, the local roughness of the optics is included in the RMS height calculation in previous Eq. (2). But practically the RMS calculation is always limited by the instrument lateral resolution and not all the spatial frequencies are included. In this section, we consider the "high" spatial frequency uniformity in order to estimate the additional losses in the cavity due to the roughness on the mirror surface.

We measured the high frequency roughness with an optical profilometer provided with a 5X magnification Michelson-type interference objective (The device is called "MicroMap" from the eponymous company which no longer exist). The 5X magnification of the profilometer objective provides a resolution of 2.56 µm by pixel with a field of view of 1mmx1mm. Figure 2 gives us an example of roughness measurement. We always subtract piston, tilt and power on the measurement before to display the map and before to use it for the loss calculation.

For all roughness measurement, we chose a 2" substrate and we scanned an area of 12.2mmx12.2mm, 3 times greater than the laser beam diameter, in order to obtain a sufficient statistic. In total, we needed to measure 225 micro-maps of 400 pixels aside. The set of measurements represents a very extensive sample statistic of roughness on the mirrors. Using Eq. (2), we calculated the RMS roughness value of each map. The results are summarized in the histogram in Fig. 3. For this substrate, the RMS height average is 0.13 nm and then median is around 0.12 nm.

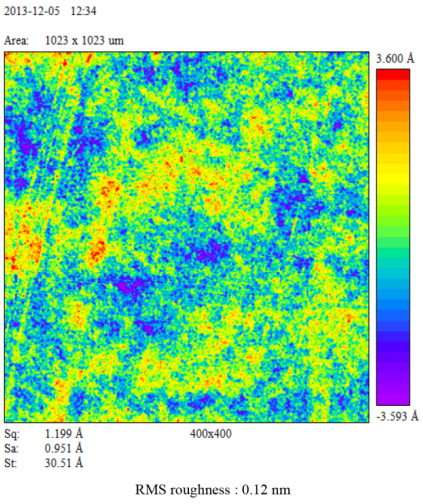

Fig. 2. Example of roughness map measured with the profilometer "Micromap" using a Micheslon-type interference objective 5X magnification, 1mm x 1mm, 2.56 µm/pixel.

#240769 Received 12 May 2015; revised 30 Jun 2015; accepted 30 Jun 2015; published 7 Aug 2015

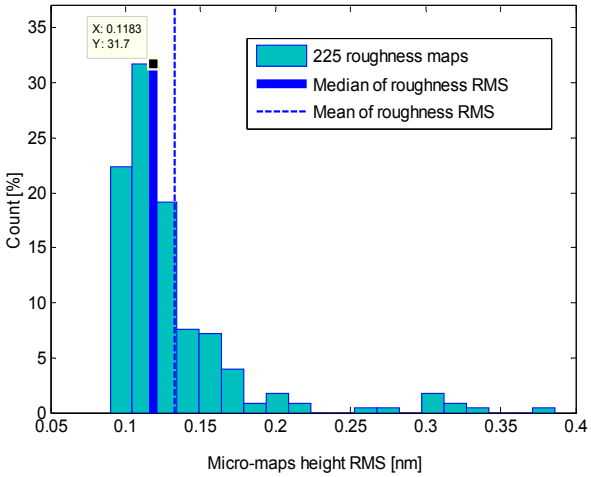

Fig. 3. RMS roughness of 225 micro-maps measured on a micro-polished "Gooch&Housego" optic.

Another way to characterize the surface uniformity of the mirrors is to plot the PSD (Power Spectral Density [18]) of each mirror map. Without entering into the details here we just remind that the PSD of the mirror map is obtained from the two dimensional Fast Fourier Transform of the wave-front map by squaring the 2D FFT and then summing over a ring of constant spatial frequency. The square of the RMS value of the map is equal to the integral of the PSD curve over the spatial frequency band:

$$\sigma_{RMS}^2 = \int_{f1}^{f2} PSD(f).df \tag{3}$$

f_1 is the minimal spatial frequency of the surface on which the uniformity is calculated. The PSD maximal spatial frequency f_2 is exactly one half of the sampling frequency of the measurement, corresponding to the lateral resolution of the instrument. Using the profilometer, the PSD maximal frequency f_2 is equal to 195000 m^{-1} for 2.56 µm of pixel size.

In Fig. 4, we plotted all the PSD of the 225 micro-maps. The PSD are expressed in [nm^2/m^{-1}] but for more contrast concerning the amplitude of the PSD, the color scale and the unit of the color-bar are given as the logarithm of the PSD. By integration of the median of all the PSD, according to Eq. (3), we find 0.11 nm of RMS roughness very similar to the 0.12 nm given by the direct calculation from Eq. (2)

At last, in Fig. 5, we superimpose the median PSD curve of the roughness maps with the PSD curve of the low spatial frequency uniformity. We observe that both PSDs combine in a satisfactory way over four spatial frequency decades.

#240769 Received 12 May 2015; revised 30 Jun 2015; accepted 30 Jun 2015; published 7 Aug 2015

10 Aug 2015 | Vol. 23, No. 16 | DOI:10.1364/OE.23.021455 | OPTICS EXPRESS 21461

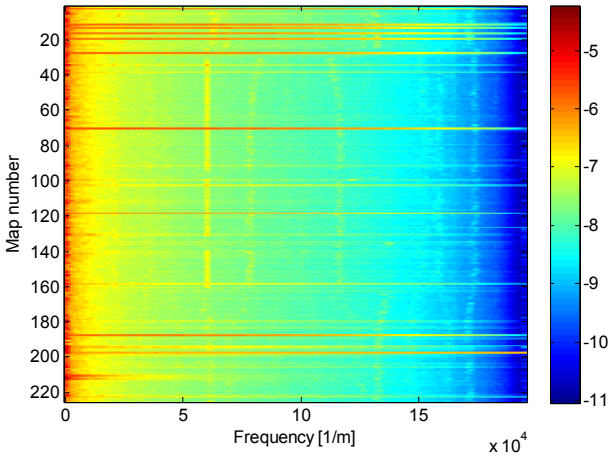

Fig. 4. 2D representation of all the PSD of 225 micro-maps measurements. The color scale is the amplitude of the PSD logarithm.

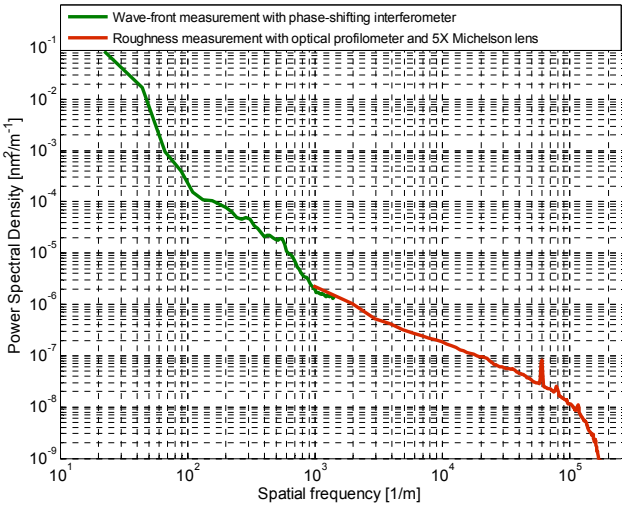

Fig. 5. Power spectral density of the reference substrate of 2 inch diameter.

5. Round-trip loss simulations

5.1. Procedures for the round-trip loss simulations

After description of the substrate surface measurement over a large range of spatial frequencies in previous section, we now detail the use of those maps in the simulations of the Fabry-Perot cavity.

#240769 Received 12 May 2015; revised 30 Jun 2015; accepted 30 Jun 2015; published 7 Aug 2015

10 Aug 2015 | Vol. 23, No. 16 | DOI:10.1364/OE.23.021455 | OPTICS EXPRESS 21462

The simulated cavity is a 10m long Fabry-Perot cavity with two mirrors of one inch diameter. For the numerical simulation, we used the package OSCAR [16] which can simulate cavities or interferometer with any arbitrary distortions. In the simulations, we set the clear aperture of the 1 inch mirror to be 21 mm in diameter to represent the real diameter of the coating. Moreover it cuts off the artifacts on the edge of the measured maps.

Surface maps used in the simulation are polished surface without any coating. However, results at LMA have shown that on small surfaces (less than 50 mm diameter), the coating is uniform enough to not degrade the quality of the polished surface. We also compared PSD before and after coating (with curvature removed) and no significant difference has been found (one more time over 2 inches diameter), the RMS being increased by 0.1 nm after the deposition of a very high reflectivity coating (transmission of 4 ppm).

For all the simulations, the input mirror and the end mirror have the same curvature and we only add the map of the wave-front measurement on the cavity end mirror, the input mirror remains perfect. The end mirror is supposed to be perfectly reflective, and the losses due to the absorption or diffusion from point defect are set to zero.

At first, in order to reduce the calculation time, we simulate a relatively low finesse cavity (finesse of 450, input mirror transmission of 1.4% in power).

For most of the simulations, we use the mirror surface shown in Fig. 6. The 2D height map is added to the nominal curvature of the end mirror with the clear aperture of 21 mm diameter, after have to remove tilt and residual curvature. Since the wave-front measurement resolution is 350µm the map only includes the low spatial frequencies below 1430 m^{-1}.

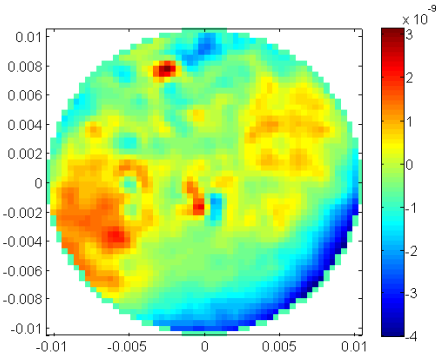

Fig. 6. 1" substrate map of uniformity used in the simulation, as reference map on the cavity end mirror. Tilt and residual curvature were removed over the central 10 mm diameter.

For the simulation of the circulating, transmitted and reflected fields of the cavity, the simulation grid size has been set to 128 by 128 points with the same pixel size as for the surface map to avoid unnecessary resampling.

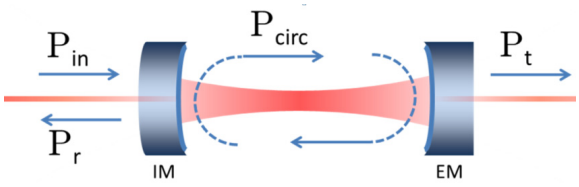

Fig. 7. Simple representation of fields in the simulated Fabry-Perot cavity.

#240769 Received 12 May 2015; revised 30 Jun 2015; accepted 30 Jun 2015; published 7 Aug 2015

10 Aug 2015 | Vol. 23, No. 16 | DOI:10.1364/OE.23.021455 | OPTICS EXPRESS 21463

Using the simple representation of the cavity shown in Fig. 7, the round-trip losses (RTL) in the Fabry-Perot cavity are defined as: (the detailed calculation is presented in the Appendix A:

$$RTL = \frac{P_{in} - P_t - P_r}{P_{circ}} \tag{4}$$

where P_{in}, P_t, P_r and P_{circ} are respectively the input, transmitted, reflected and circulating power of the fields traveling through the cavity.

Equation (4) only takes into account the power inside and leaving the cavity independently of the mode shape. But the part of the reflected and transmitted fields made of higher order modes should be considered as losses, even if they contribute to the total power.

As a consequence, we consider the round-trip losses projected on the TEM_{00} mode using the following Eq. (5):

$$RTL_{00} = \frac{P_{in} - P_r^{00}}{P_{circ}^{00}} \tag{5}$$

with P_r^{00} is the reflected power contained in the TEM_{00} mode of the field of the cavity. The losses on all the modes are usually called the clipping losses due to the finite size of the mirrors. The losses defined on the fundamental mode, takes into account the clipping losses and the fact that the cavity is coupled to an interferometer and that only the light reflected in the fundamental mode will be useful for the rest of the system.

Figure 8 shows the comparison between RTL and RTL_{00} as a function of the nominal radius of curvature (RoC) of the input and end mirrors (waist always in the middle of the cavity). As expected the losses are lower if we consider all the modes as useful power. From now on, for all the simulations, we will consider the round-trip loss calculation on the mode 00 according to Eq. (5).

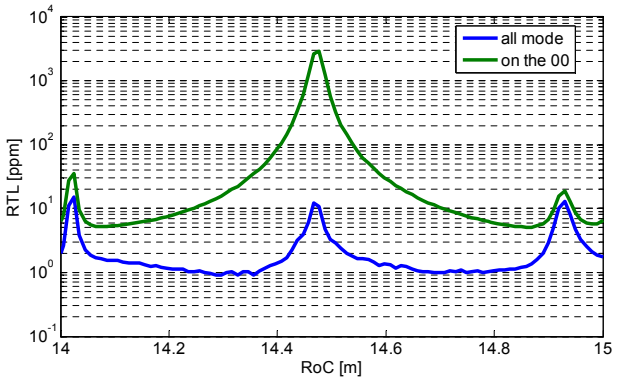

Fig. 8. Comparison of the cavity round-trip losses when all the modes are taken into account or only when the power in the fundamental mode is considered.

In Fig. 8, one can see an excess loss for a radius of curvature of 14.5 m on the losses calculated for the fundamental mode. That is due to one higher order mode resonating at the same time as the fundamental one, the cavity is degenerated for this particular configuration. This higher order mode is rather a low order mode with only moderate excess round trip loss

#240769 Received 12 May 2015; revised 30 Jun 2015; accepted 30 Jun 2015; published 7 Aug 2015

10 Aug 2015 | Vol. 23, No. 16 | DOI:10.1364/OE.23.021455 | OPTICS EXPRESS 21464

(by clipping of its shape outside the mirror), however its presence degrades the purity of the fundamental mode in reflection, hence increasing the RTL_{00}.

5.2. Losses depending on the cavity finesse

If the cavity finesse is increased, the results of the round-trip losses change considerably. Figure 9 shows the RTL_{00} as the mirrors radius of curvature is scanned between 13 and 20 meters for two different finesses 440 and 45000.

For historic reasons, we used a finesse of 45000, instead of 150 000 as mentioned in the introduction. However our finding about the optimal RoC for the cavity is unchanged with the change of finesse. Simulations of losses with finesse of 150 000 were also done with reduced data set and the RTL_{00} when the cavity is not degenerated is 5% lower compared to the value found for a cavity with a finesse of 45 000.

By increasing the cavity finesse, the Airy peaks of the degenerate modes are sharper. As a consequence, the background losses between the peaks decreases significantly. As a consequence we obtain a more comfortable range of radius of curvature for which the losses are minimal and stable.

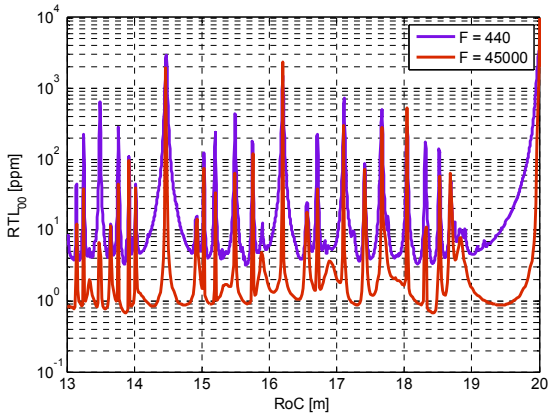

Fig. 9. Round-trip losses in the cavity with radii of curvature of the mirrors between 13 and 20 meters. Comparison of the RTL_{00} according to the cavity finesse.

Now with a second identical mirror as input mirror in the cavity, we checked that the minimal loss could be less than 2 ppm if the cavity finesse is 45000. That is a very good result. However the reader must keep in mind that this result is only due to the flatness of the mirrors because we have been using only a measured map with spatial frequencies above 1430 m^{-1}.

5.3. Dependence of the loss on the RMS height of the mirror surface

From now on and up to the end of the article, the RMS height will be always given without curvature over the diameter of interest. Nevertheless for the 1 inch substrate of the Table 1, we must keep in mind that the RMS height is 0.6 nm without curvature instead of the 1.8 nm with curvature.

We compare now the RTL variation as a function of the local RMS height of the substrate surface used as cavity end mirror. We assume 3 maps where the RMS height varies from 0.3 nm to 2.4 nm. Each map is placed on the end mirror in the cavity simulation and we computed

#240769 Received 12 May 2015; revised 30 Jun 2015; accepted 30 Jun 2015; published 7 Aug 2015

10 Aug 2015 | Vol. 23, No. 16 | DOI:10.1364/OE.23.021455 | OPTICS EXPRESS 21465

the RTL00. The scan of the loss for the 3 maps are plotted in Fig. 10 with a cavity finesse of 45000.

The first simulation uses a one inch substrate. The RMS height without curvature is 0.6 nm over 10 mm of diameter in center. We compare the round-trip losses due to this substrate with the losses generated by 2 other maps. One map is a 2 inches substrate with a lower RMS (0.3 nm) and another higher RMS map (2.4 nm) is the first map multiplied by a factor 4. Without surprise, we observe that the RTL are dependent on the RMS height. For this cavity design, we see that the RTL can increase by almost a factor 10 when the surface RMS increases only by a factor 2. According to the increase of the RMS, a factor of 4 should have been expected in the loss as we will see in the next section. Here we got a larger factor because the RMS calculation was not accurate since it was only taken over a diameter of 10 mm and not taking into account the exact laser beam profile, for example the RMS is 0.26 nm calculated over a 10 mm diameter but only 0.18 nm over 8mm. For Fig. 10, it was difficult to use a beam weighted RMS since the beam size changes as the radius of curvature of the cavity mirrors are scanned.

These results do not include the losses due to the roughness at spatial frequencies above 1400 m^{-1} which will be investigated later.

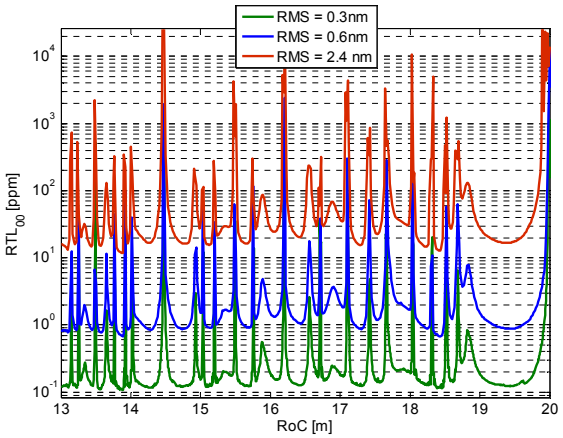

Fig. 10. Round-trip losses in the cavity as a function of the RMS value in the center of the end mirror. The clear aperture is set to a diameter of 21 mm. In the legend, the RMS height of the mirror is given over a diameter of 10 mm.

Having confirmed that the RTL changes as a function of the RMS height, we studied how the value of the local RMS uniformity as seen by the laser beam influences the losses. In other words, how the losses depend on the impact of the laser on the mirror surface.

The central 8mm × 8mm of the mirror surface is shown in Fig. 11. To estimate faithfully the local RMS seen by the laser beam, we weighted the RMS height calculation by the laser beam intensity. The map of the local RMS height as it would be seen by the laser beam is displayed in Fig. 12. The laser beam is shifted by step of 350 µm in order to match the pixel resolution of the wave-front measurement.

#240769 Received 12 May 2015; revised 30 Jun 2015; accepted 30 Jun 2015; published 7 Aug 2015

10 Aug 2015 | Vol. 23, No. 16 | DOI:10.1364/OE.23.021455 | OPTICS EXPRESS 21466

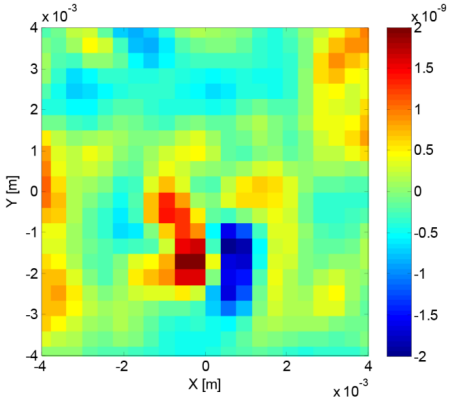

Fig. 11. Flatness map measured with the "Phase Shifting Interferometer" over a square of 8mmx8mm with a resolution of 350µm/ pixel.

For each simulation, we slightly shifted the center of the mirror by an integer number of pixel and calculated the local RMS as well as the cavity losses. A side by side comparison of the local RMS and the local RTL_{00} is shown in Fig. 12. The cavity loss calculations are done on the fundamental mode, for a nominal RoC of 14.1 m and a cavity finesse of 45 000. As expected, we found a good correlation between the local RMS and the round trip losses.

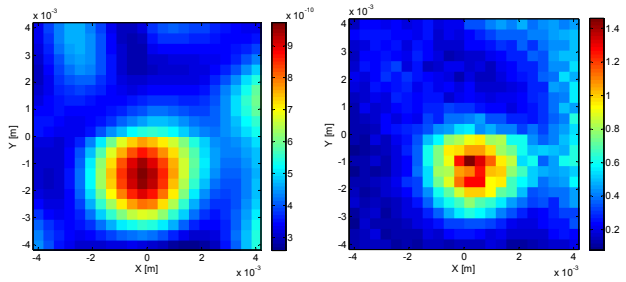

Fig. 12. Comparison on the weighted height RMS in the 8 mm square center of the substrate (a) and the corresponding RTL_{00} depending on the position of the laser beam on the surface (b).

According to the laser position on the mirror, we can gain a factor 2 or 3 on the RMS seen by the laser and almost factor 10 on the round-trip losses in the cavity. In the best configuration we could have only 0.1 ppm of loss by mirror. In Fig. 13, the round trip loss is plotted as a function of the RMS height over the square area of 8 mm x 8 mm at center of the substrate. We noticed that we have around 80% of probability to obtain less than 0.5 nm of RMS flatness, and around 80% of probability to obtain less than 0.5 ppm of loss (1 ppm for two cavity mirrors) with such a super-polished substrate as cavity end mirror.

#240769 Received 12 May 2015; revised 30 Jun 2015; accepted 30 Jun 2015; published 7 Aug 2015

10 Aug 2015 | Vol. 23, No. 16 | DOI:10.1364/OE.23.021455 | OPTICS EXPRESS 21467

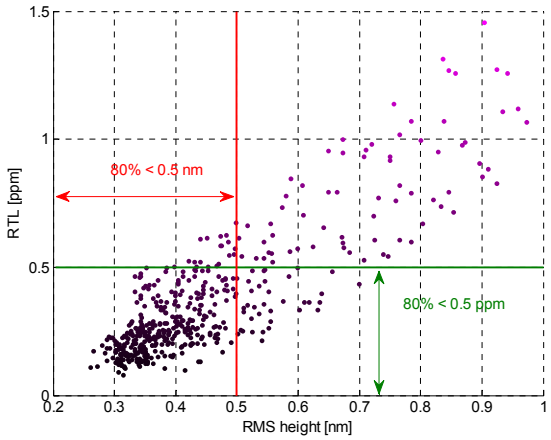

Fig. 13. Round trip loss as a function of the local RMS height seen by the laser beam over a square area of 8mm by 8mm at the substrate center. (The nominal RoC of the entire area is 14.1 meters and no map is placed on the input mirror).

5.4. Losses depending on the local radius of curvature

We saw above that the local RMS changes as a function of the position of the laser beam on the mirror and hence the round trip losses. Assuming that the resonances of the higher order modes are strongly dependent on the mirror radius of curvature, we have also to check if the local curvature in the mirror center could shift significantly the peaks of the resonant modes thus changing the RTL.

The relevant radius of curvature is the radius seen by the laser beam and is depending on the laser beam size for non-perfectly spherical surface. For example, for our cavity, the fundamental mode will only sample the curvature of the mirrors within a diameter of around 4 mm from the center (twice the beam radius). The real curvature ($1/RoC_{real}$) is the combination of the local curvature due to the height non uniformity of flat mirror ($1/RoC_{local}$) with the nominal curvature ($1/RoC_{nominal}$) of a perfectly spherical mirror:

$$\frac{1}{RoC_{real}} = \frac{1}{RoC_{nominal}} + \frac{1}{RoC_{local}} \tag{6}$$

For example if the nominal radius ($RoC_{nominal}$) is 14 m, then the real radius (RoC_{real}) over 4 mm of diameter will locally stay inside 1% requirement only if $|RoC_{local}| > 1400$m. It means that the additional sagitta must be less than 1.5 nm over 4 mm of diameter.

In order to take into account the effect of the random local RoC in the center of the mirrors, we simulated several positions of the laser falling on the mirror surface. Like for the RMS investigation, we scanned the mirror on an area of 8 mm x 8 mm. For each laser location, the fit of the local curvature is weighted by the power of the TEM_{00} in order to fit the real curvature seen by the Gaussian beam. The real radius of curvature seen by the TEM_{00} is depicted in Fig. 14 for a nominal RoC of 14.02 m.

#240769 Received 12 May 2015; revised 30 Jun 2015; accepted 30 Jun 2015; published 7 Aug 2015

10 Aug 2015 | Vol. 23, No. 16 | DOI:10.1364/OE.23.021455 | OPTICS EXPRESS 21468

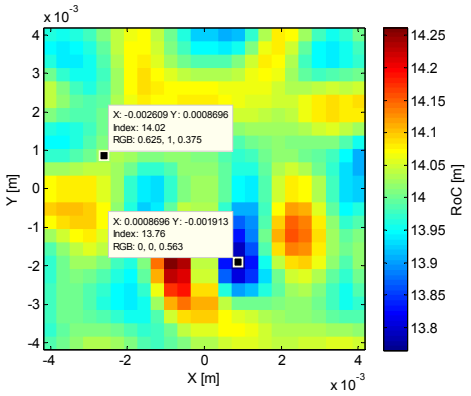

Fig. 14. Real radius of curvature seen by the TEM_{00} when the nominal radius is 14.02m.

We observed that the real curvature locally increases or decreases by about 2% from the nominal curvature. For example, instead of having a real curvature equal to the nominal curvature at 14.02 m, we have 13.76 m of radius of curvature as seen by the TEM_{00}.

However, when we scan the losses as a function of the end mirror nominal radius of curvature, we always observe a loss peak at 14.02 m of nominal radius whatever the laser location on the mirror (as seen in Figs. 8, 9 or 10). In other words, the peaks location of the resonant high order modes is not dependent on the local radius of curvature seen by the TEM_{00}, but it depends only on the nominal radius.

In Fig. 15, we can see the field amplitude of the degenerated high order modes when the nominal radius of curvature is 14.02 m. The order of this mode is 31. As depicted in the Table 2, the real radius seen by the TEM_{00} can vary from 13.760 m to 14.017 m, depending on the location of the laser on the mirror, but the higher order mode will always resonate for the same nominal curvature i.e. the radius of curvature seen by the high order mode does not change significantly.

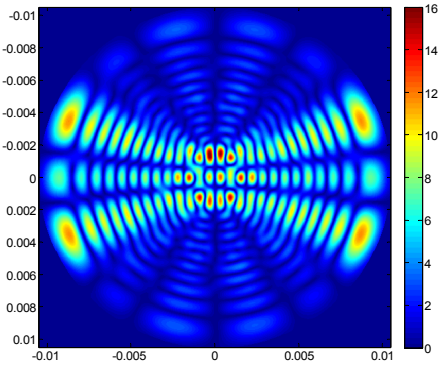

Fig. 15. Field amplitude of the high order mode when the local RoC seen by the TEM_{00} is 13.76 m.

#240769 Received 12 May 2015; revised 30 Jun 2015; accepted 30 Jun 2015; published 7 Aug 2015

Table 2. Comparison between the radii of curvature seen by the TEM_{00} and by one HOM when they are resonant at the same time at 14.02 m of nominal mirror radius of curvature (as seen on one RTL peak), corresponding to 2 positions of the beam on the mirror.

	RoC seen by the TEM_{00} at the RTL peak location	RoC seen by the HOM at the loss peak location
First mirror laser beam location.	14.017	14.02
Second mirror laser beam location.	13.760	14.02

In fact, we checked in Fig. 16 that the curvature seen by the resonant high order mode is very close to the nominal curvature. That is because the higher order mode has a very large spatial extend and hence the random fluctuations of the mirror surfaces average out.

We conclude in this section that the local variation of the radius of curvature does not affect the losses significantly. However the losses can be significantly modulated by the local defects (the local RMS height) depending on the position of the laser beam on the mirror.

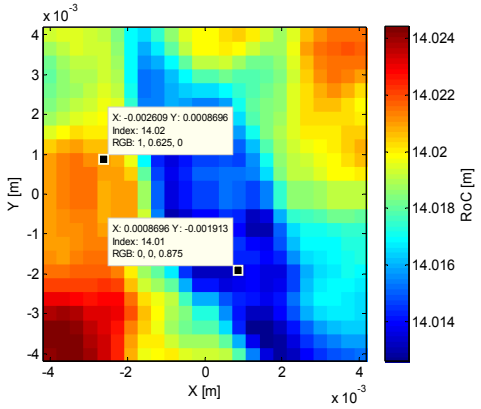

Fig. 16. Radius of curvature seen by the resonant HOM when the nominal radius is 14.02m.

5.4. Conclusion about the low spatial frequency losses

Concerning the low spatial frequency uniformity, we first have to consider that the relevant RMS flatness is the local flatness obtained by weighting the surface height with the laser beam power distribution over the mirror. For the substrates considered in this study we checked that the local flatness seen by the laser beam is below 1 nm with some large area having local flatness smaller than 0.5 nm on average. In some cases, we found that the flatness seen by the laser can be very dependent on the impact of the beam on the mirror surface. We saw that moving the laser beam over a distance less than the waist size in the center of the mirror can easily change the RMS value by a factor 2 or 3 between the best and the worst position of the laser. At the same time, the simulated round-trip losses due to the

#240769 Received 12 May 2015; revised 30 Jun 2015; accepted 30 Jun 2015; published 7 Aug 2015

scattered light in the cavity can increase by a factor 10. But if we carefully tune the laser in an ideal position, we can achieve losses as small as 0.1 ppm.

So far, we never take into account the losses due to the input mirror in the simulations. But we checked that, as expected, adding the defect on the input mirror increases the minimal loss by a factor 2 (input and end mirror maps being different and uncorrelated). As a consequence, we can reach around 0.2 ppm of round-trip loss in the cavity due to the low spatial frequencies flatness.

In the next section we will consider the effect of the surface roughness (the high spatial frequency surface defects).

6. Additional loss due to the high spatial frequencies

The wave-front measurement is only sampled with a pixel size of 350 µm. That means that the maps used previously in order to simulate the round-trip losses, do not include the spatial frequencies above 1400 m^{-1}.

Since the previous simulations are not suitable to take into account the high spatial frequencies, a simple analytical model will be derived to estimate the scattering loss for those frequencies.

First, let's understand how the losses are dependent on the light diffracted by the mirror surface. The diffraction angle θ of a light ray which meets a surface at normal incidence is proportional to the wavelength λ and to the spatial frequency f of the defects. The angle θ is expressed as follows:

$$\theta = f \times \lambda \tag{7}$$

Also, we define θ_{max} the maximal angle of diffraction above which a diffracted ray in the mirror center will exit the cavity. The angle θ_{max} is shown in Fig. 17 and is expressed as following:

$$\theta_{max} = \frac{d}{2L_{cav}} \tag{8}$$

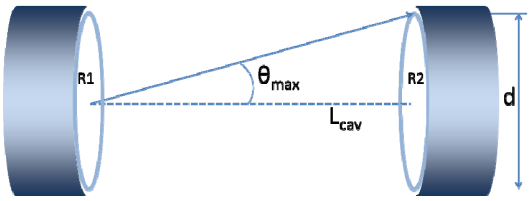

Fig. 17. Diffracted ray at the center of the cavity end mirror.

Using both the Eqs. (7) and (8), we deduce f_{limit} the spatial frequency of the roughness above which the scattered light exits the cavity. We find then:

$$f_{limit} = \frac{d}{2L_{cav} \times \lambda} \tag{9}$$

Equation (9) is an approximate formula based on simple geometry and the grating formula which does not take into account the complex Gaussian profile.

For a ten-meter long cavity made of one inch diameter mirrors, we obtain f_{limit} around 1200 m^{-1}.

The frequency f_{limit} represents a threshold beyond which the light is lost after the first round-trip in the cavity. That is to say it concerns the defects of roughness whose spatial period is below 830 µm. For all the frequencies higher than f_{limit}, the following analytical

#240769 Received 12 May 2015; revised 30 Jun 2015; accepted 30 Jun 2015; published 7 Aug 2015

10 Aug 2015 | Vol. 23, No. 16 | DOI:10.1364/OE.23.021455 | OPTICS EXPRESS 21471

formula gives us a value of the losses per reflection which only depends on the wavelength and of the amplitude of the defects [19]:

$$Loss_{(f>f_{limit})} = \left(\frac{4\times\pi\times\sigma_{RMS}}{\lambda}\right)^2 \quad (10)$$

σ_{rms} is here the RMS roughness whose spatial frequencies are greater than 1200 m^{-1}. This micro-roughness is measured with the "MicroMap" (see section 4).The field of view 1mmx1mm and the pixel size of 2.56 µm allow the measurement of the spatial frequencies between 1000 m^{-1} and 200 000 m^{-1}. As a consequence the MicroMap is the ideal tool for the computation of the roughness σ_{rms} because it can measure spatial frequencies starting from 1000 m^{-1}, which is very close to f_{limit}, the spatial frequency above which the scattered light is definitively lost. Thus, knowing the median of the RMS height σ_{rms} of the micro-maps measured in the section 4 (equal to 0.12 nm), and using Eq. (10), we find an additional loss of 2.0 ppm per mirror due to the light diffracted outside the cavity.

Using Eq. (3), we can also compute the RMS value σ_{rms} by integration of the PSD given in Fig. 5. If the curve is integrated in the range frequency above 1000 m^{-1}, we find now 0.10 nm RMS of roughness leading to 1.4 ppm of additional loss per mirror.

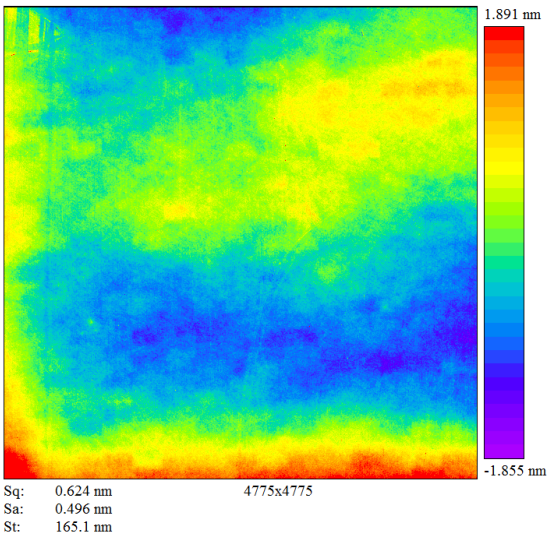

Fig. 18. Roughness map stitched with 225 maps of 1mm aside measured with the optical profilometer "micromap" and a Michelson-type interference objective of 5x magnification. The map size is 12.2 mm x 12.2 mm.

Even if the roughness is quite homogeneous on the entire scanned surface, we nevertheless see in Fig. 3 that some roughness maps are 2 or 3 times higher than the average. Assuming that one map of 1 mm aside measures 25% of the beam size on the mirror, maybe the diffraction of the light due to the local roughness on the mirror could provide more losses than expected previously. So we quantified the exact loss value due to the diffracted light when the laser reaches a large area on the mirror. The ideal area on the mirror must be 3 times greater than the beam diameter of the laser. Using specific software we stitched all the 225

#240769 Received 12 May 2015; revised 30 Jun 2015; accepted 30 Jun 2015; published 7 Aug 2015

10 Aug 2015 | Vol. 23, No. 16 | DOI:10.1364/OE.23.021455 | OPTICS EXPRESS 21472

micro-maps seen in the section 4. Thus, we obtained a large roughness map 12.2 mm aside. The large stitched map includes all the roughness over a real surface of 12.2 mm aside, but low spatial frequency artifacts appeared as shown in Fig. 18. Indeed the total height RMS was 5 times greater than the RMS of one micro-map. However, the low frequency artifact and the mirror flatness have a similar height standard deviation (0.6 nm RMS once the residual focus is removed) and we checked that the PSD of the stitched map is coherent with the other PSD in Fig. 5.

Using now the map in Fig. 18 as surface of the end mirror, we estimated the losses due to the roughness by a numerical method. Still with OSCAR as simulation tool, we computed the power of the electric field propagated over 10 meters after the light (a perfect TEM_{00}) has been reflected off the mirror. The picture of the amplitude of the electric field is shown in Fig. 19. We find then 1.5 ppm of the reflected light falls outside the clear aperture of one inch and is thus lost.

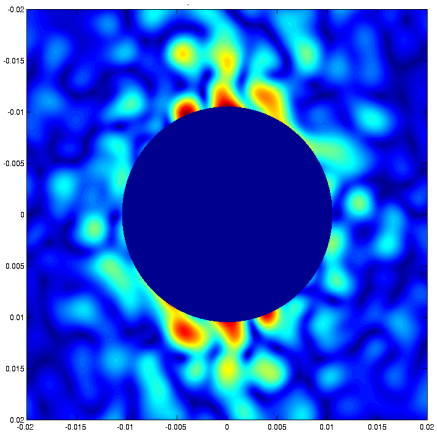

Fig. 19. Amplitude of the electric field falling outside the cavity after reflection off the mirror and propagation over 10 meters. The total amount of light falling off the mirror is 1.5 ppm.

In order to simulate more finely the cavity round-trip loss, we combine the roughness map shown in Fig. 18 and the flatness map shown in Fig. 6 into a single map. Before directly adding the maps, some adjustments are necessary. First they must have the same pixel size. Then, in order to avoid a gap between both maps, the edges of the roughness map were smoothly reduced until the pixels of the periphery fall to zero. At last, the final map used in the FFT simulation had to be adapted to the simulation computing capability. Indeed, using OSCAR, about one million points is considered as reasonable grid size to reduce the computation time. The 12.2 mm aside roughness map was under-sampled to 638 X 638 pixels, while the 21.0 mm diameter low frequency map was over-sampled to 1098 pixels X 1098 pixels.

Finally, the lateral spatial resolution of the “Micromap” which was initially 2.56µm/pixel was reduced to 19.2µm/pixel. However it is still 18 times greater than the spatial resolution accessible with the wave-front measurement. After combining the 2 maps, the maximal spatial frequency of the full map reaches 26000 m^{-1} instead of 1430 m^{-1} when taking into account only the low spatial frequency map. The RMS height of the new map is 0.77 nm in the region where both the maps overlapped, to be compared to the 0.63 nm RMS of the map with only the low frequency.

#240769 Received 12 May 2015; revised 30 Jun 2015; accepted 30 Jun 2015; published 7 Aug 2015

10 Aug 2015 | Vol. 23, No. 16 | DOI:10.1364/OE.23.021455 | OPTICS EXPRESS 21473

Using OSCAR, first we placed the full map as end mirror of the cavity and we computed the round-trip losses (RTL) on a grid size of 1024 x 1024 pixels. Then the same simulation is done but using now the down-sampled map with a pixel size is 350µm as the wave-front map lateral resolution. In both cases, the nominal radius of curvature of the mirrors is set to 14.1 meters. As all the simulations, the clear aperture of the mirrors is set to 21 mm (slightly less to one inch in order to clip the edge defects of measurement and also to consider the realistic coating diameter on the substrate). The losses of both maps are computed on the mode 00 (RTL_{00}). The results are given in the Table 3 for different values of the cavity finesse. We noticed that by adding the high spatial frequency in the simulations, the round trip losses increased by a factor 2. That is an important result, meaning that for realistic estimation of the loss, the wavefront map is not enough and that additional measurements with an optical profilometer are necessary.

Table 3. Simulated Round-trip loss in the cavity using as end mirror the low frequency map associated with the additional high frequencies roughness on the full map. (Radius of curvature = 14.1 m)

Finesse	Full map (= Flatness + roughness)		Full map under-sampled (= Flatness map)	
	RTL_{00} [ppm]	RTL [ppm]	RTL_{00} [ppm]	RTL [ppm]
450	7.6	3.1	5.2	1.4
4500	3.6	3.2	1.8	1.4
45000	3.2	3.2	1.5	1.4

The additional losses we found due to the high spatial frequency are coherent with the simple model from Eq. (10) which predicted losses from high frequency to be between 1.4 ppm and 2 ppm.

7. Loss budget and conclusion

In this article, we highlighted the influence of surface maps to overall round trip losses in the cavity. Different numerical tools have been presented in order to derive in a realistic way the cavity losses.

Using some real data of the surface of standard super-polished optics, we saw that according to the geometry of the cavity, a large number of higher order modes could resonate at the same time as the fundamental one, generating some excess loss. As a result, we showed that for a high finesse cavity, the losses can change by two orders of magnitude if the radii of curvature of the mirrors shifts by only 1%.

Even if the polisher can guarantee the nominal radius of curvature, stress and thickness non-uniformity due to the coating process or thermal effect may shift the mirror radius. In such a cavity, it will be wise to provide a thermal compensation system in order to change the curvature in situ if necessary. Assuming an optimized curvature of the mirrors, we can expect less than 0.2 ppm of loss only due to the low frequency flatness of both mirrors for our 10 m long filter cavity. In the square area of 8 mm x 8 mm at the center of the substrate, we have 80% of chance to reach less than 0.5 ppm of loss and around the same probability to have less than 0.5 nm of local height RMS on the substrate surface.

Finally the additional losses due to the light diffracted outside the cavity by the roughness defects of the mirrors have been estimated. We saw that the high frequency defects could add 3 ppm of loss in the cavity. The finite mirror sizes associated with the roughness of the surface bring around 50% of the overall losses. In our simulations, we did not include possible point defects on the coating or substrate, measurement of large angle scattering indicates that additional loss as low as 2 ppm per mirror could be obtained [20].

If we select mirrors twice larger for the cavity, we checked that the amount of light falling outside the cavity is lower as predicted with Eq. (10). Indeed using the map containing both high and low frequencies, the RTL simulation with 2-inches mirrors gives us 0.7 ppm instead

#240769 Received 12 May 2015; revised 30 Jun 2015; accepted 30 Jun 2015; published 7 Aug 2015

of 3.2 ppm for a finesse of 45000. Using a full flatness and roughness map on each 2-inches mirror of the cavity, we found that the RTL is now 1.3 ppm.

Regarding the mirror specifications, the polishing companies that provided the micro-polished substrates used for this study announce a flatness quality better than λ /10 (λ = 633 nm), in the standard range. Our measurement showed that the optics well exceed those specifications, so we recommend to require the same surface quality we have measured in order to guarantee the losses predicted in this study. For example, the two-inch substrate flatness must be less than λ /20 peak to valley. We also saw that the RMS flatness must be less than 0.5 nm over the central diameter of 10 mm. At last, the most important requirement is the RMS roughness with the spatial frequencies above 1000 m^{-1}, which must be less than 0.15 nm over the central part.

As a conclusion, we recommend that the polished substrates in the 10 meters-long cavity must have a diameter of 2 inches and a radius of curvature of 14.25+/–0.1 meters (cavity g-factor of 0.09). This curvature allows obtaining stable and minimal loss lower than 1 ppm by simulation and without adding the losses due to the roughness. Alternatively a thermal compensation system can be used in order to adjust in situ the radius of curvature.

Appendix A: Defining the cavity round-trip loss

In this section, we detailed the calculation used to derive the formula for the loss (Eq. 4).

For the following sections, we define P_{in}, P_{circ}, P_r and P_t as respectively the input power, the circulating power, the reflected power and the transmitted power of the cavity. We also define $P^{00}{}_{circ}$, $P^{00}{}_{r}$, $P^{00}{}_{t}$ as the circulating power, the reflected power and the transmitted power in the fundamental mode TEM_{00}. The projection of the electric field to the fundamental mode is numerically done with the overlap integral. The input beam of the cavity is always assumed to be in the fundamental mode (i.e. $P^{00}{}_{in} = P_{in}$).

Assuming the conservation of the optical energy by the cavity, what enters in the cavity is equal to what is going out plus what is lost:

$$P_{in} = P_r + P_t + P_{lost} \tag{11}$$

Dividing Eq. (11) of the optical energy conservation by the circulating power, we obtain:

$$\frac{P_{in}}{P_{circ}} = \frac{P_r}{P_{circ}} + \frac{P_t}{P_{circ}} + \frac{P_{lost}}{P_{circ}} \tag{12}$$

Introducing RTL, the round trip power loss and r1, r2 and t1, t2 the amplitude reflectivities and transmissions of respectively the input and end mirror of the cavities, Eq. (12) can be written as:

$$\frac{\left(1 - r_1 r_2 \sqrt{1-RTL}\right)^2}{t_1^2} = \frac{\left(r_1 - r_2 \sqrt{1-RTL}\right)^2}{t_1^2} + t_2^2 + \frac{P_{lost}}{P_{circ}} \tag{13}$$

$$\frac{1 - r_1^2 - \left(r_2^2 - r_1^2 r_2^2\right) + \left(r_2^2 - r_1^2 r_2^2\right).RTL}{t_1^2} = t_2^2 + \frac{P_{lost}}{P_{circ}} \tag{14}$$

$$\frac{1 - r_1^2 - r_2^2 + r_1^2 r_2^2 + \left(r_2^2 - r_1^2 r_2^2\right).RTL}{t_1^2} = t_2^2 + \frac{P_{lost}}{P_{circ}} \tag{15}$$

$$\frac{\left(1 - r_1^2\right)\left(1 - r_2^2\right) + r_2^2\left(1 - r_1^2\right).RTL}{1 - r_1^2} = t_2^2 + \frac{P_{lost}}{P_{circ}} \tag{16}$$

#240769 Received 12 May 2015; revised 30 Jun 2015; accepted 30 Jun 2015; published 7 Aug 2015

$$\left(1-\mathrm{r}_2^2\right)+\mathrm{r}_2^2.RTL=\mathrm{t}_2^2+\frac{P_{lost}}{P_{circ}} \tag{17}$$

$$\frac{P_{lost}}{P_{circ}}=\mathrm{r}_2^2.RTL \tag{18}$$

$$RTL=\frac{P_{in}-\left(P_r+P_t\right)}{\left(\mathrm{r}_2^2\right).P_{circ}} \tag{19}$$

Typically since r_2 is close to 1, it can be neglected. This method to calculate the round trip loss is one of the most widely used because it is relatively easy to implement numerically.

Acknowledgments

The authors gratefully acknowledge the support of the European Gravitational Observatory (EGO). N. Straniero is supported by the EGO collaboration convention for the funding of a fellowship at LMA. G. Cagnoli is grateful to the LABEX Lyon Institute of Origins (ANR-10-LABX-0066) of the "Université de Lyon" for its financial support within the program "Investissements d'Avenir" (ANR-11-IDEX-0007) of the French government operated by the National Research Agency (ANR).

#240769 Received 12 May 2015; revised 30 Jun 2015; accepted 30 Jun 2015; published 7 Aug 2015

Research Article Vol. 36, No. 11 / November 2019 / Journal of the Optical Society of America A C85

Journal of the Optical Society of America A
OPTICS, IMAGE SCIENCE, AND VISION

Large and extremely low loss: the unique challenges of gravitational wave mirrors

Jérôme Degallaix,[1,*] Christophe Michel,[1] Benoit Sassolas,[1] Annalisa Allocca,[2,3] Gianpetro Cagnoli,[4,5] Laurent Balzarini,[1,4] Vincent Dolique,[6] Raffaele Flaminio,[7] Danièle Forest,[1] Massimo Granata,[1] Bernard Lagrange,[1] Nicolas Straniero,[1] Julien Teillon,[1] and Laurent Pinard[1]

[1]Laboratoire des Matériaux Avancés - IP2I, CNRS/IN2P3, Université de Lyon, 69100 Villeurbanne, France
[2]Università di Pisa, I-56127 Pisa, Italy
[3]INFN, Sezione di Pisa, I-56127 Pisa, Italy
[4]Université Claude Bernard Lyon I, 69100 Villeurbanne, France
[5]Current address: Institut Lumière Matière, Université de Lyon, 69100 Villeurbanne, France
[6]Current address: École Nationale Supérieure de Lyon, CNRS, UCBL, Université de Lyon, Laboratoire de Physique, F-69342 Lyon, France
[7]Current address: Laboratoire d'Annecy Le Vieux de Physique des Particules, 74940 Annecy-le-Vieux, France
*Corresponding author: j.degallaix@lma.in2p3.fr

Received 18 June 2019; revised 10 September 2019; accepted 25 September 2019; posted 2 October 2019 (Doc. ID 370180); published 23 October 2019

This paper describes the making of large mirrors for laser interferometer gravitational wave detectors. These optics, working in the near infrared, are among the best optics ever created and played a crucial role in the first direct detection of gravitational waves from black holes or neutron star fusions.

https://doi.org/10.1364/JOSAA.36.000C85

1. QUEST TO DETECT GRAVITATIONAL WAVES

Gravitational waves (GW) are cosmic messengers that reveal the most energetic events in the universe. They originate from accelerating masses and propagate at the speed of light as faint ripples in the fabric of space time, as predicted by Einstein's general relativity [1]. Unlike electromagnetic waves, GW can travel without being absorbed or scattered, carrying undistorted information from their emitting sources.

As gravity is the weakest of the four fundamental forces, GW induce extremely small perturbations, and it once took tremendous dedication to measure them directly on Earth (for a historic perspective, see [2,3]). One century after general relativity, 50 years after the Weber bars [4], giant laser interferometers [5] have finally opened the realm of GW astronomy [6].

Nowadays, a network of GW detectors with the two American LIGO detectors [7] and the French–Italian Virgo [8] is working in coincidence, sharing data, and releasing common publications. At the beginning of 2020, the Japanese underground and cryogenic detector KAGRA [9] will likely join the existing network, enabling better sky localization of the GW sources.

Recent GW detections were only made possible thanks to impressive technological advances on several fronts: laser, suspension, control, and optics. In particular, the large mirrors at the core of the interferometer offer state-of-the-art performance and are the topic of this article because their coating and characterization were made in Villeurbanne, France, at the Laboratoire des Matériaux Avancés (LMA). More precisely, we will focus on the advanced Virgo large optics from an optical point of view but with limited mention of coating thermal noise.

A. Astrophysical Sources

Typical GW sources whose amplitudes could be detected on Earth must necessarily involve large masses (in the order of the mass of the sun or larger) and with a rapidly evolving nonspherical mass distribution. Typical sources include coalescence of compact binary objects, nonspherical pulsars, and core collapse supernovae.

The first direct observation of GW was recorded in September 2015, with a short signal lasting less than 1 s, seen in both LIGO detectors. The waveform was the unambiguous signature of the merging of two black holes of 36 and 29 solar masses at a luminosity distance of 1.3 billion of light years [10], and no deviation from general relativity has been observed [11]. This fusion was one of the most energetic events in the universe ever recorded, as the equivalent of three solar masses has been radiated with gravitational waves but without any electromagnetic counterpart.

The second GW landmark event occurred in August 2017, with the first recorded by the network of three detectors (the two

C86 Vol. 36, No. 11 / November 2019 / Journal of the Optical Society of America A Research Article

LIGO in the United States and Virgo in Europe) of the fusion of two neutron stars [12]. In parallel with the GW emission, a firework in the electromagnetic domain was also observed ranging from a coincident high-energy short gamma-ray burst to messengers in the visible and radio spectrum [13] lasting several days. This historic kilonova gave a limpid explanation of the origin of a short gamma-ray burst and outstanding constraint on the (non) difference between the speed of GW and the speed of light. This discovery marks the beginning of the multimessengers astronomy with GW.

More than 10 sources have already been officially detected during the first and second periods of data-taking [14], which took place in the years 2015–2017. At the time of this writing, after four months of the third observational run (O3, which must last one year), more than 25 candidate events have been announced [15].

B. Advanced GW Detectors

Because a passing GW induces a differential length change between two perpendicular directions, laser GW detectors are based on the layout of a Michelson interferometer. The differential length change generates a differential phase shift of the laser light reflected by the two arms, which is then recorded as a power modulation on the detection port. To enhance the GW signal imprinted in the phase of the light, several strategies could be combined, the two most noticeable ones are long arms in the order of the kilometer and resonant Fabry–Perot cavities instead of single-end mirrors.

The current interferometers are called "advanced interferometers" or "second-generation interferometers" because they are a major upgrade of the initial LIGO or Virgo detectors built at the beginning of this century and decommissioned in the years 2009–2011.

As an example, a simplified layout of the advanced Virgo detector is shown in Fig. 1. The two-arm Fabry–Perot cavities are 3 km long and are under high vacuum (10^{-9} mbar) to limit extra phase noise induced by residual gas. The Michelson is operated on the dark fringe, and, to further enhance the circulating light (and hence increase the signal-to-noise ratio), an extra cavity is formed between the laser and the input mirror arm cavity mirrors: the power recycling cavity. At the output of the detector, a low finesse cavity (finesse 5-10) also exists: the signal recycling cavity, which can tune the optical response of the detector to enhance the GW signal within a particular frequency band.

For the final configuration of advanced Virgo, the input laser at 1064 nm will deliver 200 W, leading to 5 kW circulating in the recycling cavity and up to 600 kW in the arm cavities. Two compensation plates have been added in the front of the two input mirrors to correct thermal effects. By shining a controlled CO_2 laser beam on the plates, active wavefront correction could be achieved [16].

For current interferometers, the maximum displacement sensitivity is achieved around 100 Hz, with an amplitude spectral density of less than 10^{-19} m/$\sqrt{\text{Hz}}$. In the low-frequency range between 10 and 100 Hz, the sensitivity is limited by angular and control noises, whereas, above 100 Hz, the interferometer is limited by coating thermal noise and shot noise [17].

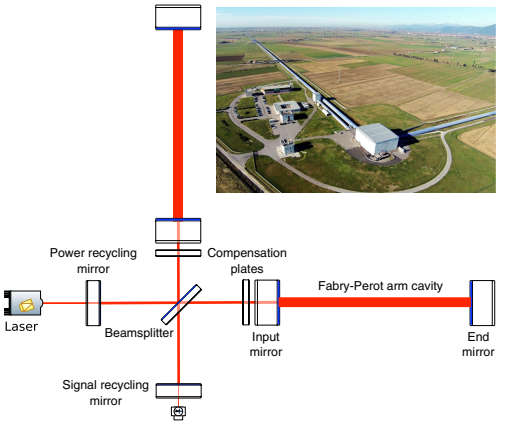

Fig. 1. Simplified optical layout of the advanced Virgo interferometer near Pisa in Italy. The configuration is a dual recycled Michelson with Fabry–Perot arm cavities. The GW signal imprinted in the phase of light is detected at the south port in this diagram. Inset: Aerial view of the detector, where one of the 3 km long arms is clearly visible. Credit: Virgo Collaboration.

2. MOST CRITICAL LARGE MIRRORS: THE MAKING OF

In this paper, we will focus on the two large input and two end mirrors forming the long arm cavities, later called by the acronyms IM and EM. Those mirrors are the most critical of the interferometers and thus have the most severe specifications. In total, eight such mirrors were produced for Virgo, four IMs and four EMs, to include a spare set of optics.

A. Material Choices

In this section, we briefly describe the motivations regarding the material choices for the substrate and coating.

1. *Fused Silica Substrates*

For the substrate material, the choice went naturally to fused silica, already used in the first generation of detectors. This material is highly transparent for near infrared, homogeneous, and comes in large dimensions. On top of its outstanding optical properties, fused silica exhibits low mechanical loss at room temperature [18], which translates to low displacement induced by the bulk thermal noise [19]. Moreover, it is possible to create fused silica fibers and attachment ears, which allows the implementation of a monolithic suspension all made of fused silica [20]. That was a crucial step to reduce the suspension thermal noise, which could potentially limit the sensitivity of the detector at low frequency [17].

As fused silica is widely used, polishing and coating processes are also well mastered for this material.

Research Article Vol. 36, No. 11 / November 2019 / Journal of the Optical Society of America A C87

2. Coating Materials

The coating is a Bragg reflector composed of two materials alternated. The low refractive index layer is made of silica ($n = 1.45$ at 1064 nm), from the same grade as the mirror substrate, while the high refractive index one is titania-doped tantala ($n = 2.09$) [21].

Those materials were selected because they present extremely low optical absorption [22] and scattering. When the interferometers reach their design sensitivity, it is expected that the coating thermal noise will be the dominant source of noise in the most sensitive midfrequency range from 50 Hz to few hundreds Hz. Because the thermal noise amplitude is directly related to the internal friction of the materials through the fluctuation-dissipation theorem [23], it is of utter importance to find material exhibiting low mechanical dissipation [24].

Using monolayers deposited on disc resonators [25], the mechanical loss of each material can be derived by fitting the mechanical ringdown of the resonator after electro-static excitation. Different values can be found in the literature according to the deposition process or parameters. The latest measurement on the coating layers of advanced LIGO and Virgo indicates a loss angle of 2.3×10^{-5} for fused silica (SiO_2) and 2.4×10^{-4} for titania-doped tantala ($Ti : Ta_2O_5$). Both values are extrapolated at 100 Hz (further details can be found in [25,26]). Thus, one can deduce that the coating thermal noise is dominated by the mechanical loss of the high refractive index material, which explains the current worldwide effort to optimize tantala or find a replacement material. The losses of nondoped tantala are around 25% higher compared with the doped material.

B. Crucial Role of Optical Simulations

The optical simulations were essential to design the interferometers and maximize the astrophysical range of the instrument. Most of the numerical tools used have been developed within the Virgo and LIGO collaborations, so those packages are usually open source and nowadays implemented in MATLAB or Python.

The first optical simulations aim to fix the finesse of the arm cavities and the gain of the recycling cavities. This optimization is a compromise because higher sensitivity can be achieved with arm cavities with higher finesse, however at the price of lower bandwidth of the detector. Note that a low bandwidth can be recovered with a particular tuning of the signal recycling mirror at the output of the instrument. At that design step, the known noise sources (technical and fundamental) are also included in the simulations to find the optimal sensitivity. An example of such a simulation package is GWINC, written first for MATLAB and translated since then in Python [27]. For advanced Virgo, the 3 km long arm overcoupled cavities have a finesse of 450, and the transmission of the power recycling mirror is 5% (power gain of 40); for the signal recycling mirror, the transmission is 40%.

In GWINC simulations, only plane waves are used with a simplified optical loss model. An important result from this first round of simulations was to set the goal for the optical round-trip loss of the arm cavities, i.e., it must be less than 75 ppm per round trip in order to achieve the desired circulating power. This extremely small loss number for a long cavity has a direct impact on the quality of the mirrors.

Thus, the second kind of simulations developed are called "FFT codes," which can use realistic laser beams with nonperfect mirror surfaces [28]; those optical cavity simulations include the realistic shape of the mirrors with the proper curvature but also with the expected 2D height of the surface to simulate imperfect polishing or nonuniform coating deposition. This work was essential to check the nondegeneracy of the arm cavities (between the fundamental mode and the higher-order modes) and set the polishing specifications in term of surface flatness and roughness. To achieve the goal of the round-trip loss of 75 ppm, the surface flatness must be less than 0.5 nm RMS over the central part (equivalent to $\lambda/160$) with a roughness of 0.1 nm RMS for the high spatial frequencies. FFT codes include SIS from the LIGO collaboration and DarkF or OSCAR [29] from Virgo, an example to design a low-loss long high finesse cavity using such simulations can be found in [30].

The mirror specifications were also derived using modal expansion codes, where the laser beam is expanded over the basis of the Hermite–Gauss modes. Those simulations are fast, can compute optical transfer functions, and include full treatment of the quantum noise (radiation pressure noise and shot noise). Those are typically used to derive the locking strategy, noise coupling in case of reflectivity asymmetry, or understand alignment instability due to radiation pressure. The most-used tool for such simulations is called Finesse [31].

C. Substrate Dimensions and Measured Properties

For advanced Virgo, both input and end mirrors (IMs and EMs) of the long arm cavities have the same dimensions: the diameter is 350 mm and the thickness is 200 mm, and the substrate weight is 40 kg. Because the substrate of the IMs is inside the power recycling cavity, crossed with several kWatt of laser light, an extremely low absorption fused silica glass from Heraeus, Suprasil 3002, has been selected.

Due to the small transmission of the EMs ($T \approx 4$ ppm), only few watts of light will pass through those substrates, so the optical absorption is less critical there; thus, Suprasil 312 was chosen.

A summary of the different optical properties of the substrates is given in Table 1, confirming the outstanding quality of those large pieces. No inclusion or bubbles were also detected in the substrates. The bulk optical absorption is a critical parameter, as up to 2 kW of laser light is expected to circulate in the IMs substrates, generating a thermal lens. This extra focusing in the recycling cavity must be actively corrected by the thermal compensation system, which is designed to correct absorption only below 0.5 ppm/cm. The refractive index inhomogeneity and birefringence can induce wavefront distortion or contrast defect and so are considered as additional sources of optical losses in the recycling cavity.

The absorption was measured at LMA with the photodeflection technique (also called "mirage effect") [33]. This is one of the sensitive techniques, as bulk absorption as low as 0.1 ppm/cm could be measured. The homogeneity and birefringence were measured by Heraeus and provided in the inspection reports of each glass blank. The birefringence is measured point by point over the central area on a commercial setup; then, a

C88 Vol. 36, No. 11 / November 2019 / Journal of the Optical Society of America A Research Article

Table 1. Measured Optical Parameters for the Arm Cavity Substrates[a]

Substrate	Material	Absorption [ppm/cm]	Homogeneity [nm]	Birefringence [nm/cm]
IM	Suprasil 3002	0.2	0.9	1.1
EM	Suprasil 312	2.3	0.5	0.7

[a]The absorption is given for 1064 nm, measured on witness samples. The homogeneity and birefringence are given as the peak-to-valley measured over the central 200 mm diameter; the average value over the four substrates of each kind is given. Complementary information regarding the different grades of Suprasil can be found in [32].

2D map is reconstructed. The spatial homogeneity of refractive index transverse to the optical axis is measured with a phase shifting interferometer, while the unpolished optic is inserted between two plates with an oil index matched liquid [34].

D. Polishing Achievement

The polishing is also a key ingredient for these large mirrors, as the flatness or roughness could have a direct impact on the optical losses inside the arm cavities and, indirectly, the overall performances of the detectors. Stringent surface specifications have been derived thanks to optical simulations on the central 150 mm diameter (~ 3 times the laser beam radius); then, a global call for tender has been issued to find potential companies that can manage such a work.

According to the optical simulations, the required specifications for the flatness must be less than 0.5 nm RMS over the central 150 mm and less than 3 nm RMS over the whole 300 mm diameter. Such a constraint on the flatness makes the use of ion beam figuring [35] mandatory. In conjunction with the extremely low flatness, low roughness was also required. Over the central area, the high spatial frequency surface height must be less than 0.1 nm RMS to guarantee low scattering. The achieved specifications are summarized in the Table 2.

The radius of curvature (RoC) of the arm cavity mirrors is around 1.5 km (half the cavity length). The radii were selected to avoid degeneracy between the fundamental mode and higher-order modes and also to have a beam slightly smaller on the input mirror compared with the end mirror (the beam radius is, respectively, 49 versus 58 mm on the end mirror).

To ensure good contrast at the dark fringe of the interferometer, it is essential to have the Gaussian beam parameters of the two arms' cavities to be as close as possible. Thus, it was required that the RoCs of the four IMs must be within 3 m of the average RoC of the four parts (idem for the EMs). That was achieved, as shown in the Table 2, where ΔRoC column represents the largest RoC difference between two substrates.

Table 2. Summary of the Polishing RoC Specifications and Measured RoC, Flatness, and Roughness[a]

Substrate	Specified RoC [m]	Measured RoC [m]	ΔRoC [m]	Flatness [nm RMS]	Roughness [Å RMS]
IM	1420 [+15/ −5]	1425.2	0.3	0.2	0.9
EM	1683 [+17/ −3]	1690.5	1.4	0.2	0.9

[a]For the flatness and roughness, the measurement is done on the central 150 mm, and the average over the four substrates is given.

To be noted, the EM substrates have a classical shape with a concave high-reflectivity (HR) surface and a flat antireflective (AR) surface with a wedge. The IM substrates are different with a convex–concave shape and with identical radii of curvature on both sides. This particular geometry was designed to benefit from the etalon effect inside the substrate between the HR and AR side [36]. By small thermal actuation, it is then possible to modulate the overall transmission of the input mirrors and hence tune the finesse of the arm cavity.

Due to the thick substrate (length of 20 cm), it was decided to compensate the IM substrate refractive index inhomogeneity by properly shaping the AR side to limit the wavefront distortion in transmission. After this optimization, the single-pass transmission aberration was less than 5 nm for the amplitude of the Zernike focus term ($Z_{2,0}$) and less than 1 nm RMS for wavefront aberration (tilt and focus removed), all measured on the central 150 mm diameter.

The eight-arm cavity substrates were polished by Zygo, with the first part delivered after one year and the total order took 18 months to be completed after initial reception of the blanks.

E. Coating Process

Once the mirrors have been polished, the final ingredient to have a mirror is the thin film deposition. To limit the optical loss and the coating thermal noise, ion beam sputtering (IBS) is the preferred technique.

1. Coating Design

The coating recipe is not a standard quarter-wave stack but has been optimized in order to reduce the quantity of Ti : Ta_2O_5 while keeping the same optical properties (at the price of increasing the thickness of SiO_2). This optimization was necessary to further reduce the coating thermal noise with a theoretical gain of 14% in the coating loss angle [37].

The coating for the input mirror (transmission of 1.4%) is composed of 18 layers for a total thickness of 2.8 μm; for the end mirror, which is almost perfectly reflective (transmission of 4 ppm), the coating has 38 layers and is 5.9 μm thick.

It should be mentioned that the coating has the main reflectivity band at 1064 nm but also at 532 nm for the auxiliary lasers helping to control the arm cavities during the lock acquisition [38] and also one around 800 nm for the diagnostic Hartman beam of the thermal compensation system [39].

2. Process

After polishing, once the substrates arrived in the clean room (ISO 3) at LMA, they were first cleaned and then characterized to validate the polishing work. Then, they were mounted in the largest IBS coating machine of the laboratory (dimensions: 2.2 m × 2.2 m × 2 m), as shown in Fig. 2. This chamber is custom-made, specifically designed for the Virgo project in

Research Article Vol. 36, No. 11 / November 2019 / Journal of the Optical Society of America A C89

Fig. 2. Front door of the large IBS coater at LMA once the machine is closed. Credit: Cyril Fresillon/LMA/CNRS Photothèque.

2008, and is so large that two 350 mm diameter mirrors can be coated at the same time.

Several years of development were necessary to achieve sub-nm flatness for a reflectivity stack. That was possible after the implementation of a planetary motion system [40] with an oscillatory optimized mask [41]. After coating, the mirrors were annealed (500°C during 10 h), characterized (see next section), and cleaned one last time before expedition.

3. OPTICAL PERFORMANCES

This section describes extensively the characterization of the mirrors coated in the years 2014–2015 and installed right after on the Virgo site. The *in situ* performances are also discussed at the end of the section.

A. Individual Characterization at LMA

After coating and annealing, each IMs and EMS is characterized individually inside the clean room at LMA. The different metrology tools have been adapted to handle the 40 kg large optics and are able to study the uniformity of the measured parameters. All the results reported in this section are given over the central 150 mm diameter of the optics.

1. Transmission Measurement

The 2D transmission maps of the mirror are measured point by point over the central part. As the two IMs and EMs are coated during the same run, similar transmission is expected for the two mirrors. This assumption is confirmed by the measurement, as the differences of transmission are found to be within the incertitude of the instrument.

The two input mirrors have a measured transmission of 1.375% and 1.377% within the specifications of 1.4% ± 0.1%; as expected, the transmission matching is good. The two end mirror transmissions are 4.4 and 4.3 ppm within the specification of 5 ppm ±1.

2. Wavefront Measurement

The reflected wavefront from the mirror is measured using a Zygo wavelength shifting interferometer. Compared with the usual phase shifting interferometer, this device can distinguish separately the different surfaces of the optics without potential interference between the front and back surfaces when no wedge is present. This feature is essential to measure with subnanometer precision the wavefront of the IM because its two surfaces are parallel.

In addition, compared with other similar devices, which are usually operating at 633 nm, the LMA interferometer is working at 1064 nm, the wavelength of the main laser of Virgo, which is essential to properly measure the phase shift experienced by the light after reflection on the Bragg mirror. During the qualification of the instrument, the reproducibility of the measurement was estimated to be less than 0.3 nm RMS.

To be able to measure the whole surface of the mirror at once, the Zygo interferometer is fitted with an 18-in. (450 mm) beam expander (clear aperture of 80%); further, flat (400 mm diameter) and curved (300 mm diameter) references are used for the metrology. A typical measurement before and after coating on the same mirror is shown in Fig. 3. In the bottom plot of Fig. 3, one can notice an additional "doughnut"-shaped feature at the surface of the mirror. That is a consequence of the small coating nonuniformity in layer thickness, and this shape can be well explained with the uniformity measured on the fused silica and tantala monolayers.

A comparison before and after the coating has shown that the RoC has only changed by 1 m, and the flatness has only been degraded from 0.3 nm RMS before coating to 0.4 nm RMS for this mirror. A cross section of the mirror surface height over the central 280 mm is shown in Fig. 4. Considering that the EM coating is 5.9 μm thick, the coating uniformity is less than 0.5% over this large area, and less than 0.1% in the central part.

3. Scattering

Once coated, the optical scattering of the mirrors is measured. For that purpose, a CASI scatterometer has been modified to be able to measure the bidirectional reflectance distribution function (BRDF) on large optics and also to do a 2D scan of the surface, measuring the position-dependent scattering at a given angle. As with other metrology instruments, the wavelength of operation is 1064 nm.

A typical picture of the 2D scattering is shown in the top plot of the Fig. 5 for one of the EMs. The scattering is uniform, and the total integrated scattering account for 4 ppm of optical loss (within ±1 ppm for the four mirrors). The total loss of the IMs has been measured to be 3 ppm ±1 ppm.

4. Optical Absorption

The optical absorption of the coating at 1064 nm is also measured on all the parts. To be able to reach sub-ppm level, the photodeflection technique (also called "mirage effect") is used [33]. A 30 W laser at 1064 nm is focused on the coating, part of the light is absorbed, generating a temperature gradient in the substrate, which is then monitored by the deflection of a low

C90 Vol. 36, No. 11 / November 2019 / *Journal of the Optical Society of America A* Research Article

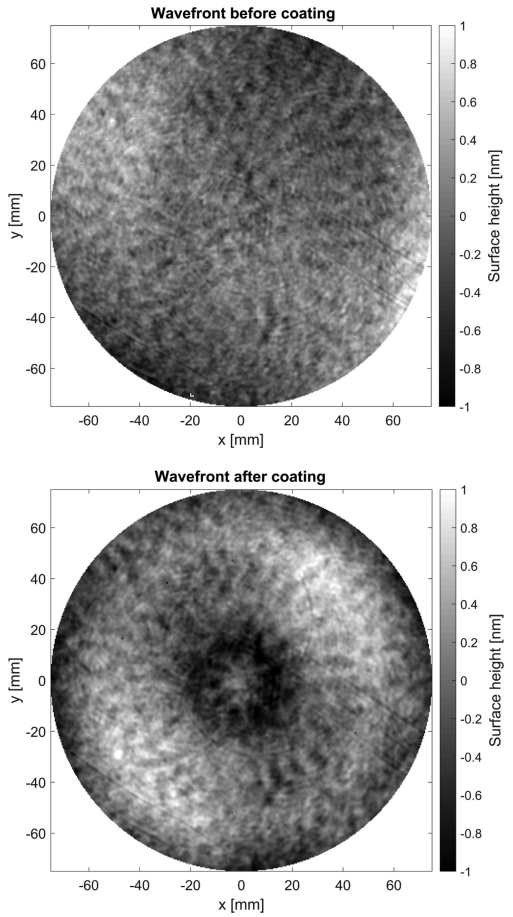

Fig. 3. Wavefront measurement of one end mirror before (top) and after coating (bottom), piston, tilt and curvature removed. The same vertical scale is used for both plots with a vertical height amplitude of 2 nm.

power probe laser beam (at 633 nm). To increase the signal-to-noise ratio, the high-power beam is intensity modulated by a chopper, and the deflection is then demodulated accordingly using a lock-in amplifier.

The optical absorption of the coating is measured at 0.3 ppm ±0.1 on all the parts below the 0.5 ppm given in the specifications.

5. *Antireflective Coating*

The antireflective (AR) coating is also characterized with the scatterometer device but in a different configuration, as we are looking to quantify the direct specular reflection. Reflectivity as low as 10 ppm could be measured.

The AR side of the IMs is within the power recycling cavity; thus, a low AR coating there is critical to avoid unnecessary large

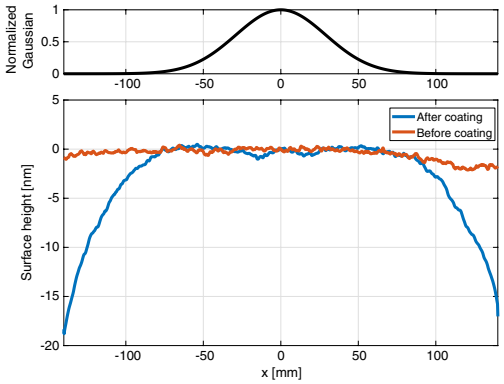

Fig. 4. Comparison of the large-scale mirror shape before and after coating for the same mirror as the one shown in Fig. 3. The plot is given for an EM mirror (coating 5.9 μm thick) over the central 280 mm diameter but the tilt and curvature are removed over the central 150 mm. For reference, in the above plot, the intensity of the Gaussian on the beam on the mirror is shown.

optical loss or too large etalon effect within the substrate. Ideally a reflectivity of less than 100 ppm is recommended, keeping in mind that performances of such AR coating are sensitive to small variations (deviations from the nominal thickness or expected refractive index) that may happen during the coating process. As an example, a random error of 1% on each layer can add 100 ppm of reflectivity. Compared with the HR coating, the total thickness for the AR coating is relatively thin at 1.1 μm and made of 16 layers.

For the first set of two IMs installed on the site, the AR coating reflectivity was measured at 32 and 58 ppm ±10. Even if the optics are coated at the same time, differences in the performances are noticeable. That is understood, as the two mirrors in the coating chamber do not follow exactly the same path during the deposition process. Indeed, for each layer, the substrates in planetary motion are not doing an integer number of turns in the machine, resulting in a nonuniform deposition. This and the extreme sensitivity to error of the AR coating also explains why the low AR coating (reflectivity below 200 ppm) usually presents a gradient of reflectivity, as shown in the bottom plot of Fig. 5.

The AR reflectivity of the second set of two IMs, used as spares and coated four years later, was measured on average at 140 ppm ±50.

6. *Loss Angle Measurement Full Stack*

The loss angle of the full coating stack of the mirrors is not measured directly on the large mirror themselves but on witness samples (1-in. optics or 3-in. wafers), which are coated in the same run as the large optics. The mechanical loss on the wafers is measured using the ring-down technique previously mentioned for both input and end mirrors, while the displacement noise has been directly measured on standard 1-in. substrates at MIT but only for the end mirrors because a low transmission is required for this experiment [42].

Research Article Vol. 36, No. 11 / November 2019 / Journal of the Optical Society of America A C91

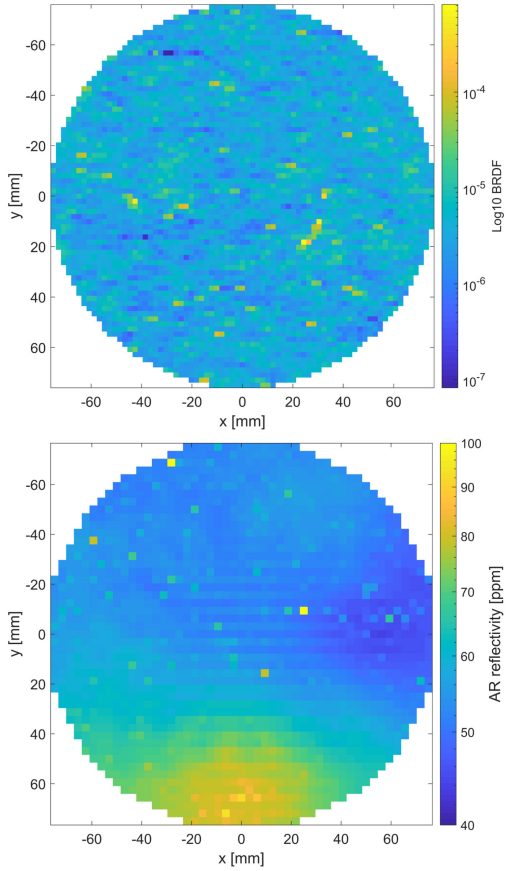

Fig. 5. Scattering uniformity of one EM (top) and uniformity of the AR coating of one IM (bottom). The total scattering loss is estimated at 4 ppm for the top plot. The average reflectivity for the AR of the IM shown is 58 ppm (bottom plot). All the plots are given over the central 150 mm diameter.

The coating loss angles from disks are measured at 1.38×10^{-4} and 2.30×10^{-4} at 100 Hz for, respectively, the IM and EM coatings [26]. The higher loss angle for the EMs is a direct consequence of the larger quantity of tantala with respect to fused silica in those mirrors compared with the IMs [25]. From the measured EM loss angle and using the test mass properties and beam parameters for advanced LIGO, the coating displacement noise can be derived [24] and is found to be 8.0×10^{-21} m/$\sqrt{\text{Hz}}$. This value is in good agreement with the direct measurement done on the MIT setup and reported to be 7.5×10^{-21} m/$\sqrt{\text{Hz}}$ for the EM coating [43].

B. Interferometer In Situ Measurement

Once the mirrors described in this paper have been installed on the Virgo site, an extensive campaign was launched to measure *in situ* the optical properties of the arm cavities and compared them with the expectation.

The first essential parameter is the cavity round-trip loss, which, as mentioned earlier, is directly related to the quality of the mirrors and must be below 75 ppm. This parameter is also extremely sensitive to contamination or improper handling of the optics. The performances of each optics is known in the LMA clean room, but once one site, in the vacuum tank, is suspended with thin glass fibers, there is always the worry that the performances may have been degraded during the installation. To derive the cavity round-trip loss, the reflected power of the cavity is measured, while the cavity is locked and unlocked. The difference between these two measurement is directly related to the finesse of the cavity and round-trip loss. Both cavities have been measured with an identical round-trip loss of 55 ppm $\pm$10, which is within the specifications.

The finesse of the cavity is also estimated after installation. Because the optical losses are negligible and the EMs near perfectly reflective, the finesse of the arm cavities is related to the transmission of the input mirrors. The finesse was derived while leaving the cavity mirrors free swinging and so crossing multiple resonances of the fundamental mode. Due to the low bandwidth of the cavity (the cavity frequency pole is around 55 Hz), the transmission is not simply a Airy peak but presents a more complicated shape with damped oscillations [44]. The finesses of the two arm cavities have been measured at 455 ± 5 and 467 ± 7, for an expected value of 456. This difference observed may be due to the etalon effect in the input mirror substrates, which has been left uncontrolled at the time of the measurement.

During the free swinging of the cavity, one can also measure the frequency separation between optical modes to derive the g-factor of the cavity, which is linked to the mirrors' RoCs. To further excite the higher-order modes and make them visible, the cavity is slightly misaligned (the EM is tilted by 1 μrad). The measured g-factor is 1% shorter from the expected value derived from the individual RoC measurement at LMA, which is equivalent to a decrease of the RoC by 5 m (over an average of 1.5 km).

4. OTHER LARGE OPTICS

Two different kinds of optics are also worth mentioning, as these are distinct from the arm cavity mirrors mentioned in this article.

First, the advanced Virgo beam splitter, which is the largest substrate-coated. Its diameter is 550 mm for a thickness of 65 mm. Due to its location in the recycling cavity, the optical loss is less critical compared with that of the arm cavity mirrors (flatness required to be less than 2 nm RMS). While the beam size at the beam splitter is similar to those at the IM and EM, this optic is positioned at 45 deg of the incident beam; further, the central diameter with stricter specifications has to be enlarged by a factor $\sqrt{2}$. In particular, the coating uniformity has to be improved compared with the arm cavity mirrors. This optic can only be treated in single rotation; no masking was used, but the uniformity was optimized by tuning the angle of the targets. At the end, a uniformity of 0.1% was achieved over a diameter of 200 mm.

C92 Vol. 36, No. 11 / November 2019 / *Journal of the Optical Society of America A* Research Article

A different kind of optics has also been coated for the Japanese gravitational wave detector KAGRA [9]. Because the main optics are operating at a cryogenic temperature (20 K), fused silica can no longer be the material of choice; thus, crystalline sapphire substrates have to be used. Low optical loss sapphire cannot be produced as large as possible for fused silica, so the dimensions of the arm cavity mirrors are smaller: diameter of 220 mm for a thickness of 150 mm. A good surprise was that the polishing capability of sapphire has greatly improved over the years, and now surface quality as good as the one of fused silica could be obtained [45] (albeit with a still larger cost and manufacturing time). A stack of SiO_2 (nondoped) Ta_2O_5 was used for the coating to avoid a possible thermal noise peak at around 25 K [46]. Following the optical characterization on individual mirrors, similar excellent performances have been found compared with what was achieved on fused silica substrates. *In situ* measurement with the mirrors at cryogenic temperature is currently ongoing.

5. NEXT GENERATION OF MIRRORS

In the coming years, a large upgrade of the Virgo and LIGO interferometers will take place to increase the sensitivity of the detector by a factor of 2 (the so-called "plus" upgrade [47]). This goal will be achieved through the injection of frequency-dependent squeezed light, together with a new set of arm cavity mirrors with lower thermal noise. For this last point, a worldwide research effort is currently underway to find coating materials with lower mechanical loss angles. Several strategies are currently explored: testing different deposition parameters, doping materials or annealing temperatures as well as finding a substitute for Tantala (see [48] and references therein). Testing coating recipes made with more than two materials [49] also seems a promising path. Thus far, in summer 2019, no clear coating recipe has been found to meet the challenges of coating with lower thermal noise and low optical absorption as well as being available in large dimensions.

In recent years, crystalline coating for high reflective optics has demonstrated outstanding properties, as it combines lower thermal noise (up to a factor of 10 reduction compared with amorphous coating [50]) combined with excellent optical properties on par with the best IBS coating [51]. Those have become a technology to consider for optics in high precision experiments. However, the availability of size compatible with GW detectors (ideally superior to 300 mm diameter) has yet to be demonstrated.

In the longer term, a next generation of GW detectors will be built on new sites and should be operating around the years 2030–2035. Those interferometers, called "Einstein telescope" (ET) [52] for the European project and "cosmic explorer" (CE) for the American one [53], will aim to be 10 times more sensitive than the second generation of interferometer, detecting all the stellar mass black hole fusions in the universe.

Those interferometers will have longer arms, 10 km for ET and 40 km for CE, and will have larger mirrors with diameters up to 700 mm for a weight of several hundreds of kg. According to the current plan, ET will be located underground with a room-temperature high-power interferometer (up to 3 MW of 1064 nm light circulating in the arm cavities) using fused silica mirrors and a cryogenic low-power interferometer (20 kW of light in the arm cavities at 1550 nm) with silicon substrates. For CE, the main laser will be at 1064 nm, and up to 1.4 MW will circulate in the arm cavities. In a second phase, silicon test masses at 120 K will be used with 2 μm light.

As seen above, the technology of high-reflective coating for GW detection and precision measurement in general is still progressing to ensure ever lower mechanical and optical loss as well as meeting the challenges of low temperature and large optics.

6. CONCLUSION

The direct detection of gravitational waves is one of the most impressive scientific achievements of this new century. This new astronomy was made possible with giant laser Michelson interferometers with low loss large optics. As described in this article, different ingredients, all outstanding, were necessary to manufacture those exceptional parts. In particular, the last steps, the coating and metrology, were done in Laboratoire des Matériaux Avancés in France following 10 years of research and development on the materials and deposition techniques to achieve large uniform coating while keeping low optical and mechanical loss.

Funding. Centre National de la Recherche Scientifique; Instituto Nazionale di Fisica Nucleare; Foundation for Fundamental Research on Matter.

Acknowledgment. The authors gratefully acknowledge the Italian Istituto Nazionale di Fisica Nucleare (INFN), the French Centre National de la Recherche Scientifique (CNRS), and the Foundation for Fundamental Research on Matter supported by the Netherlands Organisation for Scientific Research for the construction and operation of the Virgo detector and the creation and support of the EGO consortium.

REFERENCES

1. M. Maggiore, *Gravitational Waves: Volume 1: Theory and Experiments* (Oxford University, 2008), vol. **1**.
2. J. Levin, *Black Hole Blues and Other Songs from Outer Space* (Anchor, 2016).
3. M. Bartusiak, *Einstein's Unfinished Symphony: The Story of a Gamble, Two Black Holes, and a New Age of Astronomy* (Yale University, 2017).
4. J. Weber, "Detection and generation of gravitational waves," Phys. Rev. **117**, 306 (1960).
5. R. X. Adhikari, "Gravitational radiation detection with laser interferometry," Rev. Mod. Phys. **86**, 121–151 (2014).
6. The LIGO and Virgo collaborations, "Observation of gravitational waves from a binary black hole merger," Phys. Rev. Lett. **116**, 061102 (2016).
7. J. Aasi, B. Abbott, R. Abbott, T. Abbott, M. Abernathy, K. Ackley, C. Adams, T. Adams, P. Addesso, R. Adhikari, and V. Adya, "Advanced Ligo," Classical Quantum Gravity **32**, 115012 (2015).
8. The Virgo collaboration, "Advanced Virgo: a second-generation interferometric gravitational wave detector," Classical Quantum Gravity **32**, 024001 (2014).
9. T. K. Collaboration, "Construction of KAGRA: an underground gravitational-wave observatory," Prog. Theor. Exp. Phys. **2018**, 013F01 (2018).

10. LIGO Scientific Collaboration and Virgo Collaboration, "Properties of the binary black hole merger gw150914," Phys. Rev. Lett. **116**, 241102 (2016).
11. LIGO Scientific Collaboration and Virgo Collaboration, "Tests of general relativity with gw150914," Phys. Rev. Lett. **116**, 221101 (2016).
12. The LIGO and Virgo Collaborations, "Gw170817: observation of gravitational waves from a binary neutron star in spiral," Phys. Rev. Lett. **119**, 161101 (2017).
13. The LIGO and Virgo Collaborations, "Multi-messenger observations of a binary neutron star merger," Astrophys. J. Lett. **848**, L12 (2017).
14. LIGO Scientific Collaboration and Virgo Collaboration, "Gwtc-1: a gravitational-wave transient catalog of compact binary mergers observed by LIGO and Virgo during the first and second observing runs," arXiv:1811.12907 (2018).
15. S. Cooper, A. Jones, S. Morrell, and G. Smetana, "Listening to the gravitational wave cosmos," 2019, http://chirp.sr.bham.ac.uk/alerts.
16. A. F. Brooks and V. Fafone, *Thermal Adaptive Optics* (World Scientific, 2019), Chapter 22, pp. 609–637.
17. R. X. Adhikari, "Gravitational radiation detection with laser interferometry," Rev. Mod. Phys. **86**, 121 (2014).
18. S. D. Penn, G. M. Harry, A. M. Gretarsson, S. E. Kittelberger, P. R. Saulson, J. J. Schiller, J. R. Smith, and S. O. Swords, "High quality factor measured in fused silica," Rev. Sci. Instrum. **72**, 3670–3673 (2001).
19. S. Rowan, J. Hough, and D. Crooks, "Thermal noise and material issues for gravitational wave detectors," Phys. Lett. A **347**, 25–32 (2005).
20. The Virgo Collaboration, "The monolithic suspension for the Virgo interferometer," Classical Quantum Gravity **27**, 084021 (2010).
21. A. Amato, S. Terreni, V. Dolique, D. Forest, G. Gemme, M. Granata, L. Mereni, C. Michel, L. Pinard, B. Sassolas, J. Teillon, G. Cagnoli, and M. Canepa, "Optical properties of high-quality oxide coating materials used in gravitational-wave advanced detectors," J. Phys. Mater. **2**, 035004 (2019).
22. L. Pinard, B. Sassolas, R. Flaminio, D. Forest, A. Lacoudre, C. Michel, J. Montorio, and N. Morgado, "Toward a new generation of low-loss mirrors for the advanced gravitational waves interferometers," Opt. Lett. **36**, 1407–1409 (2011).
23. H. B. Callen and T. A. Welton, "Irreversibility and generalized noise," Phys. Rev. **83**, 34–40 (1951).
24. G. M. Harry, A. M. Gretarsson, P. R. Saulson, S. E. Kittelberger, S. D. Penn, W. J. Startin, S. Rowan, M. M. Fejer, D. R. M. Crooks, G. Cagnoli, J. Hough, and N. Nakagawa, "Thermal noise in interferometric gravitational wave detectors due to dielectric optical coatings," Classical Quantum Gravity **19**, 897 (2002).
25. M. Granata, E. Saracco, N. Morgado, A. Cajgfinger, G. Cagnoli, J. Degallaix, V. Dolique, D. Forest, J. Franc, C. Michel, L. Pinard, and R. Flaminio, "Mechanical loss in state-of-the-art amorphous optical coatings," Phys. Rev. D **93**, 012007 (2016).
26. M. Granata, A. Amato, L. Balzarini, M. Canepa, J. Degallaix, D. Forest, V. Dolique, L. Mereni, C. Michel, L. Pinard, B. Sassolas, J. Teillon, and G. Cagnoli, "Amorphous optical coatings of present gravitational-wave interferometers," arXiv:1909.03737 (2019).
27. T. L. collaboration, "Git repository for gravitational wave interferometer noise calculator (gwinc)," 2019, https://git.ligo.org/gwinc/pygwinc.
28. A. Fox and T. Li, "Computation of optical resonator modes by the method of resonance excitation," IEEE J. Quantum Electron. **4**, 460–465 (1968).
29. J. Degallaix, "Oscar a MATLAB based optical FFT code," J. Phys. Conf. Ser. **228**, 012021 (2010).
30. N. Straniero, J. Degallaix, R. Flaminio, L. Pinard, and G. Cagnoli, "Realistic loss estimation due to the mirror surfaces in a 10 meters-long high finesse Fabry-Perot filter-cavity," Opt. Express **23**, 21455–21476 (2015).
31. C. Bond, D. Brown, A. Freise, and K. A. Strain, "Interferometer techniques for gravitational-wave detection," Living Rev. Relativity **19**, 3 (2016).
32. Heraeus, "Quartz glass for optics, data and properties," 2019, https://www.heraeus.com/media/media/hca/doc_hca/products_and_solutions_8/optics/Data_and_Properties_Optics_fused_silica_EN.pdf.
33. W. B. Jackson, N. M. Amer, A. Boccara, and D. Fournier, "Photothermal deflection spectroscopy and detection," Appl. Opt. **20**, 1333–1344 (1981).
34. D. Schönfeld, T. Reuter, R. Takke, and S. Thomas, "Stitching oil-on interferometry of large fused silica blanks," Proc. SPIE **5965**, 59650V (2005).
35. S. Wilson and J. McNeil, "Neutral ion beam figuring of large optical surfaces," Proc. SPIE **818**, 320–324 (1987).
36. S. Hild, A. Freise, M. Mantovani, S. Chelkowski, J. Degallaix, and R. Schilling, "Using the etalon effect for in situ balancing of the advanced Virgo arm cavities," Classical Quantum Gravity **26**, 025005 (2009).
37. M. Principe, "Minimum noise optical coatings for interferometric detectors of gravitational waves," in *IEEE Metrology for Aerospace (MetroAeroSpace)* (IEEE, 2014), pp. 473–478.
38. A. Staley, D. Martynov, R. Abbott, R. X. Adhikari, K. Arai, S. Ballmer, L. Barsotti, A. F. Brooks, R. T. DeRosa, S. Dwyer, A. Effler, M. Evans, P. Fritschel, V. V. Frolov, C. Gray, C. J. Guido, R. Gustafson, M. Heintze, D. Hoak, K. Izumi, K. Kawabe, E. J. King, J. S. Kissel, K. Kokeyama, M. Landry, D. E. McClelland, J. Miller, A. Mullavey, B. O'Reilly, J. G. Rollins, J. R. Sanders, R. M. S. Schofield, D. Sigg, B. J. J. Slagmolen, N. D. Smith-Lefebvre, G. Vajente, R. L. Ward, and C. Wipf, "Achieving resonance in the advanced Ligo gravitational-wave interferometer," Classical Quantum Gravity **31**, 245010 (2014).
39. A. Rocchi, E. Coccia, V. Fafone, V. Malvezzi, Y. Minenkov, and L. Sperandio, "Thermal effects and their compensation in advanced Virgo," J. Phys. Conf. Ser. **363**, 012016 (2012).
40. C. Michel, N. Morgado, L. Pinard, B. Sassolas, R. Bonnand, J. Degallaix, D. Forest, R. Flaminio, and G. Billingsley, "Realization of low-loss mirrors with sub-nanometer flatness for future gravitational wave detectors," Proc. SPIE **8550**, 85501P (2012).
41. B. Sassolas, N. Straniero, J. Degallaix, C. Michel, L. Pinard, J. Teillon, L. Balzarini, R. Flaminio, D. Hofman, B. Lagrange, and G. Cagnoli, "Mitigation of the spiral pattern induced by the planetary motion," in *Optical Interference Coatings* (Optical Society of America, 2016), paper MB–6.
42. S. Gras, H. Yu, W. Yam, D. Martynov, and M. Evans, "Audio-band coating thermal noise measurement for advanced Ligo with a multimode optical resonator," Phys. Rev. D **95**, 022001 (2017).
43. S. Gras and M. Evans, "Direct measurement of coating thermal noise in optical resonators," Phys. Rev. D **98**, 122001 (2018).
44. M. Rakhmanov, "Doppler-induced dynamics of fields in Fabry-Perot cavities with suspended mirrors," Appl. Opt. **40**, 1942–1949 (2001).
45. E. Hirose, D. Bajuk, G. Billingsley, T. Kajita, B. Kestner, N. Mio, M. Ohashi, B. Reichman, H. Yamamoto, and L. Zhang, "Sapphire mirror for the KAGRA gravitational wave detector," Phys. Rev. D **89**, 062003 (2014).
46. M. Granata, K. Craig, G. Cagnoli, C. Carcy, W. Cunningham, J. Degallaix, R. Flaminio, D. Forest, M. Hart, J.-S. Hennig, J. Hough, I. MacLaren, I. W. Martin, C. Michel, N. Morgado, S. Otmani, L. Pinard, and S. Rowan, "Cryogenic measurements of mechanical loss of high-reflectivity coating and estimation of thermal noise," Opt. Lett. **38**, 5268–5271 (2013).
47. D. Castelvecchi, "Gravitational-wave observatory LIGO set to double its detecting power," 2019, https://www.nature.com/articles/d41586-019-00573-4.
48. M. Granata, A. Amato, G. Cagnoli, M. Coulon, J. Degallaix, D. Forest, L. Mereni, C. Michel, L. Pinard, B. Sassolas, and J. Teillon, "Progress in the measurement and reduction of thermal noise in optical coatings for gravitational-wave detectors," in *Optical Interference Coatings* (Optical Society of America, 2019), paper FA.1.
49. W. Yam, S. Gras, and M. Evans, "Multimaterial coatings with reduced thermal noise," Phys. Rev. D **91**, 042002 (2015).
50. G. D. Cole, W. Zhang, M. J. Martin, J. Ye, and M. Aspelmeyer, "Tenfold reduction of Brownian noise in high-reflectivity optical coatings," Nat. Photonics **7**, 644 (2013).
51. G. D. Cole, W. Zhang, B. J. Bjork, D. Follman, P. Heu, C. Deutsch, L. Sonderhouse, J. Robinson, C. Franz, A. Alexandrovski, M. Notcutt, O. H. Heckl, J. Ye, and M. Aspelmeyer, "High-performance near-and mid-infrared crystalline coatings," Optica **3**, 647–656 (2016).

C94 Vol. 36, No. 11 / November 2019 / *Journal of the Optical Society of America A* Research Article

52. M. Punturo, M. Abernathy, F. Acernese, B. Allen, N. Andersson, K. Arun, F. Barone, B. Barr, M. Barsuglia, M. Beker, N. Beveridge, S. Birindelli, S. Bose, L. Bosi, S. Braccini, C. Bradaschia, T. Bulik, E. Calloni, G. Cella, E. C. Mottin, S. Chelkowski, A. Chincarini, J. Clark, E. Coccia, C. Colacino, J. Colas, A. Cumming, L. Cunningham, E. Cuoco, S. Danilishin, K. Danzmann, G. D. Luca, R. D. Salvo, T. Dent, R. D. Rosa, L. D. Fiore, A. D. Virgilio, M. Doets, V. Fafone, P. Falferi, R. Flaminio, J. Franc, F. Frasconi, A. Freise, P. Fulda, J. Gair, G. Gemme, A. Gennai, A. Giazotto, K. Glampedakis, M. Granata, H. Grote, G. Guidi, G. Hammond, M. Hannam, J. Harms, D. Heinert, M. Hendry, I. Heng, E. Hennes, S. Hild, J. Hough, S. Husa, S. Huttner, G. Jones, F. Khalili, K. Kokeyama, K. Kokkotas, B. Krishnan, M. Lorenzini, H. Lück, E. Majorana, I. Mandel, V. Mandic, I. Martin, C. Michel, Y. Minenkov, N. Morgado, S. Mosca, B. Mours, H. Müller, P. Ebhardt, R. Murray, J. Nawrodt, R. Nelson, C. Oshaughnessy, D. Ott, C. Palomba, A. Paoli, G. Parguez, A. Pasqualetti, R. Passaquieti, D. Passuello, L. Pinard, R. Poggiani, P. Popolizio, M. Prato, P. Puppo, D. Rabeling, P. Rapagnani, J. Read, T. Regimbau, H. Rehbein, S. Reid, L. Rezzolla, F. Ricci, F. Richard, A. Rocchi, S. Rowan, A. Rüdiger, B. Sassolas, B. Sathyaprakash, R. Schnabel, C. Schwarz, P. Seidel, A. Sintes, K. Somiya, F. Speirits, K. Strain, S. Strigin, P. Sutton, S. Tarabrin, A. Thüring, J. van den Brand, C. van Leewen, M. van Veggel, C. van den Broeck, A. Vecchio, A. Veitch, F. Vetrano, A. Vicere, S. Vyatchanin, B. Willke, G. Woan, P. Wolfango, and K. Yamamoto, "The Einstein telescope: a third-generation gravitational wave observatory," Classical Quantum Gravity **27**, 194002 (2010).

53. D. Reitze, LIGO Laboratory: California Institute of Technology, LIGO Laboratory: Massachusetts Institute of Technology, LIGO Hanford Observatory, and LIGO Livingston Observatory, "The US program in ground-based gravitational wave science: contribution from the LIGO laboratory," Bull. Am. Astron. Soc. **51**, 141 (2019).

SoftwareX 12 (2020) 100587

Contents lists available at ScienceDirect

SoftwareX

journal homepage: www.elsevier.com/locate/softx

Original software publication

OSCAR: A MATLAB based package to simulate realistic optical cavities

J. Degallaix

Laboratoire des Matériaux Avancés - IP2I, CNRS/IN2P3, Université Claude Bernard Lyon 1, Université de Lyon, 69100 Villeurbanne, France

ARTICLE INFO

Article history:
Received 14 March 2020
Received in revised form 30 June 2020
Accepted 9 September 2020

Keywords:
Fabry–Perot cavities
Mirrors
Interferometry

ABSTRACT

OSCAR is a MATLAB toolbox to simulate optical resonators such as Fabry–Perot cavities in presence of imperfect optics. It can handle any wavefront distortions as deviation of radius of curvature or 2D profile height of the surface of the mirrors. The package also natively supports arbitrary laser beam shapes from higher order optical modes (in Hermite or Laguerre Gauss basis) or from exotic flat beams. One of the most suitable application of OSCAR is designing and commissioning the long arm cavities of laser gravitational wave detectors.

Code Metadata

Current code version	3.2
Permanent link to code/repository used for this code version	https://github.com/ElsevierSoftwareX/SOFTX_2020_116
Code Ocean compute capsule	none
Legal Code License	BSD-3-Clause
Code versioning system used	git https://github.com/Jerome-LMA/oscar
Software code languages, tools, and services used	MATLAB
Compilation requirements, operating environments & dependencies	Same as MATLAB
If available Link to developer documentation/manual	documentation is inside the package
Support email for questions	j.degallaix@lma.in2p3.fr

1. Motivation and significance

Optical resonators are regularly used to amplify signals through the interaction with light. The most simple of such resonators is the Fabry–Perot cavity, two high reflectivity mirrors facing each other and separated by a distance. The length of the cavity could range from millimeter to probe optomechanical interaction [1], to meters (for magnetic birefringence measurement of vacuum [2]) and up to a kilometer scale for laser gravitation wave detectors [3].

To achieve the maximal signal amplification, optical losses must be restrained, setting hard specifications on the surface or coating of the mirrors. In particular, the quality of the polished substrate is crucial as surface defects scatter light and are usually the major source of optical losses [4]. Unfortunately, no simple analytical model exists linking the low spatial frequency surface defects (called flatness) and the losses in the cavity. Such a study could easily be performed in OSCAR as we will see later in this article in Section 3.

OSCAR stands for Optical Simulation Containing Ansys Results since this software was first designed to simulate optical cavities in presence of thermal distortions due to the heating from the laser beam. The non-spherical distortions (themoelastic deformations of the surfaces or thermal lensing effect in the substrates) was at that time derived from the FEM software ANSYS.

Later OSCAR was expanded to simulate any kind of planar optical cavities, linear or ring shapes with an arbitrary number of mirrors (2, 3 or 4 mirrors being the most common). In recent years, to fully simulate gravitational wave detectors, systems of coupled cavities were also implemented. The most complex configuration tested so far is Advanced Virgo, a dual recycled Michelson interferometer with Fabry–Perot arm cavities, however the code is not public as not yet fully documented. The code is always under-development to answer the needs of physicists and to take advantages of the latest computing development.

OSCAR was used extensively during the optical design and commissioning of the Advanced Virgo gravitational wave detector. In particular, it helped to define the geometry of the long arm cavities and setting the mirror polishing specifications. It also contributed to define the optical wavefront distortion budget

E-mail address: j.degallaix@lma.in2p3.fr.

https://doi.org/10.1016/j.softx.2020.100587

in order to not degrade the interferometer performances setting constraints on the quality of the correction of the Thermal Compensation System (TCS) [5]. More details on this topic could be find in the chapter 2 of the Advanced Virgo technical design report [6]. During the commissioning of Advanced Virgo, OSCAR is used to understand the behavior of the interferometer and in particular explaining the power and optical mode contents at the different port of the detector, for the carrier and sidebands fields.

2. Software description

The core of the program is a set of routines written in MATLAB to gain the full benefits from multicore CPU or user friendly interfaces [7]. The code takes advantage of the oriented object programming with classes (for example: electric field or cavity) and associated methods (for example: propagate the field or display the field intensity).

The goal of the simulations is to calculate the laser beams at the different positions inside and outside the optical cavity. For example for a given input laser beam, we are interested in the steady state power and shape of the laser beam circulating inside the cavity but also being reflected or transmitted. Those results depend also on the geometry of the cavity as well as the transmission/reflection of the different optics. In OSCAR, the laser beams are represented as 2D arrays of complex numbers corresponding to the 2D spatial distribution of the electric fields. For example, a complex fundamental Gaussian beam E could be discretized on a 2D Cartesian grid (x,y) as:

$$E(x,y) = Ae^{i\phi} e^{-\frac{(x^2+y^2)}{\omega^2}} e^{-i\frac{2\pi}{\lambda}\frac{(x^2+y^2)}{2R}} \quad (1)$$

with A the amplitude of the electric field, ϕ a possible phase shift (including the Gouy phase), ω the beam Gaussian beam radius, λ is the wavelength and R the complex radius of curvature of the wavefront. Of course, as the beam propagates or is reflected the parameters A, ϕ, ω and R will change accordingly.

2.1. Principle of the simulations

The code is built around a beam propagation method based on the FFT (Fast Fourier Transform) algorithm under the paraxial approximation [8]. Such approach is extremely powerful as the propagation over a distance of any arbitrary 2D electric fields is possible and with always the same computational effort. In more details the propagation is done in 3 steps:

1. the decomposition of the electric field on a sum of plane waves, done with a 2D FFT
2. propagation of each plane waves, done with a multiplication point by point of a complex 2D array
3. recomposition of the planes waves into the electric field with a 2D inverse FFT.

The second ingredient of the simulation is the handling of wavefront distortions encountered by the laser beam. Such distortions could come from the transmission through a lens, a reflection from a spherical mirror or an aberrated surface. A distortion is characterized by a 2D non uniform phase shift quantified by the optical path difference OPL. An electric field E_1 passing through the distortions OPL will thus get the additional phase shift and becomes E_2 according to:

$$E_2(x,y) = E_1(x,y)e^{-i\frac{2\pi}{\lambda}OPL(x,y)} \quad (2)$$

As an example, OPL from a mirror is simply twice the surface height (also called sagitta), for a spherical mirror of radius of curvature R_C, the OPL is given by:

$$OPL(x,y) = 2\left(R_C - \sqrt{R_C^2 - (x^2+y^2)}\right) \quad (3)$$

Once we are able to simulate the propagation of laser beams as well as reflections over surfaces, everything is in place to simulate optical cavities. In the Fabry–Perot cavity, the laser beam is propagating back and forth between the two mirrors and then all the propagating fields are summed at the same plane to calculate the total circulating beam. From there, the reflected and transmitted beams could be calculated.

2.2. Typical simulations

OSCAR is provided with a set of examples to demonstrate the simulation possibilities. As mentioned before, the code is particularly suited to simulate the steady state circulating, transmitted and reflected laser beams from optical cavities with any numbers of mirrors (example file: `Example_Pcirc.m`). It can include arbitrary input beams as well as imperfect optics (example file: `Example_HOM_with_maps.m`).

Once the cavity is defined, it is also possible to perform a scan over one free spectral range and display the result (example file: `Example_cavity_FSR_scan.m`). Theoretical 2D eigenmodes and eigenvalues of the cavity fields could also be calculated to check the round trip loss and resonance positions of the different higher order modes of the cavity (example file: `Example_cavity_eigenmodes.m`).

To simulate length control signals, radio-frequency sidebands can be added on the input field to derive error signals using the Pound Drever Hall technique [9] (example file: `Example_PDH_signal.m`).

OSCAR provides also a set of functions to read directly the 2D surface height files taken by wavefront measurement interferometers [10] from the brand Zygo [11] used in the mirror's characterization. It is possible to remove the tilt and curvature over a certain diameter and calculate the RMS of the surface (example file: `Example_Display_Create_maps.m`). That is particularly useful to validate the polishing work.

3. Illustrative example

One of the most emblematic example is the simulation of cavity round trip optical loss in presence of realistic polishing 2D surface maps. The round trip loss represents the fraction of light power falling outside the clear aperture of the mirror due to the imperfect flatness of the mirrors. That is a critical number for high finesse (i.e. very low loss) cavity and give some strong constraint on the surface quality of the mirrors.

To achieve this simulation, one must first define the mirrors: that includes, at minima, the diameter or clear aperture, the curvature and the reflectivity (or transmission) of the coating. Then a file, representing the 2D surface height of the mirror surface is loaded and added to the curved mirror surfaces. Such files could come from wavefront measurement of real mirrors [12] and are essential to confirm that mirrors meet their specifications.

Once the two (or more) mirrors are defined, the length of the cavity and the input beam are specified. That is all the information required to launch the simulation as output quantity could be selected later. A first function will calculate the round trip phase shift to guarantee that the circulating field is on resonance, maximizing the circulating power and a second function calculates the 2D steady state permanent fields in the cavity (circulating) as well as outside (reflected and transmitted fields). From there the conservation of energy (or power) can tell us how much light is lost due to the finite aperture of the mirrors.

An example of the result of such simulation is shown in the right part of Fig. 1. As the RMS of the flatness over the central part of the mirror is increased, the cavity round trip

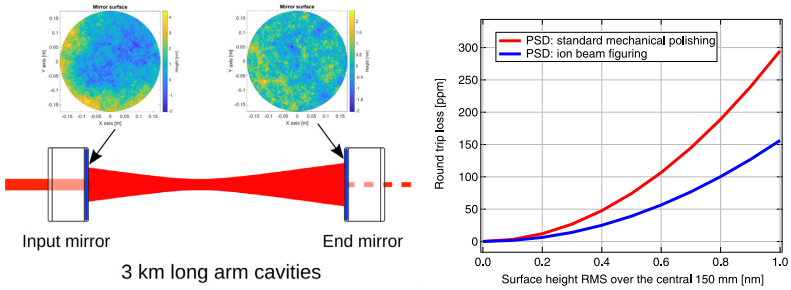

Fig. 1. Principle of the simulation (left): a Fabry–Perot cavity is simulated with realistic surface of the mirrors. The surface of the mirrors, excluding the curvature, is shown as 2D color plot of the surface height above the cavity sketch. Result of the simulation (right): Round Trip Loss (RTL) as a function of the surface flatness over the central part.

loss is also increased.[1] That is expected as the mirror surface defects are larger, more light is scattered and so lost. For this plot, two different kind of surfaces are tested, manufactured with two different techniques: standard mechanical polishing and ion beam figuring [13]. The two different techniques result in surface defects with different spatial frequencies (different PSD of the surface [14]), and hence different amount of light scattered even if the flatness in RMS is the same.

It can be remarked that, the round trip loss in the cavity is independent of the input beam shape for a high finesse cavity when there is no resonance degeneracy between the fundamental mode of interest and higher order optical modes. Also to be complete, the flatness is not the only source of light losses, as the surface (high spatial frequency) roughness or coating optical absorption must also be included in the light loss budget.

4. Impact

OSCAR was essential during the design and commissioning of the Advanced Virgo gravitational wave detector. Several points where this software made an impact could be highlighted:

- OSCAR was used to defined the flatness requirement for the most critical optics, in particular the mirrors of the long arm cavities. Similar to the example shown in Section 3, the cavity round trip loss was calculated for different levels of surface defects and it was demonstrated that to achieve a total round trip loss of less than 75 ppm, the RMS of the flatness must be less than 0.5 nm, on the central diameter of 150 mm.
- Still in the design phase of Advanced Virgo, OSCAR simulation of the full interferometer demonstrated the absolute necessity to be able to correct in situ the distortions in the power recycling cavity. It was shown that the errors of radii of curvature of the mirrors due to polishing tolerances have disastrous consequences on the light used to control the interferometer (the sideband fields). So stringent specifications were set for the thermal compensation system which must be able to correct such distortions.
- During the large optics production for Advanced Virgo, all the results from the optical characterization were progressively incorporated in the simulation. It was shown that an optic used in transmission (a compensation plate) was presenting a very large wavefront distortion impacting the performance of the detector. It was then decided to use a spare of better quality, which is now installed on the site.

[1] This is an academic example, as mechanical polishing cannot reach flatness below 2 nm RMS over a large diameter.

OSCAR is still currently used for the commissioning and monitoring of Advanced Virgo optical properties. As the input laser power is progressively increased, the uniform and non-uniform thermal effects are included and the simulations help to find the best operating point.

In the gravitational wave community but beyond Advanced Virgo, OSCAR was also essential to simulate:

- the losses inside long filtering cavities used to manipulate the quantum properties of light [4,15]
- the damping of parametric instabilities using tuning of the radius curvature of the mirrors [16,17]
- for the next generation of detectors, how the implementation of higher order modes could be impacted by mirror surface imperfections [18,19]

Outside the field of very large laser interferometers, OSCAR has also been proven to be useful to simulate mm-scale Fabry–Perot cavities and the degeneracy with higher optical modes [20,21].

5. Conclusions

OSCAR is a reliable and versatile MATLAB package to simulate realistic Fabry–Perot optical cavities. The main driver for its development was the design and commissioning of the laser gravitational wave detector Advanced Virgo and it has since been extensively used within this collaboration. OSCAR has also served other research area working with high finesse cavities. Since its first public release in 2008, the software has been downloaded more than 4000 times.

Declaration of competing interest

The authors declare that they have no known competing financial interests or personal relationships that could have appeared to influence the work reported in this paper.

Appendix A. Supplementary data

Supplementary material related to this article can be found online at https://doi.org/10.1016/j.softx.2020.100587.

References

[1] Favero I, Karrai K. Optomechanics of deformable optical cavities. Nat Photonics 2009;3(4):201. http://dx.doi.org/10.1038/nphoton.2009.42.
[2] Berceau P, Fouché M, Battesti R, Rizzo C. Magnetic linear birefringence measurements using pulsed fields. Phys Rev A 2012;85(1):013837. http://dx.doi.org/10.1103/physreva.85.013837.

[3] Acernese F, Agathos M, Agatsuma K, Aisa D, Allemandou N, Allocca A, et al. Advanced Virgo: a second-generation interferometric gravitational wave detector. Classical Quantum Gravity 2014;32(2):024001. http://dx.doi.org/10.1088/0264-9381/32/2/024001.
[4] Straniero N, Degallaix J, Flaminio R, Pinard L, Cagnoli G. Realistic loss estimation due to the mirror surfaces in a 10 meters-long high finesse Fabry-Perot filter-cavity. Opt Express 2015;23(16):21455–76. http://dx.doi.org/10.1364/OE.23.021455.
[5] Rocchi A, Coccia E, Fafone V, Malvezzi V, Minenkov Y, Sperandio L. Thermal effects and their compensation in Advanced Virgo. J Phys Conf Ser 2012;363:012016. http://dx.doi.org/10.1088/1742-6596/363/1/012016.
[6] Collaboration V, et al. Advanced virgo2012advanced Virgo technical design report. Virgo internal document VIR-0128A-12, 2012.
[7] Moler CB. Numerical computing with MATLAB: revised reprint. vol. 87. Siam; 2008.
[8] Beam propagation methods. In: Introduction to optical waveguide analysis. John Wiley & Sons, Ltd; 2002, p. 165–231. http://dx.doi.org/10.1002/0471221600.ch5.
[9] Black ED. An introduction to Pound–Drever–Hall laser frequency stabilization. Amer J Phys 2001;69(1):79–87. http://dx.doi.org/10.1119/1.1286663.
[10] Malacara D. Optical shop testing. vol. 59. John Wiley & Sons; 2007.
[11] Corporation Z. Laser interferometers. 2020, URL https://www.zygo.com/?/met/interferometers/.
[12] Degallaix J, Michel C, Sassolas B, Allocca A, Cagnoli G, Balzarini L, et al. Large and extremely low loss: the unique challenges of gravitational wave mirrors. J Opt Soc Amer A 2019;36(11):C85–94. http://dx.doi.org/10.1364/JOSAA.36.000C85.
[13] Wilson SR, McNeil JR. Neutral ion beam figuring of large optical surfaces. In: Fischer RE, Smith WJ, editors. Current developments in optical engineering II, vol. 0818. SPIE, International Society for Optics and Photonics; 1987, p. 320–4. http://dx.doi.org/10.1117/12.978903.
[14] Sidick E. Power spectral density specification and analysis of large optical surfaces. In: Bosse H, Bodermann B, Silver RM, editors. Modeling aspects in optical metrology II. vol. 7390. SPIE, International Society for Optics and Photonics; 2009, p. 195–206. http://dx.doi.org/10.1117/12.823844.
[15] Capocasa E, Barsuglia M, Degallaix J, Pinard L, Straniero N, Schnabel R, et al. Estimation of losses in a 300 m filter cavity and quantum noise reduction in the KAGRA gravitational-wave detector. Phys Rev D 2016;93:082004. http://dx.doi.org/10.1103/PhysRevD.93.082004.
[16] Zhao C, Ju L, Fang Q, Blair C, Qin J, Blair D, et al. Parametric instability in long optical cavities and suppression by dynamic transverse mode frequency modulation. Phys Rev D 2015;91:092001. http://dx.doi.org/10.1103/PhysRevD.91.092001.
[17] Ma YB, Liu J, Ma YQ, Zhao C, Ju L, Blair DG, et al. Thermal modulation for suppression of parametric instability in advanced gravitational wave detectors. Classical Quantum Gravity 2017;34(13):135001. http://dx.doi.org/10.1088/1361-6382/aa7340.
[18] Gatto A, Tacca M, Kéfélian F, Buy C, Barsuglia M. Fabry–Pérot-Michelson interferometer using higher-order Laguerre-Gauss modes. Phys Rev D 2014;90:122011. http://dx.doi.org/10.1103/PhysRevD.90.122011.
[19] Allocca A, Gatto A, Tacca M, Day RA, Barsuglia M, Pillant G, et al. Higher-order Laguerre-Gauss interferometry for gravitational-wave detectors with in situ mirror defects compensation. Phys Rev D 2015;92:102002. http://dx.doi.org/10.1103/PhysRevD.92.102002.
[20] Ott K, Garcia S, Kohlhaas R, Schüppert K, Rosenbusch P, Long R, et al. Millimeter-long fiber Fabry-Perot cavities. Opt Express 2016;24(9):9839–53. http://dx.doi.org/10.1364/OE.24.009839.
[21] Wittmuess P, Piehler S, Dietrich T, Ahmed MA, Graf T, Sawodny O. Numerical modeling of multimode laser resonators. J Opt Soc Amer B 2016;33(11):2278–87. http://dx.doi.org/10.1364/JOSAB.33.002278.

B

OUTREACH OFF THE BEATEN PATH

The outreach activities are inseparable to my research work and I enjoy them as organiser, participant or just spectator. I will not detail here all the events in the last 10 years from several open days (in the lab or not) to the countless presentations in Lyon for most, in France for some, and even a few abroad.

We will focus here on few unusual experiences, always enjoyable even if sometimes out of the comfort zone compared to the standard lab tours.

B.1 LASER IN THE SKY OF LYON

To celebrate the 20th anniversary of the planetarium of Vaulx en Velin, as well as for the international year of light in 2015, an experiment was proposed to the public to measure the speed of light, in the same spirit as Fizeau did in 1849 in Paris. A laser beam did a round trip between one of the highest points in Lyon (Colline de Fourvière) and the city hall of Vaulx en Velin (17 km round trip). With the help of a high speed rotating mirror, it was possible to measure the speed of light as a length of a bright laser segment projected on a screen.

This experience was lead by the institut Lumière Matière with all the support from the planetarium (especially to deal with the multiple authorisations). I participated in the meetings, installation and LMA contributed to some last minute optics (bought off the shelves). Only 3 evenings of commissioning were allowed and it started only to work right before the public opening. The laser was installed (in an ugly container box) right next to a landmark basilica and one of the best spots to encompass the whole city of Lyon, a truly magical place the evening (see the collage of photos in figure 44).

Needless to say, the event was a huge success and an exceptionally visible experiment in the sky of Lyon.

B.2 EVENTS WITH THE PLANETARIUM OF VAULX EN VELIN

I a still amazed about the energy and initiatives radiating from the planetarium of Vaulx en Velin [88]. They are truly doing a wonderful job promoting science and the Universe in general. As part of the regular event I am participating in, is 'Ouf d'astro' ('crazy about astro') which happens every 2 years. During this festival lasting several weeks, a lot of events are happening but there are always two days of meeting between scientists and people which takes place in a play-

Figure 44: From left to right, top to bottom: inside the laser container with the visit of the police the first night, first evening with the public, the outside setting during the pointing tests and view of the laser in the sky.

ful environment to encourage discussions. It is always a memorable day and every time the concept is different and very creative from chasing scientists as pokemon to revealing scientists as dissidents in a dystopian world of fake news (illustrations in 45).

The planetarium has also welcomed us with communicating enthusiasm for two special nights in 2017 and 2019: "La nuit des ondes gravitationnelles" et "la nuit de l'antimatière", two nights organised by the French Physical Society and taking place synchronously in multiple sites at the same time with local and remote events. The planetarium managed that very smoothly even with all our constraints and the technical problems during the nights.

Figure 45: My first participation in 2011 in Ouf d'Astro and in 2019 with a Michelson interferometer (mini-Virgo) with an audio output. Photo left by Ville de Vaulx-en-Velin, Studio Gaudin Ramet.

So if I have a message for them: "Simon, Pierre, thank you and keep doing this amazing work".

B.3 SCIENTIFIC CULTURE IN JAILS

Another unusual project close to my heart is the outreach activities in jails. It all started in 2018 thanks to a meeting with the association "Égalité des Sciences" [89] organised by our regional CNRS bureau. This association is devoted to organise meetings between prisoners and researchers. The activities proposed could range from standard presentations to even practical works (once validated by the authorities).

I must admit that we are not dealing with the usual recipients of our actions and so I was quickly appealed by this project. Moreover, I do not have often the opportunity to visit a jail. For my first visit, I prepared a presentation about the history of astronomy and how the technical progress helps to see further and further and changes the place of the Man in the Universe. It went very well and the audience was really engaging (all volunteers), more active than a class of high school students.

After discussing this experience with the Virgo Outreach coordinator, it was decided to attempt a common week of outreach in jail for 2020. As a start, using Virgo members network, activities will be proposed in France, Italy and Spain at the same time. I also spent time looking for people doing similar activity in France to see if we can do a coordinated action to have a larger visibility.

B.4 PRODUCTION WITH THE ARTIST ALEX ANDRIX

Alex Andrix [90] is a numerical artist with a unique interest in science. I met him while he was impregnated by thermal noise during his artistic residency at ENS Lyon. He came by curiosity to our first meeting on GW for interested scientists in Lyon and we quickly exchanged ideas. This first contact led to a residency at LMA for one week to discuss the science of GW[1]. As a result, GW made an appearance in Alex's immersive show called 'Variation Physic Vol II', which has to be appreciated with a VR headset.

Half a year after this first interaction, I proposed to Alex to create an artistic rendering to illustrate a coming LIGO-Virgo article about a special event. This event, called GW190814, was the fusion of a black hole with an enigmatic object, either the lightest black hole or the heaviest neutron star ever detected. From the recorded signal the two hypotheses could not be distinguished. Alex was in the secret of the

1 This visit was made possible thanks to a funding from the Labex LIO.

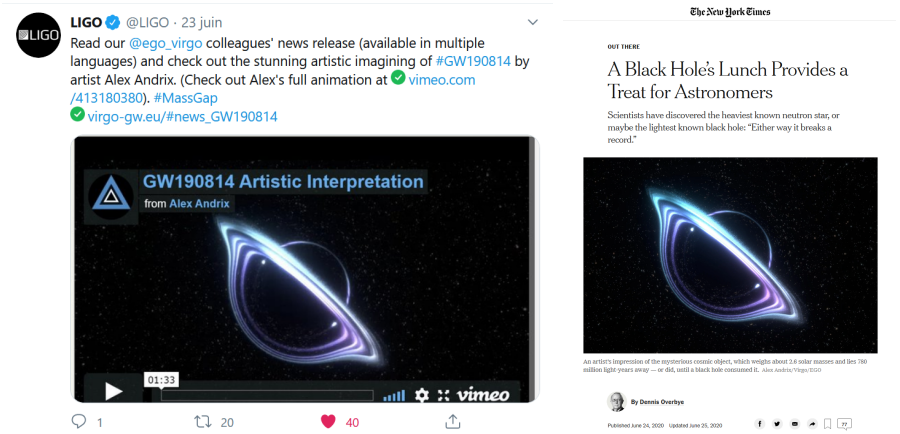

Figure 46: The artistic animation for GW190814 prepared by Alex got quite some resonances with here two examples a tweet from LIGO (left) and the article from the New York Times (right).

coming announcement and based on a draft of the scientific article he proposed his vision for this special coalescence.

The interaction with the Virgo outreach team was more intense than expected. With several meetings to be sure that the message from Alex's animation about the mysterious object could not be misinterpreted and then amplified by social networks. Then we shared this work with our LIGO colleagues and another round of meetings happened with further careful wordings around the rendering.

In the end it put some constraints on the artistic freedom but that was the price to pay to be endorsed by the scientific institutions. The animation [91] was released at the same time as the article and was a huge success with more than 70 000 views. I was really delighted to see some still images from the animation illustrating several articles from mainstream newspapers.

B.5 SEEN AT THE TV!

My young career did not go unnoticed by the local TV channels, you can find some screenshot of my interviews during the last 10 years in the figure 47.

Figure 47: Thank you France 3 Rhône Alpes and BFM TV Lyon for your support, it restores my faith in true journalism.

C

BONUS

You want to shine in society ? impress your friends and family with your superior intellectual skills ? It is now possible thanks to this cheat card to take everywhere with you and calculate quickly the finesse or the gain of any cavities. All the cool formulas from this document in one place, pocket size[1].

Cavity style	**AdV**	**BMV**
Hypothesis	$T_1 \gg T_2, L$	$T_1 = T_2 = T, L \approx T$
Finesse	$\frac{2\pi}{T_1}$	$\frac{2\pi}{2T+L}$
Power Gain	$\frac{4}{T_1}$	$\frac{4T}{(2T+L)^2}$
Reflected power	$1-\frac{4}{T_1}(T_2+L)$	$\left(\frac{L}{2T+L}\right)^2$

1 Also available in a laminated version for the adventurous off-road readers.

BIBLIOGRAPHY

[1] Albert Einstein. "Die feldgleichungen der gravitation". In: *Sitzung der physikalische-mathematischen Klasse* 25 (1915), pp. 844–847.

[2] Albert Einstein. "Näherungsweise Integration der Feldgleichungen der Gravitation". In: *Preussische Akademie der Wissenschaften, Sitzungsberichte* (1916), pp. 688–696.

[3] Kip S Thorne, Charles W Misner, and John Archibald Wheeler. *Gravitation*. Freeman, 2000.

[4] Joel M Weisberg, David J Nice, and Joseph H Taylor. "Timing measurements of the relativistic binary pulsar PSR B1913+ 16". In: *The Astrophysical Journal* 722.2 (2010), p. 1030.

[5] SE Gossan, Patrick Sutton, A Stuver, Michele Zanolin, Kiranjyot Gill, and Christian D Ott. "Observing gravitational waves from core-collapse supernovae in the advanced detector era". In: *Physical Review D* 93.4 (2016), p. 042002.

[6] Brynmor Haskell and Andrew Melatos. "Models of pulsar glitches". In: *International Journal of Modern Physics D* 24.03 (2015), p. 1530008.

[7] Thibault Damour and Alexander Vilenkin. "Gravitational wave bursts from cosmic strings". In: *Physical Review Letters* 85.18 (2000), p. 3761.

[8] Reinhard Prix. "Gravitational waves from spinning neutron stars". In: *Neutron Stars and Pulsars*. Springer, 2009, pp. 651–685.

[9] Sirichai Chongchitnan and George Efstathiou. "Prospects for direct detection of primordial gravitational waves". In: *Phys. Rev. D* 73 (8 2006), p. 083511.

[10] Benjamin P Abbott, Richard Abbott, TD Abbott, MR Abernathy, Fausto Acernese, Kendall Ackley, Carl Adams, Thomas Adams, Paolo Addesso, RX Adhikari, et al. "Observation of gravitational waves from a binary black hole merger". In: *Physical review letters* 116.6 (2016), p. 061102.

[11] Benjamin P Abbott, Rich Abbott, TD Abbott, Fausto Acernese, Kendall Ackley, Carl Adams, Thomas Adams, Paolo Addesso, RX Adhikari, VB Adya, et al. "GW170817: observation of gravitational waves from a binary neutron star inspiral". In: *Physical Review Letters* 119.16 (2017), p. 161101.

[12] Paolo Creminelli and Filippo Vernizzi. "Dark Energy after GW170817 and GRB170817A". In: *Phys. Rev. Lett.* 119 (25 2017), p. 251302. DOI: 10.1103/PhysRevLett.119.251302.

[13] MR Drout, AL Piro, BJ Shappee, CD Kilpatrick, JD Simon, C Contreras, DA Coulter, RJ Foley, MR Siebert, N Morrell, et al. "Light curves of the neutron star merger GW170817/SSS17a: Implications for r-process nucleosynthesis". In: *Science* 358.6370 (2017), pp. 1570–1574.

[14] LIGO Scientific Collaboration, Virgo Collaboration, 1M2H Collaboration, Dark Energy Camera GW-EM Collaboration, DES Collaboration, DLT40 Collaboration, Las Cumbres Observatory Collaboration, VINROUGE Collaboration, MASTER Collaboration, et al. "A gravitational-wave standard siren measurement of the Hubble constant". In: *Nature* 551.7678 (2017), pp. 85–88.

[15] R. Abbott et al. *GWTC-2: Compact Binary Coalescences Observed by LIGO and Virgo During the First Half of the Third Observing Run*. 2020. arXiv: 2010.14527 [gr-qc].

[16] Gravitational Wave Open Science Center. *GWTC-2 Data Release Documentation*. 2020. URL: https://www.gw-openscience.org/GWTC-2/ (visited on 01/04/2021).

[17] and J Aasi et al. "Advanced LIGO". In: *Classical and Quantum Gravity* 32.7 (2015), p. 074001. DOI: 10.1088/0264-9381/32/7/074001.

[18] F Acernese et al. "Advanced Virgo: a second-generation interferometric gravitational wave detector". In: *Classical and Quantum Gravity* 32.2 (2014), p. 024001. DOI: 10.1088/0264-9381/32/2/024001.

[19] T. Akutsu, M. Ando, K. Arai, Y. Arai, S. Araki, A. Araya, N. Aritomi, and H. Asada. "KAGRA: 2.5 generation interferometric gravitational wave detector". In: *Nature Astronomy* 3.1 (2019), pp. 35–40. ISSN: 2397-3366. DOI: 10.1038/s41550-018-0658-y. URL: https://doi.org/10.1038/s41550-018-0658-y.

[20] Benjamin P Abbott, R Abbott, TD Abbott, MR Abernathy, F Acernese, K Ackley, C Adams, T Adams, Paolo Addesso, RX Adhikari, et al. "Prospects for observing and localizing gravitational-wave transients with Advanced LIGO, Advanced Virgo and KAGRA". In: *Living Reviews in Relativity* 23.3 (2020).

[21] R. Abbott et al. "Observation of Gravitational Waves from Two Neutron Star–Black Hole Coalescences". In: *The Astrophysical Journal Letters* 915.1 (2021), p. L5. DOI: 10.3847/2041-8213/ac082e. URL: https://doi.org/10.3847/2041-8213/ac082e.

[22] Odylio Denys Aguiar. "Past, present and future of the Resonant-Mass gravitational wave detectors". In: 11.1 (2010), pp. 1–42.

[23] D Schnier, J Mizuno, Gerhard Heinzel, Harald Lück, A Rüdiger, Roland Schilling, M Schrempel, Walter Winkler, and Karsten Danzmann. "Power recycling in the Garching 30 m prototype interferometer for gravitational-wave detection". In: *Physics Letters A* 225.4-6 (1997), pp. 210–216.

[24] Massimo Granata, Alex Amato, Laurent Balzarini, Maurizio Canepa, Jérôme Degallaix, Danièle Forest, Vincent Dolique, Lorenzo Mereni, Christophe Michel, Laurent Pinard, et al. "Amorphous optical coatings of present gravitational-wave interferometers". In: *Classical and Quantum Gravity* 37.9 (2020), p. 095004.

[25] A Rocchi, E Coccia, V Fafone, V Malvezzi, Y Minenkov, and L Sperandio. "Thermal effects and their compensation in Advanced Virgo". In: *Journal of Physics: Conference Series*. Vol. 363. 1. IOP Publishing. 2012, p. 012016.

[26] F Acernese, M Agathos, L Aiello, A Allocca, A Amato, S Ansoldi, S Antier, M Arène, N Arnaud, S Ascenzi, et al. "Increasing the astrophysical reach of the advanced virgo detector via the application of squeezed vacuum states of light". In: *Physical review letters* 123.23 (2019), p. 231108.

[27] Yuhang Zhao, Naoki Aritomi, Eleonora Capocasa, Matteo Leonardi, Marc Eisenmann, Yuefan Guo, Eleonora Polini, Akihiro Tomura, Koji Arai, Yoichi Aso, et al. "Frequency-Dependent Squeezed Vacuum Source for Broadband Quantum Noise Reduction in Advanced Gravitational-Wave Detectors". In: *Physical Review Letters* 124.17 (2020), p. 171101.

[28] E Polini. "Broadband quantum noise reduction via frequency dependent squeezing for Advanced Virgo Plus". In: *Physica Scripta* 96.8 (2021), p. 084003.

[29] Grant David Meadors, Keita Kawabe, and Keith Riles. "Increasing LIGO sensitivity by feedforward subtraction of auxiliary length control noise". In: *Classical and Quantum Gravity* 31.10 (2014), p. 105014.

[30] S Soni, C Austin, A Effler, RMS Schofield, G González, VV Frolov, JC Driggers, A Pele, AL Urban, G Valdes, et al. "Reducing scattered light in LIGO's third observing run". In: *Classical and Quantum Gravity* 38.2 (2020), p. 025016.

[31] M Cabero et al. "Blip glitches in Advanced LIGO data". In: *Classical and Quantum Gravity* 36.15 (2019), p. 155010.

[32] Paul Berceau, Rémy Battesti, M Fouche, and Carlo Rizzo. "The vacuum magnetic birefringence experiment: a test for quantum electrodynamics". In: *Canadian Journal of Physics* 89.1 (2011), pp. 153–158.

[33] A Ejlli, F Della Valle, U Gastaldi, G Messineo, R Pengo, G Ruoso, and G Zavattini. "The PVLAS experiment: a 25 year effort to measure vacuum magnetic birefringence". In: *Physics Reports* (2020).

[34] MT Hartman, A Rivère, R Battesti, and C Rizzo. "Noise characterization for resonantly enhanced polarimetric vacuum magnetic-birefringence experiments". In: *Review of Scientific Instruments* 88.12 (2017), p. 123114.

[35] Garry Hamming. *Virgo Tecnical Documentation System*. 2010. URL: https://tds.virgo-gw.eu/ (visited on 08/30/2020).

[36] Garry Hamming. *Virgo Logbook*. 2010. URL: https://logbook.virgo-gw.eu/virgo/ (visited on 08/30/2020).

[37] T Accadia et al. "Status of the Virgo project". In: *Classical and Quantum Gravity* 28.11 (2011), p. 114002. DOI: 10.1088/0264-9381/28/11/114002.

[38] M Lorenzini and. "The monolithic suspension for the Virgo interferometer". In: *Classical and Quantum Gravity* 27.8 (2010), p. 084021. DOI: 10.1088/0264-9381/27/8/084021.

[39] T Accadia, F Acernese, M Agathos, A Allocca, P Astone, G Ballardin, F Barone, M Barsuglia, Andrea Basti, Th S Bauer, et al. "Central heating radius of curvature correction (CHRoCC) for use in large scale gravitational wave interferometers". In: *Classical and Quantum Gravity* 30.5 (2013), p. 055017.

[40] Richard Day and Antonino Chiummo. *Radius of Curvature Correction (CHRoCC) talk at LVC meeting, Gainesville*. 2011. URL: https://tds.virgo-gw.eu/ql/?c=8612 (visited on 08/30/2020).

[41] John M. Khosrofian and Bruce A. Garetz. "Measurement of a Gaussian laser beam diameter through the direct inversion of knife-edge data". In: *Appl. Opt.* 22.21 (1983), pp. 3406–3410. DOI: 10.1364/AO.22.003406.

[42] B. P. Abbott et al. "GW170814: A Three-Detector Observation of Gravitational Waves from a Binary Black Hole Coalescence". In: *Phys. Rev. Lett.* 119 (14 2017), p. 141101. DOI: 10.1103/PhysRevLett.119.141101.

[43] Orazio Svelto and David C Hanna. *Principles of lasers*. Springer, 2010.

[44] John A Sidles and Daniel Sigg. "Optical torques in suspended Fabry–Perot interferometers". In: *Physics Letters A* 354.3 (2006), pp. 167–172.

[45] R. Ward. *e-evaluating the choice of the Advanced Virgo arm cavity finesse*. 2010. URL: https://tds.virgo-gw.eu/ql/?c=7411 (visited on 08/30/2020).

[46] Daniel Malacara. *Optical shop testing*. Vol. 59. John Wiley & Sons, 2007.

[47] Nicolas Straniero. "Étude, développement et caractérisation des miroirs des interféromètres laser de 2ème génération dédiés à la détection des ondes gravitationnelles". PhD thesis. 2015. URL: http://www.theses.fr/2015LYO10319/document.

[48] Romain Bonnand. "The Advanced Virgo Gravitational wave detector : Study of the optical design and development of the mirrors". PhD thesis. 2012. URL: http://www.theses.fr/2012LYO10147.

[49] Marcel Demmler, Michael Zeuner, Frank Allenstein, Thoralf Dunger, Matthias Nestler, and Sven Kiontke. "Ion beam figuring (IBF) for high precision optics". In: *Advanced Fabrication Technologies for Micro/Nano Optics and Photonics III*. Vol. 7591. International Society for Optics and Photonics. 2010, 75910Y.

[50] Qi Fang, Carl D. Blair, Chunnong Zhao, and David G. Blair. "Revealing optical loss from modal frequency degeneracy in a long optical cavity". In: *Opt. Express* 29.15 (2021), pp. 23902–23915.

[51] John C Stover. "Optical scattering: measurement and analysis". In: Society of Photo-Optical Instrumentation Engineers. 2012.

[52] L. Pinard and J. Degallaix. *Polishing Specifications of the Advanced VIRGO End Mirror substrates*. 2012. URL: https://tds.virgo-gw.eu/ql/?c=8975 (visited on 08/30/2020).

[53] C. Michel, N. Morgado, L. Pinard, B. Sassolas, R. Bonnand, J. Degallaix, D. Forest, R. Flaminio, and G. Billingsley. "Realization of low-loss mirrors with sub-nanometer flatness for future gravitational wave detectors". In: *Optical Systems Design 2012*. Ed. by Laurent Mazuray et al. Vol. 8550. SPIE, 2012, pp. 516 – 522.

[54] Benoit Sassolas et al. "Mitigation of the spiral pattern induced by the planetary motion". In: *Optical Interference Coatings 2016*. Optical Society of America, 2016, MB.6.

[55] L. Pinard. *Advanced Virgo End Mirror Characterization report- EM01 (coatings C14042/10 + C14035/10)*. 2015. URL: https://tds.virgo-gw.eu/ql/?c=10990 (visited on 08/30/2020).

[56] A. Chiummo and A. Allocca. *Comment to Losses and free swinging measurements*. 2018. URL: https://logbook.virgo-gw.eu/virgo/?r=42757 (visited on 08/30/2020).

[57] MJ Lawrence, B Willke, ME Husman, EK Gustafson, and RL Byer. "Dynamic response of a Fabry–Perot interferometer". In: *JOSA B* 16.4 (1999), pp. 523–532.

[58] J. Casanueva, A. Allocca, M. Mantovani, and A. Chiummo. *North arm cavity ringing*. 2016. URL: https://logbook.virgo-gw.eu/virgo/?r=33795 (visited on 08/30/2020).

[59] A. Allocca and A. Chiummo. *Finesse measurement from ringing fit*. 2018. URL: https://logbook.virgo-gw.eu/virgo/?r=42806 (visited on 08/30/2020).

[60] Anthony E. Siegman. *Lasers*. University Science Books, 1986.

[61] Allocca. *Arms Gouy phase measurement*. 2019. URL: https://logbook.virgo-gw.eu/virgo/?r=47961 (visited on 08/30/2020).

[62] A. Allocca and M. De Laurentis. *Modes identification in the arms Free Spectral Range*. 2018. URL: https://logbook.virgo-gw.eu/virgo/?r=41721 (visited on 08/30/2020).

[63] A. Allocca and A. Chiummo. *Arm cavity gouy phase*. 2018. URL: https://logbook.virgo-gw.eu/virgo/?r=42701 (visited on 08/30/2020).

[64] A. Allocca and A. Chiummo. *Arms Gouy phase measurement - new RoCs for the ETM*. 2018. URL: https://logbook.virgo-gw.eu/virgo/?r=43276 (visited on 08/30/2020).

[65] A. Allocca, A. Chiummo, and P. Ruggi. *Where is the power lost ?* 2018. URL: https://logbook.virgo-gw.eu/virgo/?r=42058 (visited on 08/30/2020).

[66] A. Allocca, A. Chiummo, P. Ruggi, and H. Yamamoto. *Transient power drop in dark fringe lock acquisition during the commissioning before O3*. 2019. URL: https://tds.virgo-gw.eu/ql/?c=14881 (visited on 08/30/2020).

[67] Aidan F. Brooks et al. "Point absorbers in Advanced LIGO". In: *Appl. Opt.* 60.13 (2021), pp. 4047–4063. DOI: 10.1364/AO.419689.

[68] J. Degallaix. *Optical simulations arm cavities round trip loss vs input power*. 2019. URL: https://logbook.virgo-gw.eu/virgo/?r=47428 (visited on 08/30/2020).

[69] Jonathon Baird and Matteo Barsuglia. "Fine-Tuning the Optical Design of the Advanced Virgo+ Gravitational-Wave Detector Using Binary-Neutron Star Signals". In: *Galaxies* 8.4 (2020). ISSN: 2075-4434. URL: https://www.mdpi.com/2075-4434/8/4/86.

[70] Nur Ismail, Cristine Calil Kores, Dimitri Geskus, and Markus Pollnau. "Fabry-Pérot resonator: spectral line shapes, generic and related Airy distributions, linewidths, finesses, and performance at low or frequency-dependent reflectivity". In: *Optics express* 24.15 (2016), pp. 16366–16389.

[71] UPR3228. *Welcome page LNCMI*. 2019. URL: http://lncmi.cnrs.fr/en/welcome/ (visited on 08/30/2020).

[72] Mathilde Fouché. "Propagation de la lumière sous champ magnètique". PhD thesis. Université de Nice Sophia Antipolis, 2016. URL: https://tel.archives-ouvertes.fr/tel-01321760.

[73] Paul Berceau. "Propagation de photons sous champs magnétiques intenses - Etude expérimentale de la biréfringence magnétique du vide quantique". PhD thesis. Université Paul Sabatier - Toulouse III, 2012. URL: https://tel.archives-ouvertes.fr/tel-00766215.

[74] Eric D Black. "An introduction to Pound–Drever–Hall laser frequency stabilization". In: *American journal of physics* 69.1 (2001), pp. 79–87.

[75] QUBIG. *Home - QUBIG GmbH*. 2019. URL: https://www.qubig.com/ (visited on 08/30/2020).

[76] Karl Lambrecht Corporation. *Glan laser*. 2020. URL: http://www.klccgo.com/glanlaser.htm (visited on 08/30/2020).

[77] Red Pitaya. *Red Pitaya - Stemlab swiss army knife for engineers*. 2019. URL: https://www.redpitaya.com/ (visited on 08/30/2020).

[78] L. Neuhaus, R. Metzdorff, S. Chua, T. Jacqmin, T. Briant, A. Heidmann, P.-F. Cohadon, and S. Deléglise. "PyRPL (Python Red Pitaya Lockbox) — An open-source software package for FPGA-controlled quantum optics experiments". In: *2017 Conference on Lasers and Electro-Optics Europe European Quantum Electronics Conference (CLEO/Europe-EQEC)*. 2017, pp. 1–1.

[79] GGB. *Precision Laser Control Electronics*. 2019. URL: http://www.sisyph.com/ (visited on 08/30/2020).

[80] R Martonka and V Fliegel. "Hexapod: The Platform with 6DOF". In: *Modern Methods of Construction Design*. Springer, 2014, pp. 133–138.

[81] Symétrie. *Symetrie | Precision positioning and motion hexapods*. 2020. URL: https://symetrie.fr/en/hexapods/bora/ (visited on 08/30/2020).

[82] Physik Instrumente. *L-611 V6 Precision Rotation Stage Suitable for Vacuum*. 2020. URL: https://www.physikinstrumente.com/en/products/rotation-stages/l-611-v6-v7-v9-precision-rotation-stage-suitable-for-vacuum-412418484/ (visited on 08/30/2020).

[83] Y Salomon, N Sternberg, I Gouzman, G Lempert, E Grossman, D Katsir, R Cotostiano, and T Minton. "Qualification of Acktar Black coatings for space application". In: *Proceedings of the International Symposium on Materials in a Space Environment, Aix-En-Provence, France*. 2009.

[84] J Degallaix. *BMV style cavity - Length scan*. 2021. URL: https://youtu.be/bX7Q4s7Xiyk (visited on 09/01/2021).

[85] Garrett D Cole, Wei Zhang, Michael J Martin, Jun Ye, and Markus Aspelmeyer. "Tenfold reduction of Brownian noise in high-reflectivity optical coatings". In: *Nature Photonics* 7.8 (2013), pp. 644–650.

[86] Xu Chen, Clément Chardin, Kevin Makles, Charles Caër, Sheon Chua, Rémy Braive, Isabelle Robert-Philip, Tristan Briant, Pierre-François Cohadon, Antoine Heidmann, et al. "High-finesse Fabry–Perot cavities with bidimensional Si 3 N 4 photonic-crystal slabs". In: *Light: Science & Applications* 6.1 (2017), e16190–e16190.

[87] MS Seghilani, M Sellahi, M Devautour, P Lalanne, I Sagnes, G Beaudoin, M Myara, X Lafosse, L Legratiet, J Yang, et al. "Photonic crystal-based flat lens integrated on a Bragg mirror for high-Q external cavity low noise laser". In: *Optics express* 22.5 (2014), pp. 5962–5976.

[88] Ville de Vaulx-en velin. *Le Planétarium de Vaulx-en-Velin*. 1995. URL: https://www.planetariumvv.com/ (visited on 08/30/2020).

[89] Echo Sciences Grenoble. *Égalité des Sciences derrière les barreaux !* 2016. URL: https://www.echosciences-grenoble.fr/articles/egalite-des-sciences-derriere-les-barreaux (visited on 08/30/2020).

[90] Alex Andrix. *A Newotnian painter*. 2015-2020. URL: https://alexandrix.com/ (visited on 08/30/2020).

[91] Alex Andrix. *GW190814 Artistic Interpretation*. 2020. URL: https://vimeo.com/413180380 (visited on 08/30/2020).